Evaluating GPR polarization effects for imaging fracture channeling and estimating fracture properties

Christopher P. Perll
B.S General Geology, University of Kansas, 2011

Submitted to the graduate degree program in Geology and the Graduate Faculty of the University of Kansas in partial fulfillment of the requirements for the degree of Master of Arts

Advisory Committee

Dr. George Tsoflias - Chair

Dr. Ross Black

Dr. Jennifer Roberts

9/11/13
Date of Thesis Defense:

The Thesis Committee for Christopher P. Perll certifies that this is the approved version of the following thesis:

Evaluating GPR polarization effects for imaging fracture channeling and estimating fracture properties

Advisory Committee

Dr. George Tsoflias - Chair

Dr. Ross Black

Dr. Jennifer Roberts

9/11/13
Date Approved:

Abstract

This study investigates the polarization properties of GPR signals for imaging flow channeling in a discrete fracture. In particular this study examines if cross-polarized components could be used to image channels in a horizontal fracture. To understand how the polarization of radar waves affects imaging of channelized flow in a horizontal fracture, i) a series of numerical forward models was created with varying fracture aperture, channel orientation, and varying fracture water electrical conductivity, and ii) mulitpolarization field data were used to monitor dipole flow saline tracer tests in a subhorizontal fracture.

Numerical modeling demonstrated that the cross-polarized data held useful information about channels but only when the channel is oriented oblique to the E-W wavefield orientation. When the channel is oriented oblique to survey line, summation of the cross-polarized and co-polarized components results in an accurate representation of the total scattered energy from the channel. When the channel is oriented parallel or orthogonal to survey line summation the co-polarized components represent the total scattered energy.

In addition to numerical modeling multipolarization, time lapse GPR field data was acquired at the Altona Flat Rock test site in New York State. These surveys were conducted under varying artificial hydraulic gradients, to investigate channeled transport of different concentrations of saline tracer through the fracture and to highlight flow channels between wells. Amplitude analysis of the cross-polarized components reveals flow channeling in an E-W orientation which suggests good well connectivity in that direction. N-S amplitude trends suggest poor hydraulic connectivity. In conclusion, this investigation reveals that cross-polarized components of GPR signals contain useful information for imaging channeled flow in fractured media.

Acknowledgements

First, I would like to thank my advisor George Tsoflias, without his guidance and support this projected would not have been completed. I would also like to thank Ross Black and Jennifer Roberts for being on my committee and helping me with revisions. In addition to the great faculty here at KU I would like to thank all the geophysics students Bevin Bailey, Blair Benson, Anthony Hoch, Jose Velez, Clyde Redger, and Ayrat Sirazhiev. They made my time here at KU enjoyable and without their help and support I would not have been able to finish my degree. Special thanks to Matt Baker "sensei" who was always there to help with MATLAB. Furthermore, I need to thank the many friends I made at KU Gabe Creason, Rachelle Warren, Jessica Jordan, Ted Morehouse, Brian Klipp, Mallory Stevenson, Hannah Wasserman, Jeff Olmann, and Britney Katz. They gave me the confidence to finish this study and were always there when I needed them. Finally, I would like to thank any friends I forgot along with my parents and family for their support.

Table of Contents

List of Figures

List of Tables

Chapter 1: Introduction

1.1 Fractures and fluid flow

Fractures provide conduits for fluid flow, aquifer recharge, and movement of contaminants in fractured rock. Fracture network models are often used to analyze fluid flow in fractured rock. However, these models do not take into account the high heterogeneity of fractures. Variability of fracture aperture creates "flow channeling" or paths of least resistance. Flow channeling refers to a few preferential pathways where the majority of fluid flow occurs (Tsang and Neretnieks, 1998). Flow channeling occurs where fracture aperture increases, thus allowing for more fluid flow. Contaminants in ground-water, travel along channeled pathways, making it difficult to locate affected areas without detailed knowledge of channel locations and geometries (Talley et al., 2005). Therefore there is a need for imaging channelized flow and determining fracture properties to enable better prediction of fluid flow and transport in fractured bedrock. Ground penetrating radar (GPR) has been successfully used to image fractures and monitor contaminants (Birken and Versteeg, 2000; Kim et al., 2000; Sato and Miwa, 2000; Tsoflias et al., 2001; Day-Lewis et al., 2003), yet additional work is needed to understand the signal response to fracture channeling.

For my thesis, I examine the polarization effects of GPR for imaging fracture channels. I used Finite-Difference-Time-Domain (FDTD) numerical modeling to simulate GPR imaging of channels in a horizontal fracture. I also collected multipolarization GPR data to image channelized flow along a subhorizontal fracture at the Altona Flat Rock site near Plattsburg, NY. The four polarizations recorded were two orthogonal co-polarized and two cross-polarized signals. My study focuses on extracting information from the cross-polarized components. Several surveys were conducted with different frequencies under varying artificial hydraulic

gradients, which were introduced to facilitate transport of different concentrations of saline tracer throughout the fracture. Introducing varying amounts of saline tracer causes the electrical conductivity of the fracture water to increase, changing the amplitude and the phase of the reflected radar signals. I analyzed changes in the signal to identify channels within the fracture.

The thesis consists of 5 chapters. Chapter 1 discusses the various aspects of my work including fluid flow, GPR imaging of fractures, and GPR polarization effects. Chapter 2 provides background information on FDTD modeling, multipolarization GPR, and GPR polarization effects. Chapter 3 includes FDTD numerical modeling methods, results, and discussion. Chapter 4 includes a review of my field work methods, results, and discussion. Chapter 5 highlights the significance of the study and provides suggestions for future work.

1.2 GPR Imaging of Fractures

Numerical modeling is an effective way to test target responses from GPR. A common numerical method used is FDTD because of its simplicity and fast run times. Teixeira et al. (1998) developed a 3D FDTD method and modeled several common geologic targets to demonstrate the GPR response from models were similar to those seen in field data. Tang et al. (2006) generated a layered model of the subsurface and propagated GPR signals through the layers. They then used the simulated travel time of GPR waves through the different media to estimate layer thicknesses. Irving and Knight (2006) developed a FDTD method to simulate transmission and reception for crosshole GPR in heterogeneous media. GPR FDTD numerical modeling is a reliable method to simulate radar wave propagation.

GPR provides high resolution imaging of the subsurface and is capable of imaging fractures (Davis and Annan, 1989). Grasmueck et al. (1996; 2004; and 2005) used 3-D surveys to image fractures and emphasized quarter-wavelength spatial sampling as the minimum

requirement for high resolution 3-D surveys. Jeannin et al. (2006) used horizontal and vertical profiles along a cliff to image fractures at centimeter scale resolution and determined their orientation and dip. Theune et al. (2006) created maps of fractures and produced reliable data about their shape and density. In addition to imaging fractures GPR has been used to monitor fluid flow and determine flow paths. Tsoflias et al. (2001) used pumping tests in conjunction with ground based GPR to analyze changes in waveform to determine water saturation of fractures. Day-Lewis et al. (2003) used saline tracer and cross-hole GPR to identify preferential fracture flow paths. Combining saline tracer tests and single-hole GPR the connectivity and geometry of fractures that contributed to tracer transport were identified (Dorn et al., 2011; Dorn et al., 2012). GPR has the capability to image fractures and monitor the flow of tracers, but the quantitative prediction of fracture aperture and tracer concentration remains a challenge. Additional work is needed to understand the response of GPR to fracture properties.

Polarization of GPR signal refers to the orientation of the propagated EM wave which is controlled by the orientation of the antennas on the surface. Dipole antennas used in typical GPR systems create linearly polarized EM waves with strong amplitude directionality along the long axis of the antenna. Depending on the polarization of the incident wave and the orientation of the target the radar wave can be preferentially scattered (Roberts and Daniels, 1996). Preferential scattering causes changes in the amplitude and phase of the returned signal. The polarization effects of EM waves create different images of the subsurface. A typical GPR survey uses two dipole antennas positioned parallel to each other and oriented perpendicular to the survey line (Lehmann et al., 2000). Surveys using two dipole antennas collect single polarization data based on the orientation of the target. Changing the azimuth of the antennas on the surface causes the radiated EM waves to propagate in a different orientation thus illuminating the target differently.

Acquiring multipolarization GPR data provides more precise measurements of the size, shape, and orientation of the target (Van der Kruck et al., 2003; Radzevicius and Daniels, 2000; Roberts and Daniels, 1996).

Using multiple polarizations the target is illuminated with varying polarized waves which will be preferentially scattered based on the incident wave polarization and orientation of the target. Examining the returned wave from different polarizations and noting the changes in amplitude and phase, properties of the target can be discovered. Tsoflias et al. (2004) identified a phase difference in orthogonal pairs of polarization data sets to determine the azimuth of vertical fractures. Tsoflias and Hoch (2006) used controlled experiments to characterize thin layers using different GPR polarizations and noticed that changes in the signal amplitude and phase were related to layer properties, i.e thickness, fluid fill, and fluid electrical conductivity. Tsoflias et al. (2012) following a method proposed by Lehmann et al. (2000) combined orthogonal co-polarized datasets and obtained images of flow channeling within a subhorizontal fracture. By combing the co-polarized datasets reduced polarization effects caused by the dipole nature of the antennas and improved imaging of flow channeling.

1.3 Research Objectives and Significance

The objective of this study is to investigate the use of cross-polarized GPR data for imaging fracture flow channeling. Improved understanding of the polarization properties of radar signals will enhance the imaging capabilities of GPR for characterization of the heterogeneous fracture flow properties.

In this study I used Finite-Difference-Time-Domain (FDTD) numerical modeling to investigate the polarization effects of GPR. With the insight gained from FDTD modeling I demonstrate a method that uses the cross-polarized components from a multipolarization survey

at the Altona Flat Rock site to image fracture channeling. I then sum the multiple cross-polarized data to generate high resolution images of the fracture channel. To the best of my knowledge, this is the first study to use cross-polarized GPR data to image fracture channels.

Chapter 2: Background

2.1 GPR Analytical and Numerical Modeling

Forward modeling is used to improve the understanding of how GPR signals respond to a target of interest. The target of interest for my research is a water saturated subhorizontal fracture at 7.6 m depth at the Altona Flat Rock site. A prior study by Tsoflias and Becker (2008) created a series of analytical models using the recursive method to test the effects of signal frequency, fracture aperture, and water electrical conductivity on the reflection coefficient magnitude (R) and phase (Φ) of a horizontal thin fracture. The model parameters where set to resemble those at the Altona Flat Rock site. Their modeling method used the electrical properties of the layered model, electrical conductivity (σ), electrical permittivity (ε), magnetic permeability (μ), and layer thickness (d), to calculate the R and Φ (Figures 2.1-2.2).The models demonstrated that all frequencies show increased R with increase in d but low frequencies exhibit greater change in R with increasing σ. The phase response showed all frequencies demonstrated a phase delay due to increasing σ but the delay was greater in the low frequencies.

Using the knowledge gained from the analytical models Tsoflias and Becker (2008) used numerical modeling to simulate thin fracture responses for 50 and 100 MHz GPR signals. Numerical modeling incorporates geometric spreading, propagation effects, and signal attenuation that is not taken into account with analytical modeling. These models showed that the lower frequency 50 MHz GPR response had a pronounced phase lag and demonstrated greater change in amplitude in response to changes in fracture water electrical conductivity than the 100 MHz GPR data. The study concluded that lower frequencies are better for distinguishing changes in fracture electrical conductivity than higher frequencies.

Lane et al. (2000) used numerical modeling to distinguish between air, water, and hydrocarbon-filled fractures. The numerical models demonstrated the change in amplitude and phase that is associated with fracture fill. The water filled fractures generated the largest amplitudes and demonstrated reverse polarity compared to air and hydrocarbon filled fractures. Sambuelli and Calzoni (2010) used control experiments to vary fracture fill and determined that the phase and the amplitude of the reflected signals could be used to discriminate between dry and saturated fillings. Sato and Miwa (2000) used numerical modeling to analyze co-polarized and cross-polarized responses from a flat fracture and a nearly flat fracture with roughness. They showed no response from the cross-polarized components in the flat model but in the rough fracture model the cross-polarized components are depolarized and are able to detect the fracture.

The numerical modeling method used in my thesis study was Finite-Difference-Time-Domain (FDTD). FDTD modeling was chosen because the software is freeware and easy to manipulate. I used GprMax V 2.0 (Giannopoulos, 2005) to generate 3D models of horizontal fractures. The software solves the Maxwell equations (Equations 1-4) to propagate GPR waves throughout the models (Balanis, 1989). Variables in bold represent vector quantities and other symbols are scalar quantities. The Maxwell equations express the relations between the fundamental electromagnetic field quantities and their dependence on their sources:

$$\nabla \times \boldsymbol{E} = -\frac{\partial \boldsymbol{B}}{\partial t} \quad (1)$$

$$\nabla \times \boldsymbol{H} = \frac{\partial \boldsymbol{D}}{\partial t} + \boldsymbol{J} \quad (2)$$

$$\nabla \cdot \boldsymbol{B} = 0 \quad (3)$$

$$\nabla \cdot \boldsymbol{D} = q_V \quad (4)$$

where t is time in seconds, q_V is the volume electric charge density (C/m), **J** is current density (A/m^2), **E** is electric field intensity (V/m), **H** is magnetic field strength (A/m), **B** is magnetic flux

density (T), and **D** is electric flux density (C/m^2). Using Maxwell equations the general wave equations can be derived (Equations 5-6). The general wave equation or Maxwell equations can solve any electromagnetic field problem with known initial and boundary conditions.

$$\nabla^2 E = \mu_0 \varepsilon \frac{\partial^2 E}{\partial t^2} + \mu_0 \sigma \frac{\partial E}{\partial t} + \mu_0 \frac{\partial J_S}{\partial t} + \frac{1}{\varepsilon} \nabla q_V \quad (5)$$

$$\nabla^2 H = \mu_0 \varepsilon \frac{\partial^2 H}{\partial t^2} + \mu_0 \sigma \frac{\partial H}{\partial t} - \nabla \times J_S \quad (6)$$

To propagate a GPR signal GprMax discretizes both the space and time continua. The building block of this technique is the Yee cell (Yee, 1966) (Figure 2.3). In each Yee cell, a numerical solution of the wave equations is obtained in the time domain. After each iteration (time step), the electromagnetic (EM) field propagates in the model to the adjacent Yee cells. The nature of GPR forward problem classifies it as an initial value-open boundary problem. To obtain a solution one has to define an initial condition (i.e. GPR transmission pulse) and allow the resulting fields to propagate through an infinite model space. A detailed explanation of the various features of GprMax is available in the user manual (Giannopouls, 2005).

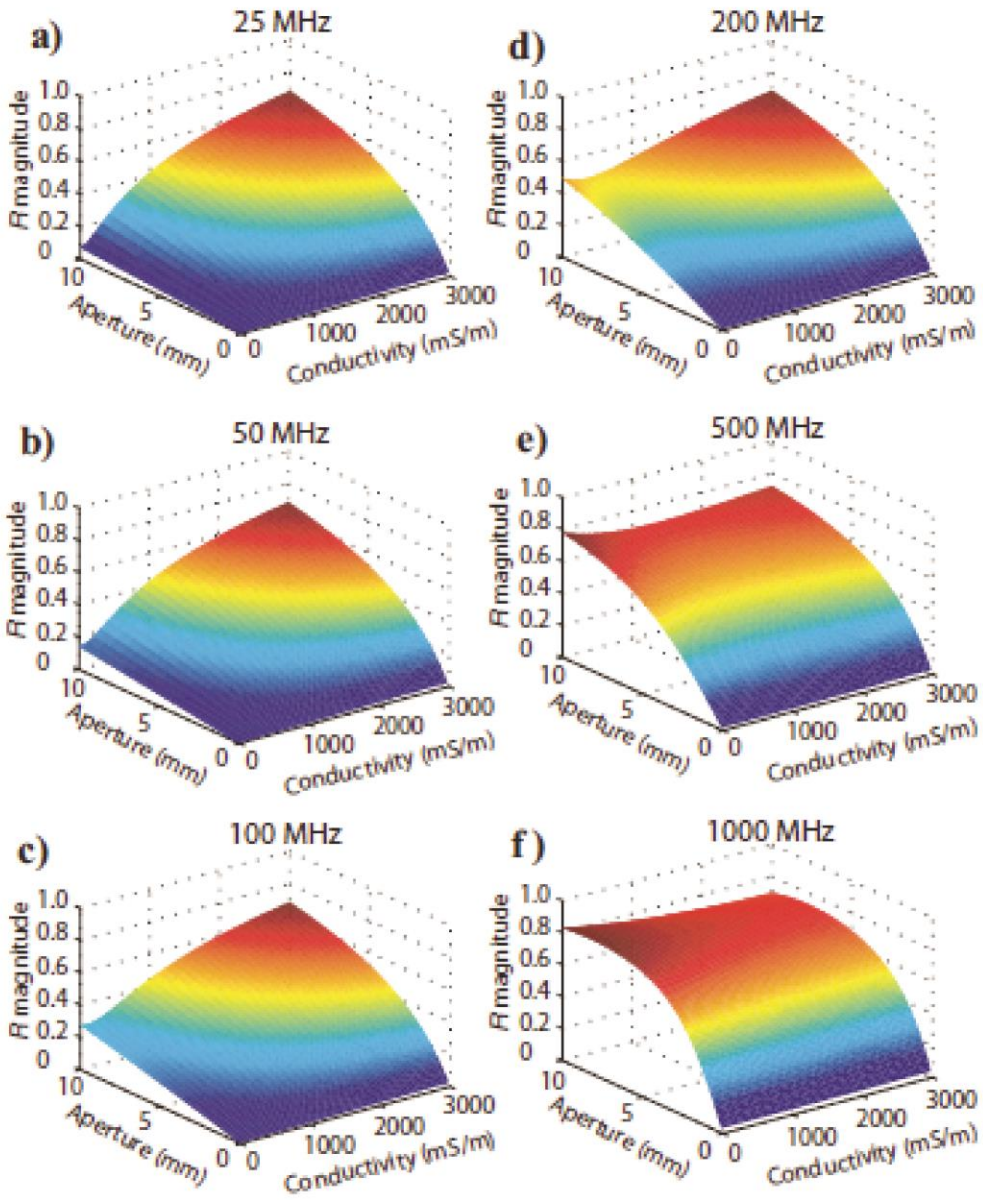

Figure 2.1: Plots of reflection coefficient magnitude R as a function of fracture aperture and water electrical conductivity. (a) 25 MHz, (b) 50 MHz, (c) 100 MHz, (d) 200 MHz, (e) 500 MHz, and (f) 1000 MHz (From Tsoflias and Becker, 2008).

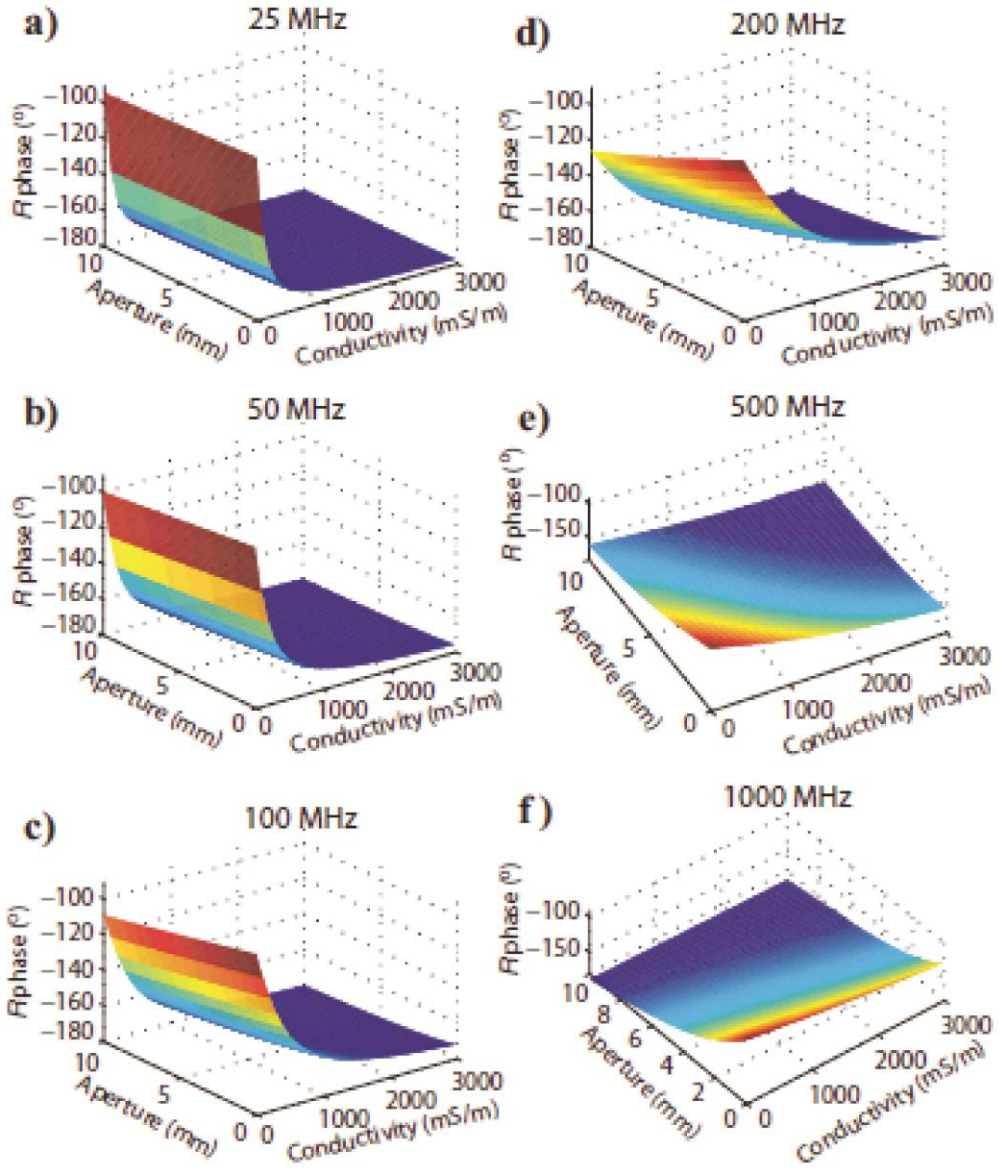

Figure 2.2: Plots of phase Φ as a function of fracture aperture and water electrical conductivity. (a) 25 MHz, (b) 50 MHz, (c) 100 MHz, (d) 200 MHz, (e) 500 MHz, and (f) 1000 MHz (From Tsoflias and Becker, 2008).

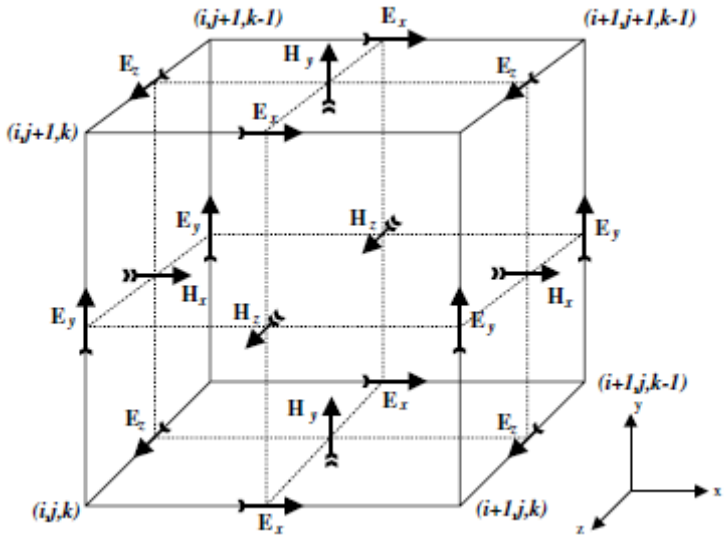

Figure 2.3: Yee cell building block of FDTD numerical modeling (From Giannopoulos, 2005).

2.2 GPR Imaging of Fractures

GPR transmits electromagnetic waves (EM) into the ground, where changes in electrical properties of the subsurface create reflections that are detected at the surface (Davis and Annan, 1989). Common GPR frequencies range from 10-1000 MHz. The electrical properties of the subsurface that affect GPR signals are electrical conductivity, electrical permittivity (dielectric constant), and magnetic permeability. Davis and Annan (1989) provide a table of common geological materials with typical electrical properties for at 100 MHz (Table 2.1). Large changes in electrical properties between subsurface layers will generate a strong response from GPR. For example a water filled fracture encased in bedrock would generate a strong reflection because of the large contrast in electrical properties between water and rock matrix. Because of this strong contrast in electrical properties GPR is a suitable geophysical method for imaging fractures. Field studies have shown the effectiveness of GPR for imaging and characterizing fractures (Davis and Annan, 1989; Tsoflias et al., 2001, Tsoflias, 2008).

The standard technique to study fractured systems is to use hydrogeological tests but these tests are limited to borehole locations and give little information on how the fracture connects the hydrologic system between the boreholes. Combining hydrogeological tests with a GPR survey has proven to be an effective method to identify and characterize fractures. (Day-Lewis et al., 2003; Talley et al., 2005; Tsoflias et al., 2001).

Tsoflias et al. (2001) acquired 200 MHz GPR refection data during several pumping tests in a fractured carbonate aquifer to determine if changes in fracture saturation could be assessed. The results demonstrate that the radar signal amplitude and waveform varied along a water filled fracture corresponding to changes in water saturation. Figure 2.4 demonstrates the change in waveform and amplitude of a fracture reflection, visible at 24-28 ns, during a pumping

test. Fracture reflections to the south of the pumping well show strong amplitudes, decreasing to smaller amplitudes north of the well. GPR was able to provide real time monitoring of pumping tests and quantify changes in signal amplitude and waveform to changes in water saturation.

Day-Lewis et al. (2003) collected cross-borehole GPR in conjunction with a saline tracer test to identify the presence and location of preferential flow paths in a fractured system. Saline water was injected into a fresh water fracture from one borehole and time-lapse cross-borehole GPR surveys were collected in three adjacent boreholes to track the plume of saline water. A 3-D inversion method was successful in locating the saline plume. Talley et al. (2005) used ground based GPR to detect saline tracer movement through a subhorizontal fracture at the Altona Flat Rock site. Several saline tests were conducted between different boreholes to determine how flow paths change under varying hydraulic conditions. Amplitude maps were created for each test to determine the flow paths of the saline tracers. Meter-scaled spatial variably was observed and attributed to heterogeneity in fracture aperture (i.e flow channeling).

Material	K	σ (mS/m)	V (m/ns)	α (dB/m)
Air	1	0	0.30	0
Distilled water	80	0.01	0.033	2×10^{-3}
Fresh water	80	0.5	0.033	0.1
Sea water	80	3×10^{4}	0.01	10^{3}
Dry sand	3-5	0.01	0.15	0.01
Saturated sand	20-30	0.1-1.0	0.06	0.03-0.3
Limestone	4-8	0.5-2	0.12	0.4-1
Shales	5-15	1-100	0.09	1-100
Silts	5-30	1-100	0.07	1-100
Clays	5-40	2-1000	0.06	1-300
Granite	4-6	0.01-1	0.13	0.01-1
Dry salt	5-6	0.01-1	0.13	0.01-1
Ice	3-4	0.01	0.16	0.01

Table 2.1: Electrical properties of common geological materials dielectric constant (K), electrical conductivity (σ), velocity (V), and attenuation (α).

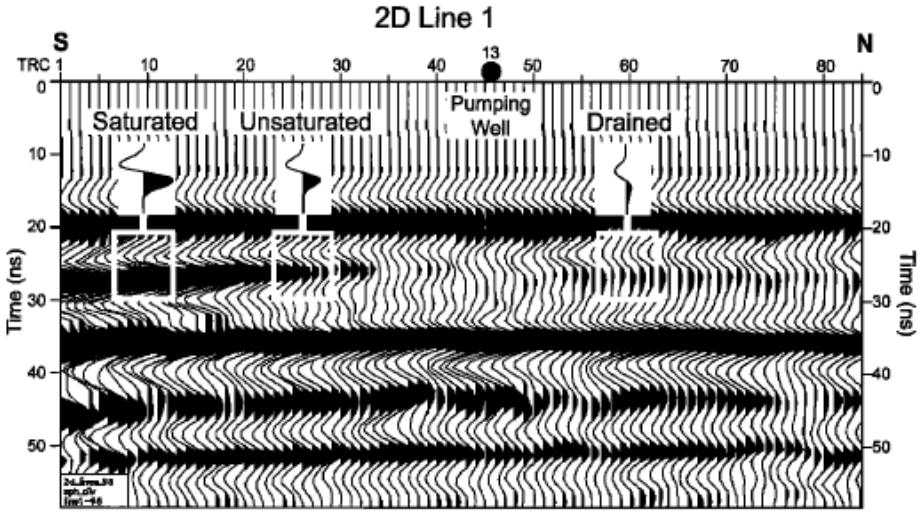

Figure 2.4: 2D line during pumping test demonstrating change in amplitude and phase corresponding to changes in fracture saturation (From Tsoflias et al., 2001).

2.3 Polarization Effects of GPR

The polarized nature of EM waves must be accounted for when collecting GPR data. The standard dipole antennas used in a GPR survey generate linearly polarized EM waves with the electric field component oriented along the long axis of the antenna. Changing the orientation of the antennas on the surface causes the GPR signal to change the polarization of the incident waveform that is being sent into the subsurface (Roberts and Daniels, 1996). By changing the polarization of the incident waveform the reflected signal from the target changes. Therefore, the orientation of the antennas along with the orientation the target must be accounted for to generate an accurate image of the subsurface (Luzitano and Ulrych 1996; Roberts and Daniels 1996; Radzevicius and Daniels 2000; Daniels et al., 2003; Lutz et al., 2003).

GPR polarization has been used to detect and characterize fractures. Seol et al. (2001) noticed that the reflection energy varied between GPR polarizations depending on the strike and dip of the reflector. Using the different polarizations Seol et al. (2001) developed a strike finding algorithm for dipping fractures. Thin vertically oriented fractures where detected with various polarizations and a phase lead was observed when the incident E-field component was oriented perpendicular to the plane of the fracture (Tsoflias et al., 2004). Based on the presence of the phase lead between different polarizations, the azimuth of the fracture could be determined. Further controlled experiments on thin fractures by Tsoflias and Hoch (2006) demonstrated changes in the amplitude and phase of the GPR signal based on system polarization relative to fracture fill. The change in amplitude and phase for the different polarizations were consistent with analytical model results and they concluded that these changes can be used to identify fracture fill properties.

Using multipolarization GPR data polarization has proven to be useful in characterizing fractures, but combining the information from multiple polarizations could improve the image of the subsurface. Lehmann et al., (2000) proposed a way to combine orthogonal co-polarized signals to produce a pseudoscalar data set with low levels of directionality. Summing the two orthogonal linear polarizations simulates a circular wavefront, similar to a seismic wave, allowing for standard seismic processing steps to be applied with more confidence. This allows for migration to be applied, therefore creating more accurate images of the subsurface. They demonstrated the effectiveness of summing orthogonal polarization in a 3D GPR survey over a gravel quarry. Summing two orthogonal co-polarized dataset they produced a pseudoscalar dataset (Figure 2.5). Images produced from the individual co-polarized signals are influenced by the directional properties of antennas and structures in the subsurface where the pseudoscalar sum provided an image that is not influenced by polarization. The method of summing two orthogonal polarizations in combination with saline tracer tests was used by Tsoflias et al. (2012) to image fracture flow paths in a subhorizontal fracture at the Altona Flat Rock site. Four polarizations were collected including two orthogonal co-polarized and two orthogonal cross-polarized signals. Amplitude maps were generated for the individual co-polarized data and also by summing the two orthogonal co-polarized signals. The individual co-polarized amplitude maps demonstrate high levels of directionality. The summed amplitude maps reduced the level of directionality and produced accurate images of fracture flow paths. Additional data within the cross-polarized components has not been investigated leading to the question of whether useful information can be extracted from the cross-polarized signals.

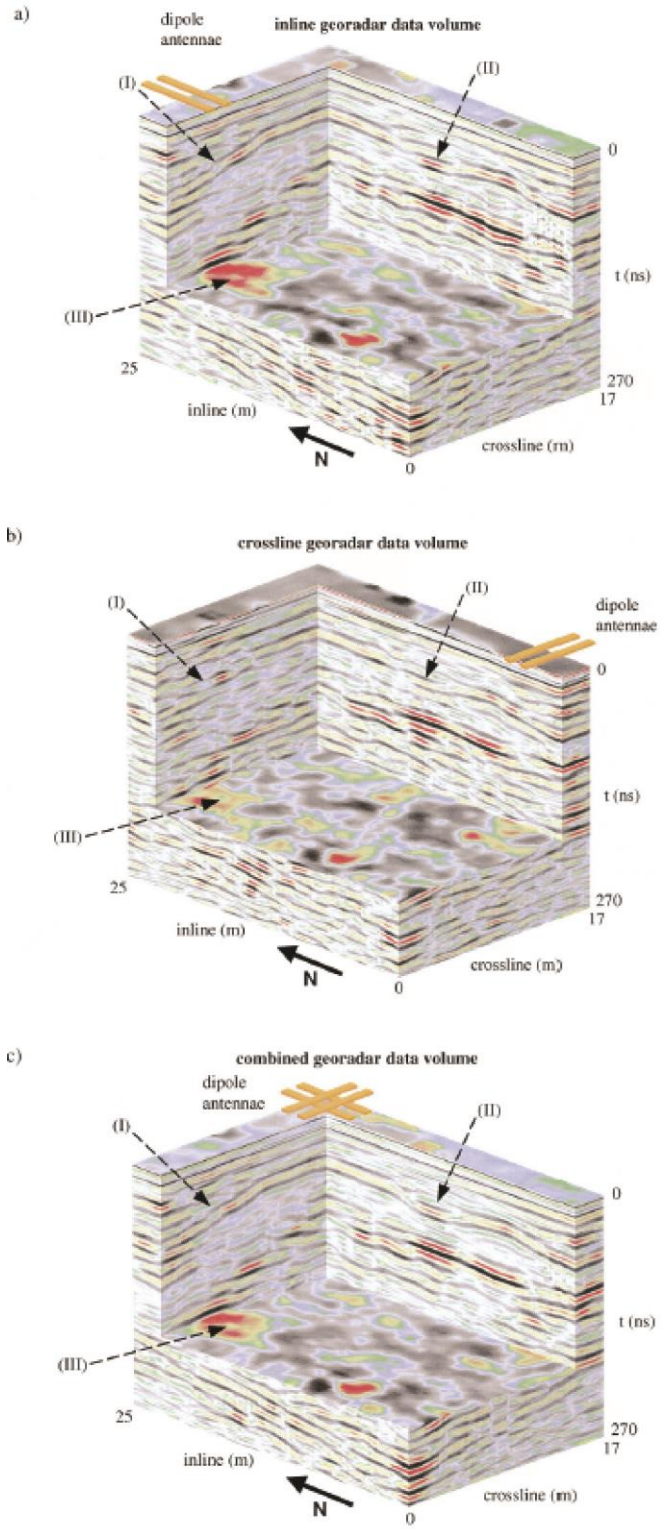

Figure 2.5: 3D migrated multipolarization GPR survey with two co-pole orthogonal polarizations. (a) Parallel to in-line direction and, (b) parallel to cross-line direction, (c) Sum of (a) and (b). Note difference in amplitude of structural features (I-III) (From Lehmann et al., 2000).

2.4 Scattering Matrix

In a multipolarization ground based GPR survey there can be four polarizations used to image a target, two co-polarized and two cross-polarized. The scattering matrix S(t) represents the target response in the time domain from these four polarizations (Equation 7) where the first subscript in the elements of the matrix represents transmitter direction and the second subscript corresponds to receiver orientation. (Sato and Miwa 2000; Chen et al., 2001; Seol et al., 2001; Sassen and Everett 2009; Villela and Romo 2013).

$$S(t) = \begin{pmatrix} S_{xx} & S_{xy} \\ S_{yx} & S_{yy} \end{pmatrix} \quad (7)$$

The co-polarized components are the diagonal elements and the off diagonal elements are the cross-polarize components responses. Few studies have been conducted to investigate the response of targets in the subsurface using all four polarizations in the scattering matrix.

Roberts and Daniels (1996) investigated the GPR polarization anomaly by analyzing responses from buried cylinders and flat planes using models and field data. They used antennas in two orientations, the first with the transmitter and receiver parallel (co-polarized), and the second receiver perpendicular to the transmitter (cross-polarized). The co-polarized orientation was shown to generate strong responses from flat planes and gave maximum response from cylindrical targets when the antennas where parallel with the long axis of the cylinder. The cross-polarized orientation gave no response from the flat plane because the incident wave must be depolarized, and this does not occur for horizontal planar reflectors. Cross-polarized orientations showed response from cylinders because depolarization occurred but varies in strength depending on the orientation of the cylinder relative to the incident wave.

Studies have used the scattering matrix to characterize and image subsurface features. Chen et al., (2001) proposed a method of using the eigenvalues from the scattering matrix to

classify unexploded ordnance (UXO). The eigenvalues where then used to estimate linearity, length, orientation, and depth of UXO. Using these four characteristics they were able to distinguish between non-UXO objects and UXO objects. Sassen and Everett (2009) used the largest eigenvalue from the scattering matrix to calculate coherence volumes of fractured rock. Combining the different coherence volumes reduced the effects of polarization caused by linear antenna and allowed for delineation of subsurface features.

Sato and Miwa (2000) developed a polarimetric borehole radar system to characterize subsurface fractures. The system collects two co-pole and two cross-pole orientations allowing the scattering matrix of the target to be acquired. Through numerical modeling Sato and Miwa (2000) demonstrated that a constant aperture fracture with a rough surface causes depolarization allowing the cross-polarized components to detect the fracture (Figure 2.6). Imaging a flat plane there is no response from the cross-polarized components, but when the flat plane has roughness then depolarization occurs and the cross-polarized components can image the plane. They conclude that calibrated polarimetric radar profiles have the potential to be used for fracture classifications. Villela and Romo (2013) use the four elements of the scattering matrix to image buried cylinders. They propose three rotation-invariant quantities (Equations 8-10) that may improve subsurface imaging because they incorporate all four elements of the scattering matrix and remove the directional character of the GPR dipolar field.

$$trace(S) = S_{XX} + S_{YY} \tag{8}$$

$$det(S) = S_{XX}S_{YY} - S_{xy}S_{yx} \tag{9}$$

$$norm(S) = |S_{XX}|^2 + |S_{YY}|^2 + |S_{XY}|^2 + |S_{YX}|^2 \tag{10}$$

These quantities are created by using the four polarizations of the scattering matrix and combining them in a mathematical simple and sound manner. They tested these methods by

imaging a buried cylinder (Figure 2.7). By combining the information from multiple polarizations the cylinder was identified more accurately then using a single polarization.

These studies have established that all elements of the scattering matrix hold useful information about subsurface targets, and suggest that cross-pole polarizations from a multipolarization GPR survey can be used to identify and characterize fractures channels.

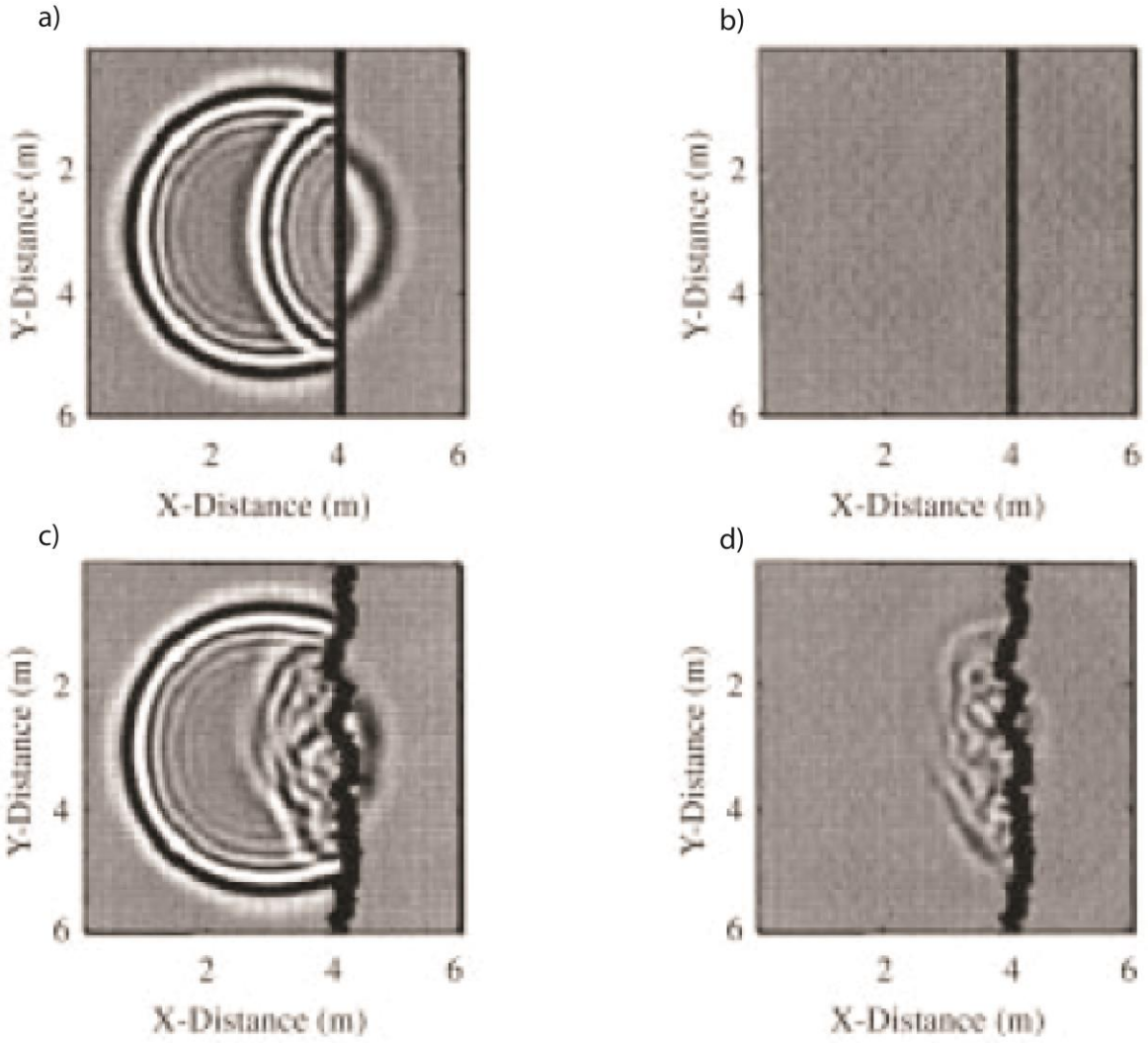

Figure 2.6: FDTD simulation from a flat fracture and rough fracture. (Top) flat (Bottom) rough. (a) Co-polarized signal, (b) Cross-polarized signal, (c) Co-polarized signal, (d) Cross-polarized signal (From Sato and Miwa, 2000).

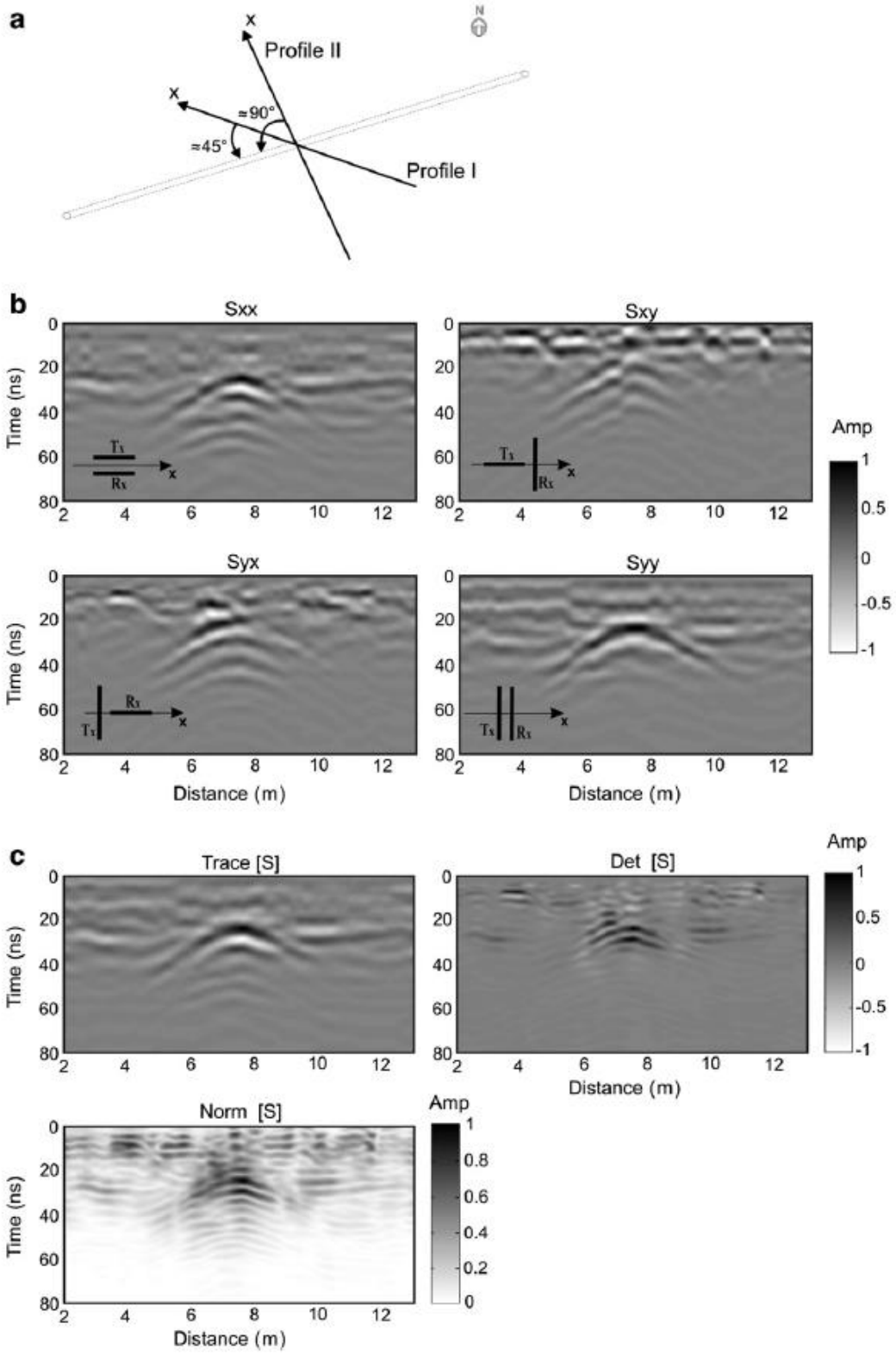

Figure 2.7: (a) Outline of an aqueduct pipe and two measured profiles, (b) Cross-sections with the elements of the scattering matrix measured for Profile 1, (c) Cross-sections of the invariant quantities. After filtering the direct arrival the amplitude of the components were normalized for plotting purposes (From Villela and Romo 2013).

Chapter 3: 3D FDTD Numerical Modeling of GPR Fracture Channel Imaging

3.1 Methods

3.1.1 Horizontal Fracture

3D FDTD modeling was used to evaluate the effects of GPR signal polarization, varying water electrical conductivity, and aperture on a horizontal fracture. Rock-matrix parameters were $\varepsilon_r = 7$, $\sigma = 0$ mS/m and water $\varepsilon_r = 80$ similar to the Altona Flat Rock site. Four polarizations were modeled simulating data acquisition at the Altona Flat Rock Site using source frequencies of 50 and 100 MHz (Figure 3.1). The fracture water electrical conductivity was set to 28 mS/m to simulate background fresh water conditions, as well as 180 mS/m, 400 mS/m, and 700 ms/m to simulate varying saline tracer concentration. Fracture aperture was set to 0.01 m, 0.02 m, 0.05 m, and 0.1 m. Model grid size was 0.01 m and dimensions were 3.0 m x 3.0 m x 3.0 m with the horizontal fracture located at 2.0 m depth (Figure 3.2). Source receiver separation was 0.1 m and a single trace was simulated with each polarization for the varying fracture properties described above. Figure 3.3a shows 50 and 100 MHz frequency traces simulated from an "empty" model, containing no fracture, and a model containing a 0.01 m horizontal fracture filled with 28 mS/m conductivity water referenced as the "background" model. To enhance visualization of the results the empty model (no fracture) is subtracted from model containing a fracture with varying properties as described above (Figure 3.3b). Subtracting the empty model trace removes the high amplitude direct arrival as well as reflected energy from the model boundaries. In addition all results (co-polarized and cross-polarized) are normalized to the background horizontal fracture amplitude from the co-polarized signals with water eclectical conductivity of 28 mS/m and fracture aperture of 0.01 m (Figure 3.3c). The normalization was done to highlight amplitude changes from the background horizontal fracture amplitude.

Normalized amplitudes near one are similar in strength to the fracture reflection from background horizontal fracture. These two processing steps are applied to all modeling results presented in this chapter except figures 3.16-3.20.

3.1.2 Fracture Channel

Numerical models of a horizontal fracture containing a channel were also run to assess GPR signal polarization effects on the reflected signal. Fracture aperture remained constant at 0.01 m and the water electrical conductivity was set to fresh water conditions of 28 mS/m. A simulated channel was inserted along the y-axis and the geometry and properties were changed to analyze polarization effects (Figure 3.4). Models were run with a channel simulated by a box that increased the fracture aperture to 0.02 m. Channel widths simulated were 0.6 m, 0.2 m, 0.1 m, and 0.02 m (Figure 3.4a). The fracture channel was then simulated by inserting a cylinder along the y-axis with a diameter of 0.06 m (Figure 3.4b). In subsequent models the 0.06 m cylinder was reoriented to cross the source and receivers at a 45^{o} angle to enhance the cross-polarized signals (Figure 3.4c). Additionally, the cylinder's electrical conductivity was increased to 180 mS/m, 400 mS/m, and 700 mS/m to simulate varying saline tracer concentration. Co-polarized and cross-polarized traces, generated using the configurations shown in figure 3.1, were simulated at a single location over channels as shown in figure 3.4.

3.1.3 Fracture Channel Survey Line

The last set of models where run with a cylinder oriented first along the y-axis (or 0^{o} to the y-axis) and then at a 45^{o} angle to the y-axis. The GPR survey line was simulated in the x-direction with a trace spacing of 0.1 m. (Figure 3.5). Fracture aperture remained 0.01 m with water electrical conductivity of 28 mS/m. Each polarization profile was 2D migrated using a velocity of 0.11 m/ns. The co-polarized signals had a horizontal background fracture model

subtracted. Then the co-polarized signals (P1 and P3) and the cross-polarized signals (C1 and C3) were summed and compared. These data sets are similar to field acquisition geometries used at the Altona Flat Rock site.

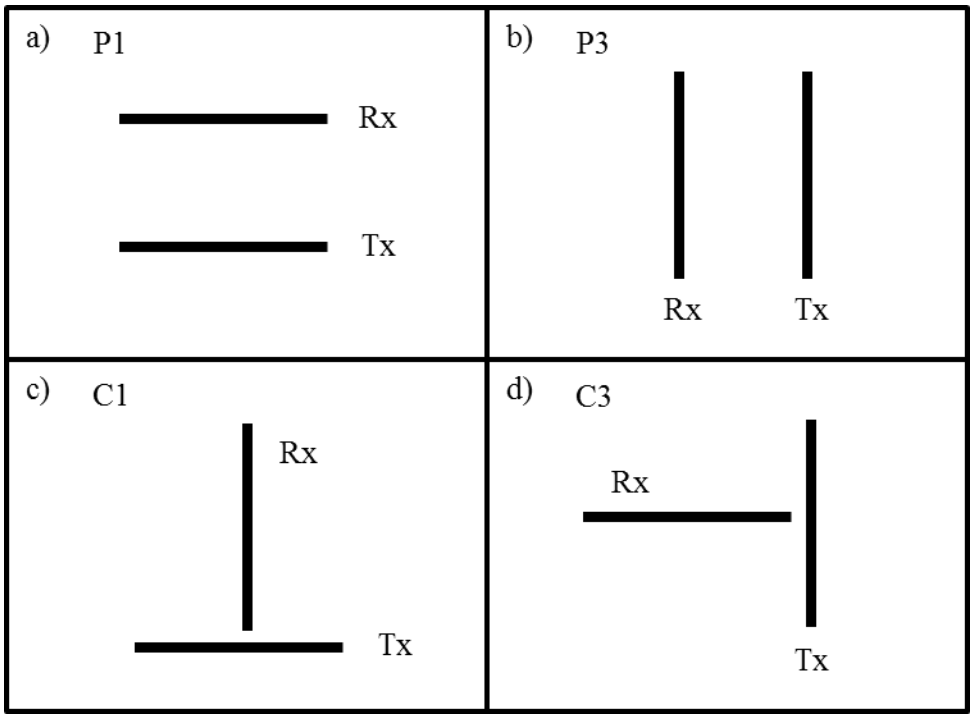

Figure 3.1: Co-polarized and cross-polarized source and receiver orientations. Tx stands for source and Rx for receiver. a) P1 polarization oriented along x-axis, b) P3 polarization oriented along y-axis, c) C1 polarization with source oriented along x-axis, d) C3 polarization with source oriented along y-axis.

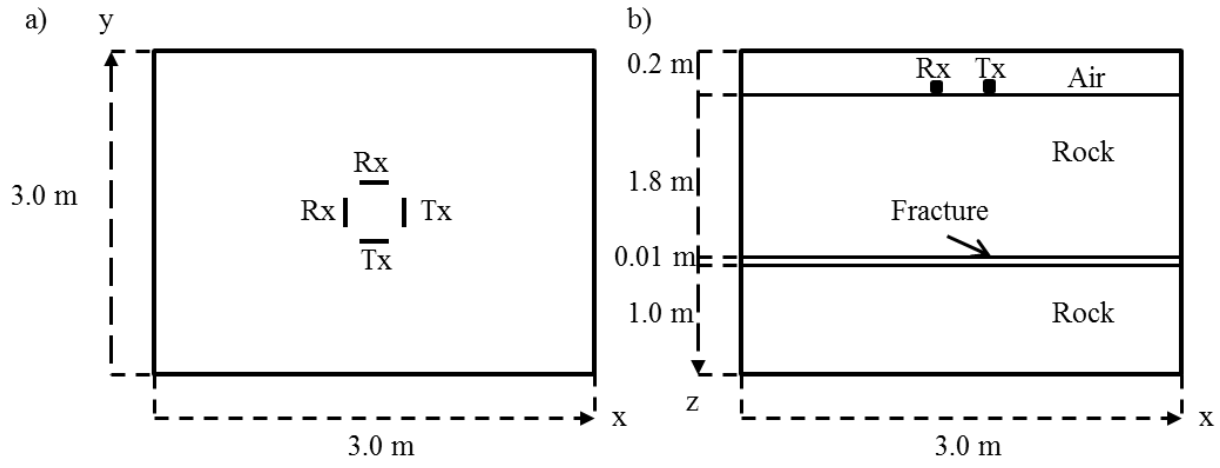

Figure 3.2: 3D FDTD model geometry (not to scale). a) Map view with source and receiver locations identified, b) Cross-section view with fracture at 1.8 m depth.

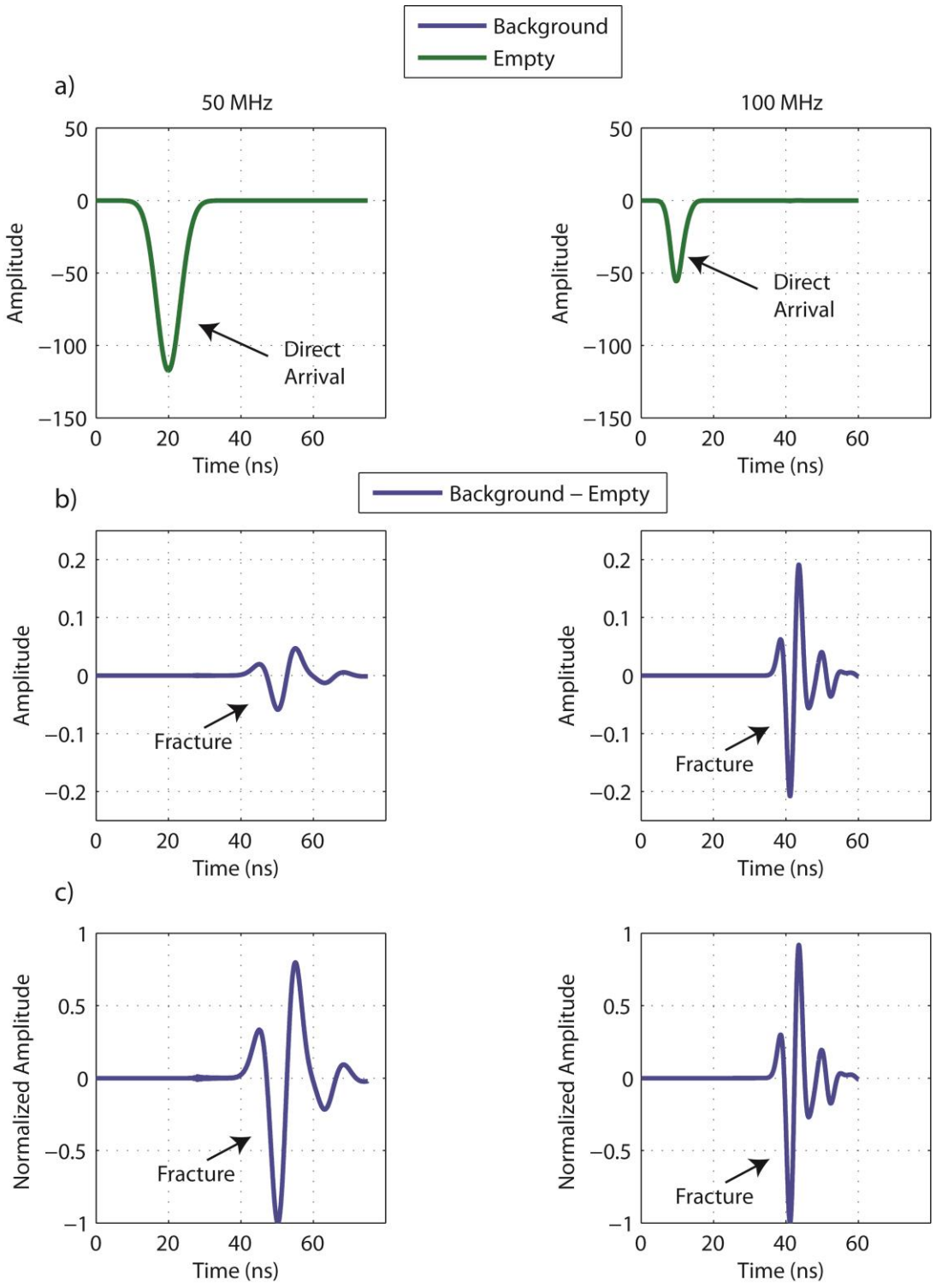

Figure 3.3: (Left) 50 MHz and (Right) 100 MHz signals. Fracture aperture 0.01 m and water electrical conductivity set to 28 mS/m. a) Empty model and background model, b) Background model after subtracting empty model, c) Background model after normalization. Subtracting the empty model and normalizing to background electrical conductivity removes the direct arrival and helps visualization of fracture reflection.

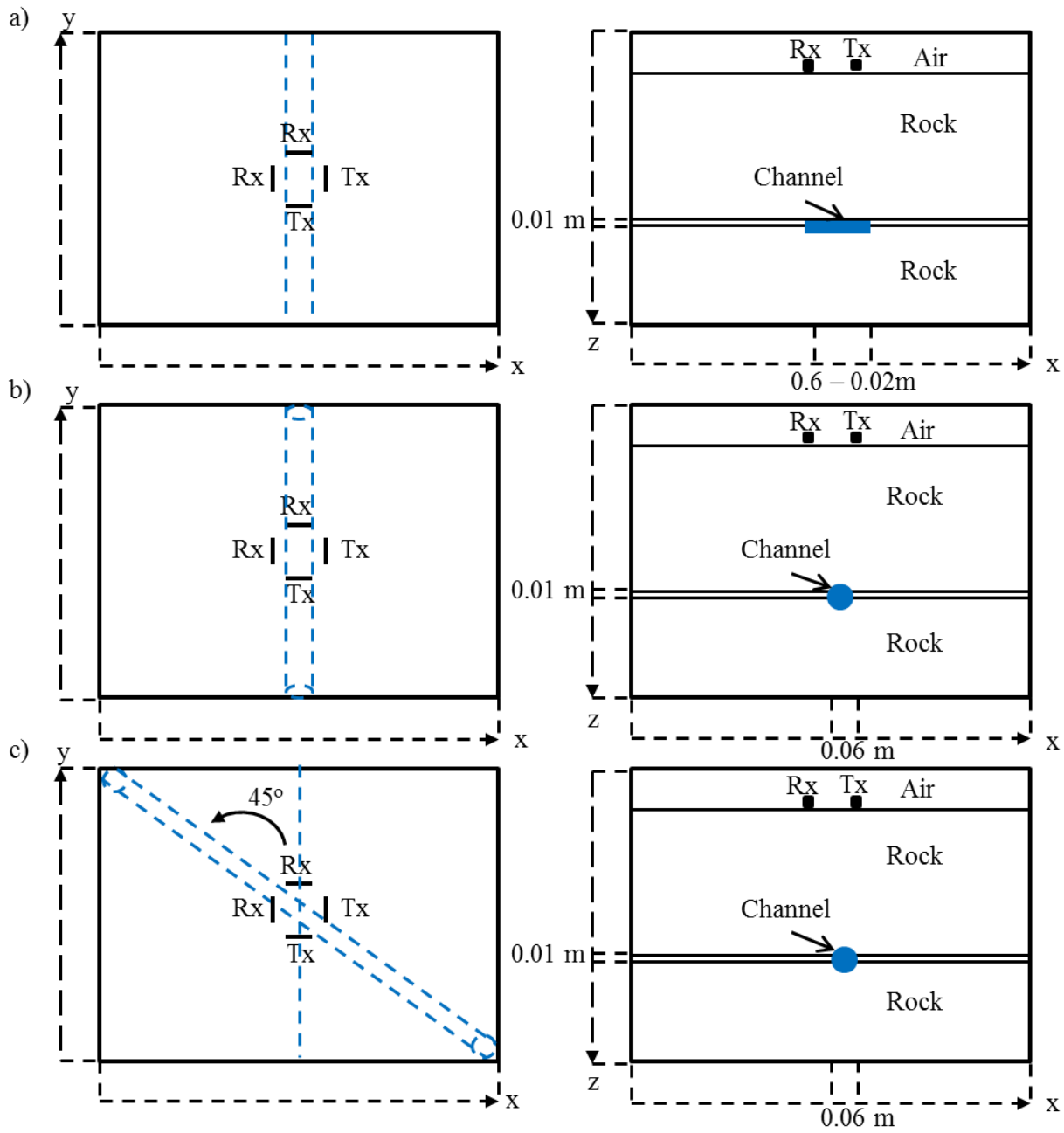

Figure 3.4: 3D FDTD model geometries for channel models (not to scale). (Left) Map view and (Right) cross-section view. Fracture water electrical conductivity 28 mS/m. a) Channel simulated by box increased fracture aperture to 0.02 m and varied in width from 0.6m – 0.02m., b) Channel simulated by cylinder with diameter of 0.06 m. Fracture water electrical conductivity set to 28 mS/m, 180 mS/m, 400 mS/m, and 700 mS/m, c) Cylinder rotated 45^{o} to enhance cross-polarized responses. Fracture water electrical conductivity set to 28 mS/m, 180 mS/m, 400 mS/m, and 700 mS/m.

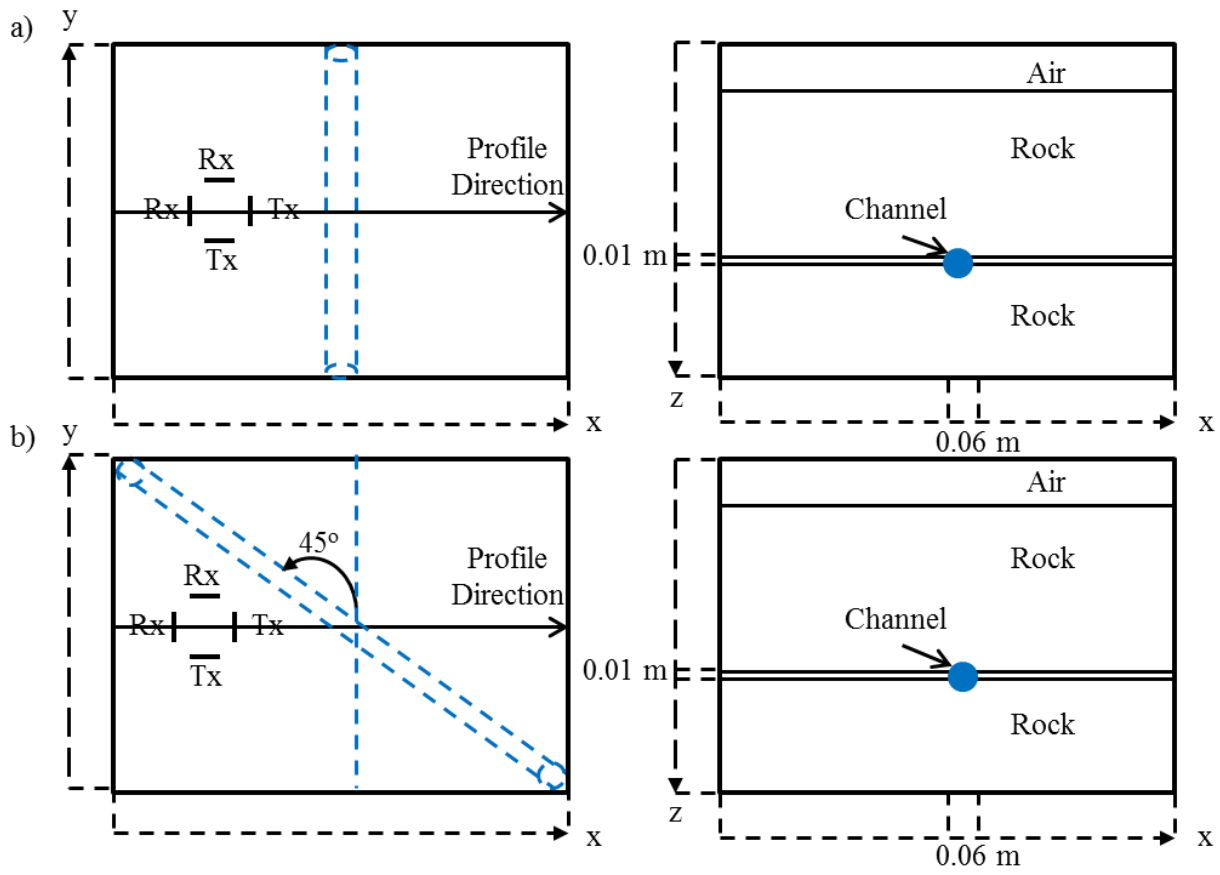

Figure 3.5: 3D FDTD model geometry for channel model with survey line in x-direction to simulate field acquisition (not to scale). (Left) Map view and (Right) cross-section view. Fracture water electrical conductivity set to 28 mS/m. a) Cylinder is oriented 0^{o} (along y-direction) to source and receivers to generate differences in co-polarized responses, b) Cylinder is orientated 45^{o} (oblique) to sources and receivers to generate maximum cross-polarized response.

3.2 Results

3.2.1 Horizontal Fracture

An analytical model was generated using the same method described by Tsoflias and Becker (2008) to examine fracture reflection coefficient (R) strength for 50 and 100 MHz frequency radar signals when fracture aperture varied from 0.0 m to 0.1 m with water electrical conductivity set to 28 mS/m (Figure 3.6). The 100 MHz frequency shows stronger R magnitudes than the 50 MHz, as expected from higher frequency signals illustrated in Figures 3.3b and 3.7a. After normalization the 50 MHz frequency signal shows greater amplitude change with increasing fracture aperture than the 100 MHz (Figure 3.7b).

The fracture response from all four polarizations (Figure 3.1) for a horizontal fracture with varying aperture and water electrical conductivity are show in figures 3.8-3.10. With increasing fracture aperture both 50 and 100 MHz co-polarized signals (P1 and P3) show increasing fracture reflection amplitude except for the 100 MHz 0.1 m fracture aperture (Figure 3.8). For a water saturated fracture 0.1 m wide, the 100 MHz signal can resolve the top and bottom of the fracture and therefore reflection amplitude is not proportional to fracture aperture. These results are in agreement with theory (Balanis, 1989) that when imaging thin layers (i.e. thickness $< \lambda/4$), increasing layer thickness increases the reflected amplitude. A phase delay also occurs caused by increased fracture aperture. With increasing water electrical conductivity in the fracture, both 50 and 100 MHz co-polarized signals show increasing fracture reflection amplitude and an increasing phase lag (Figure 3.9). The 50 MHz data show a greater change in fracture reflection amplitude and phase lag than the 100 MHz data. The greater phase lag and greater difference in amplitude between the various water electrical conductivities indicate that 50 MHz data would be better at distinguishing changes in electrical conductivity than 100 MHz

data as suggested by Tsoflias and Becker (2008). As predicted by EM theory (Balanis, 1989), normal and near-normal incidence reflection from planar interfaces is polarization independent. The only difference between P1 and P3 for a flat fracture is computational noise, as shown by the difference between P1 and P3 in figures 3.8c and 3.9c. Cross-polarized signals C1 and C3 show no appreciable reflected energy from the horizontal fracture. Horizontal interfaces do not cause normally incident GPR signals to depolarize and therefore the reflected energy remains oriented parallel to the source signal orientation. No signal component is detected in the cross-polarized orientation (Figure 3.10).

3.2.2 Horizontal Fracture Modeling Result Summary

1. Increasing fracture aperture or the fluid electrical conductivity will increase fracture refection amplitude in co-polarized signals.
2. 50 MHz signals show greater change in reflection amplitude and phase lag than 100 MHz signals, indicating that 50 MHz signals would be better at distinguishing changes in electrical conductivity during a saline tracer test.
3. Cross-polarized signals cannot detect horizontal planar targets.

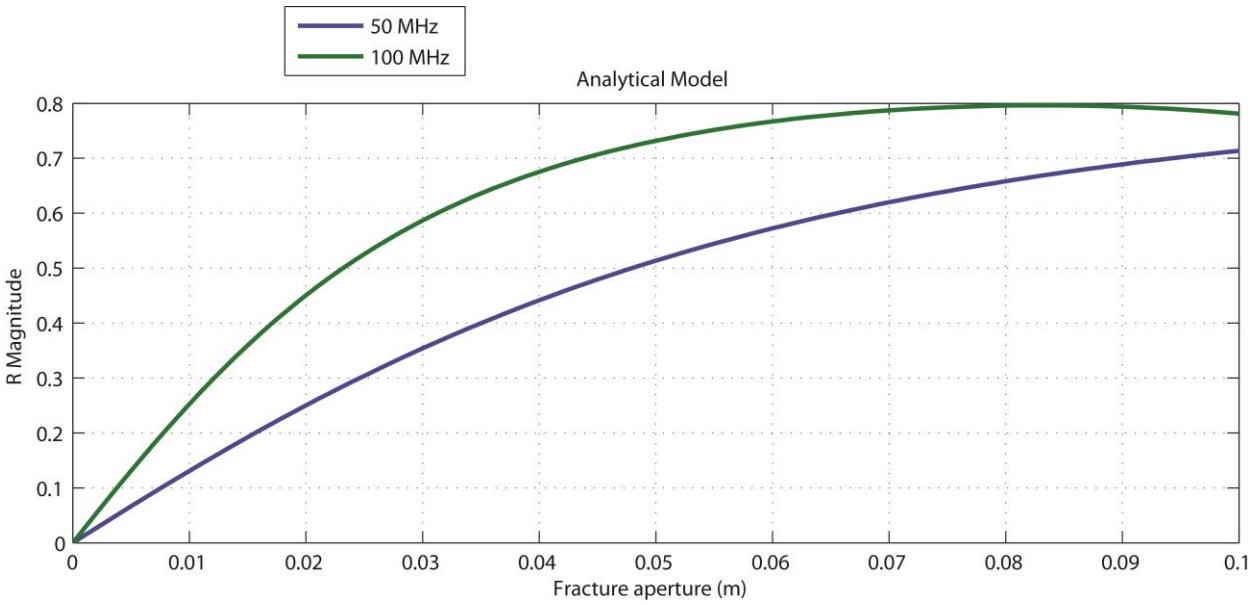

Figure 3.6: Analytical models of facture reflection coefficient (R) using 50 and 100 MHz frequencies. Fracture aperture varies from 0 to 0.1 m and water electrical conductivity is set to 28 mS/m.

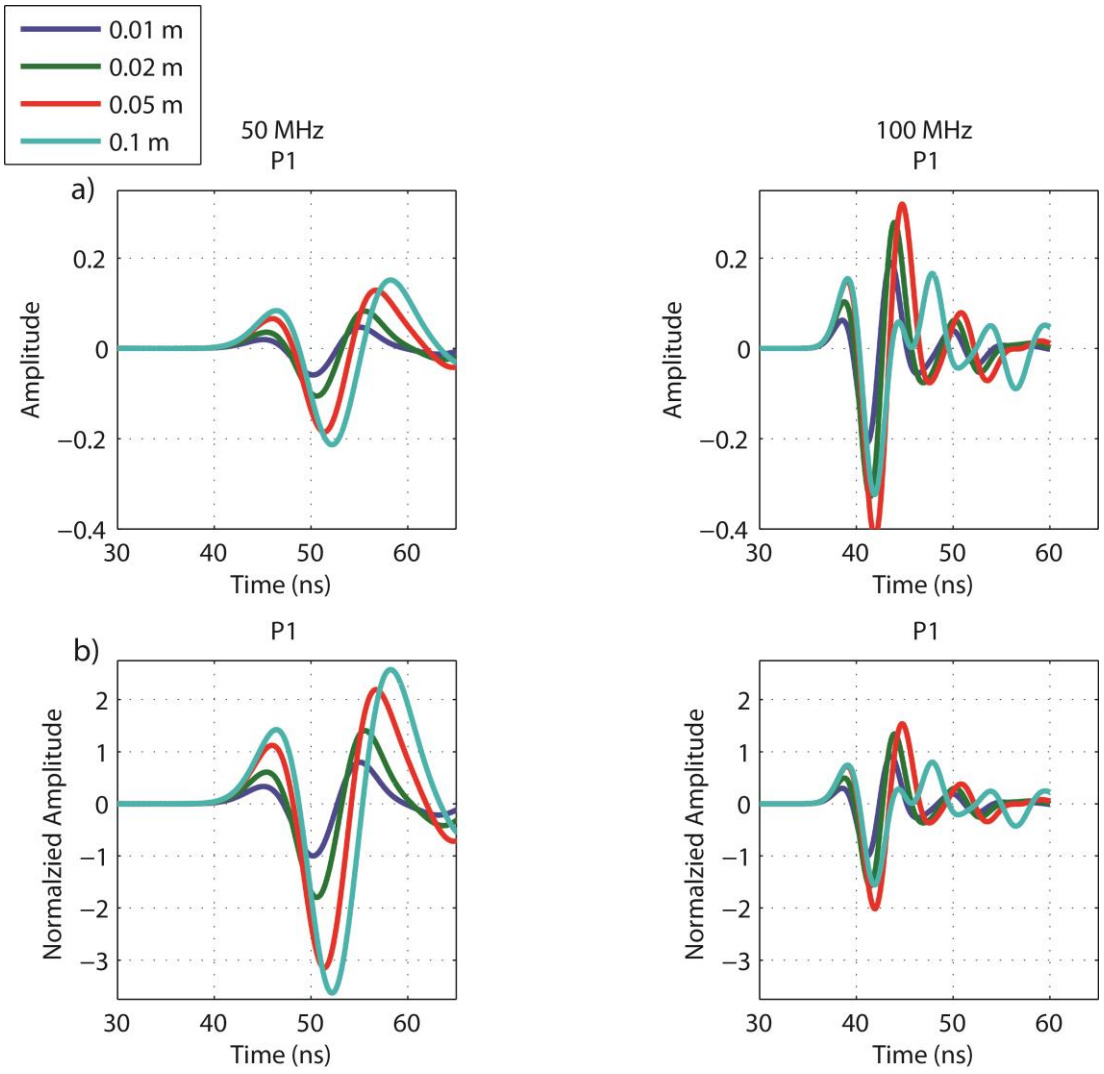

Figure 3.7: Horizontal fracture models with varying aperture. Water electrical conductivity 28 mS/m. (Left) 50 MHz (Right) 100 MHz. a) P1 non-normalized, b) P1 normalized to the reflection amplitude of a 0.01 m aperture with water electrical conductivity of 28 mS/m.

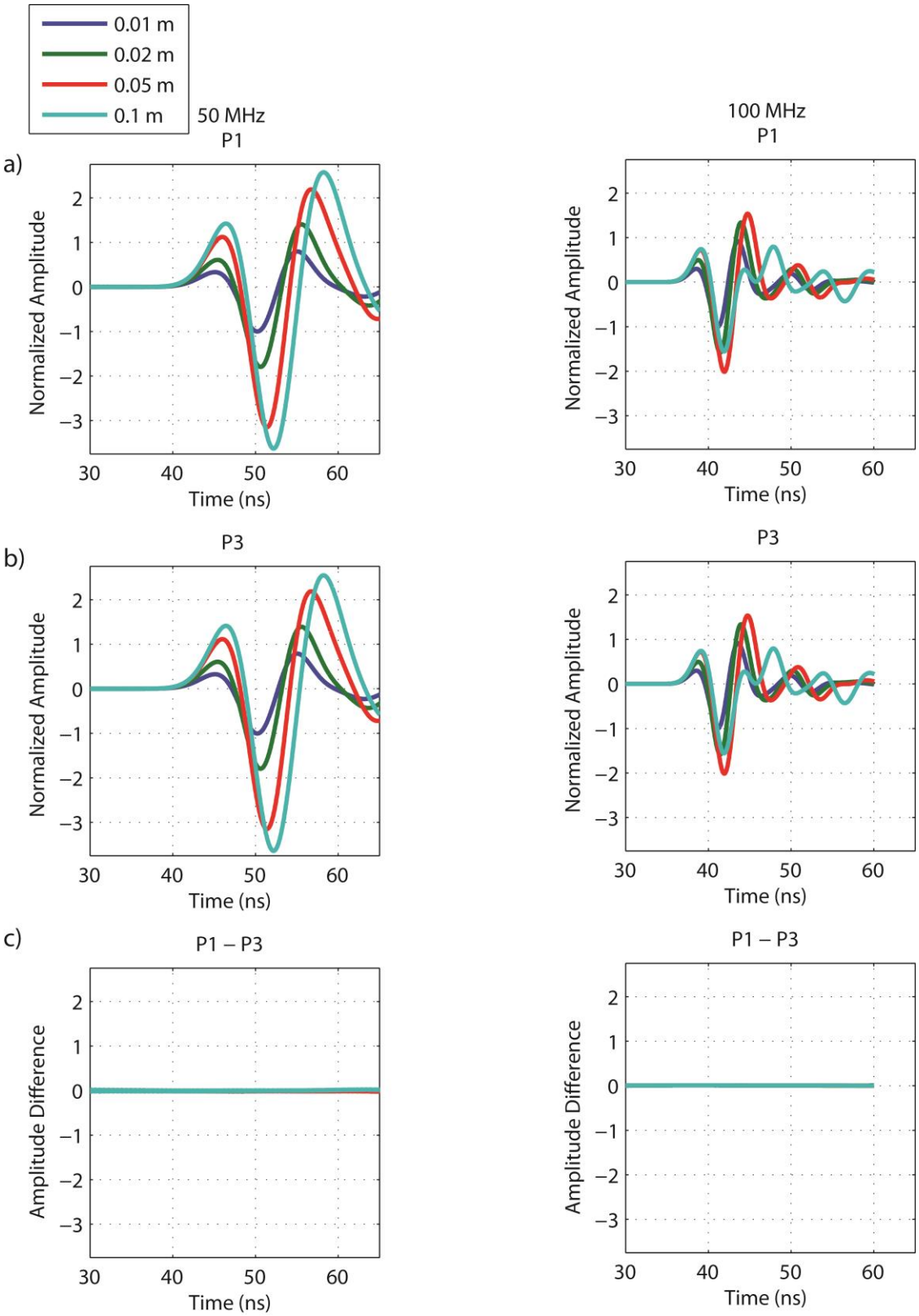

Figure 3.8: Models of co-polarized GPR signal response to varying fracture aperture. Water electrical conductivity 28 mS/m. (Left) 50 MHz (Right) 100 MHz. a) P1, b) P3, c) P1-P3.

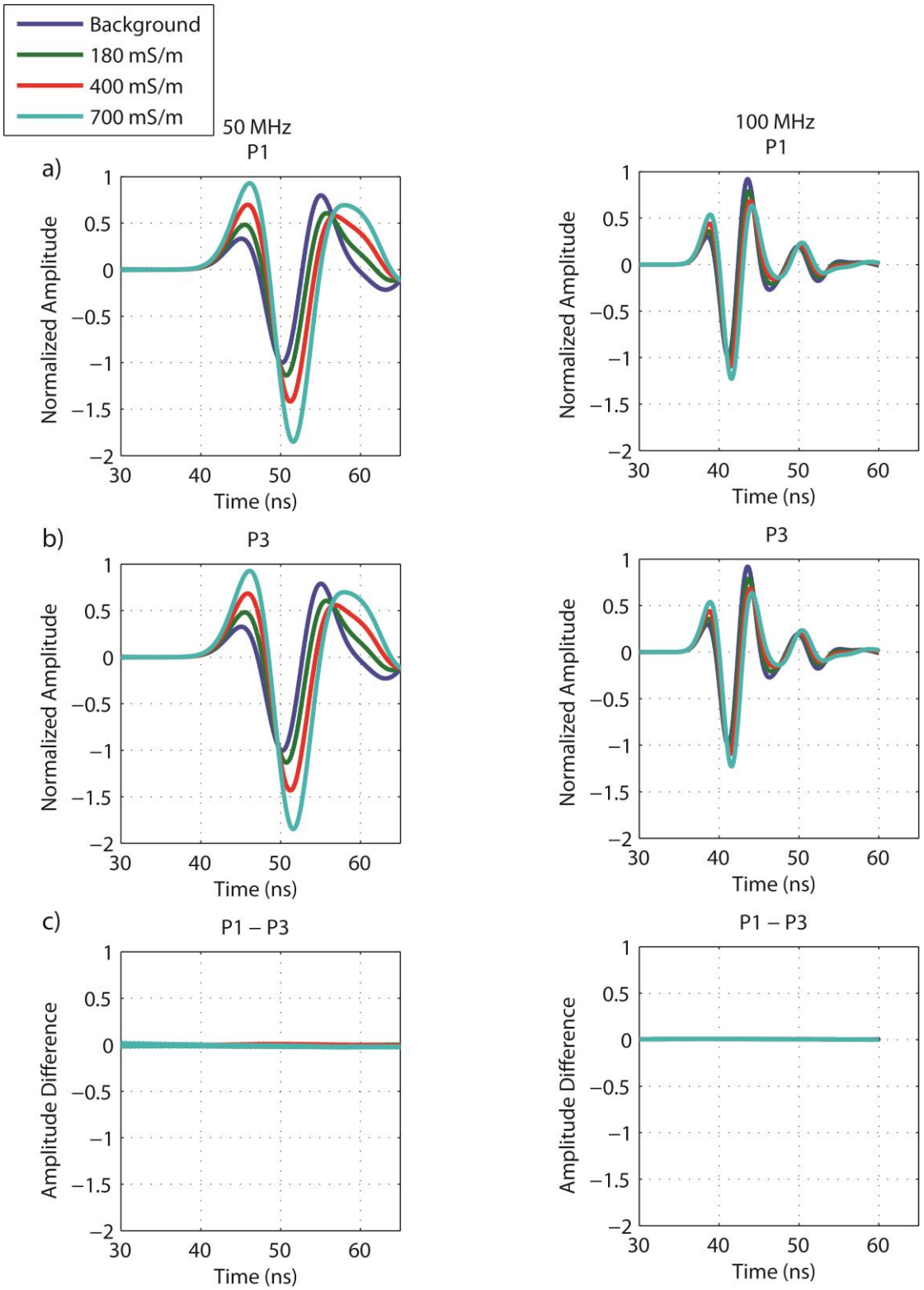

Figure 3.9: Models of co-polarized GPR signal response to varying water electrical conductivity. Fracture aperture 0.01 m. (Left) 50 Mhz (Right) 100 MHz. a) P1, b) P3, c) P1-P3.

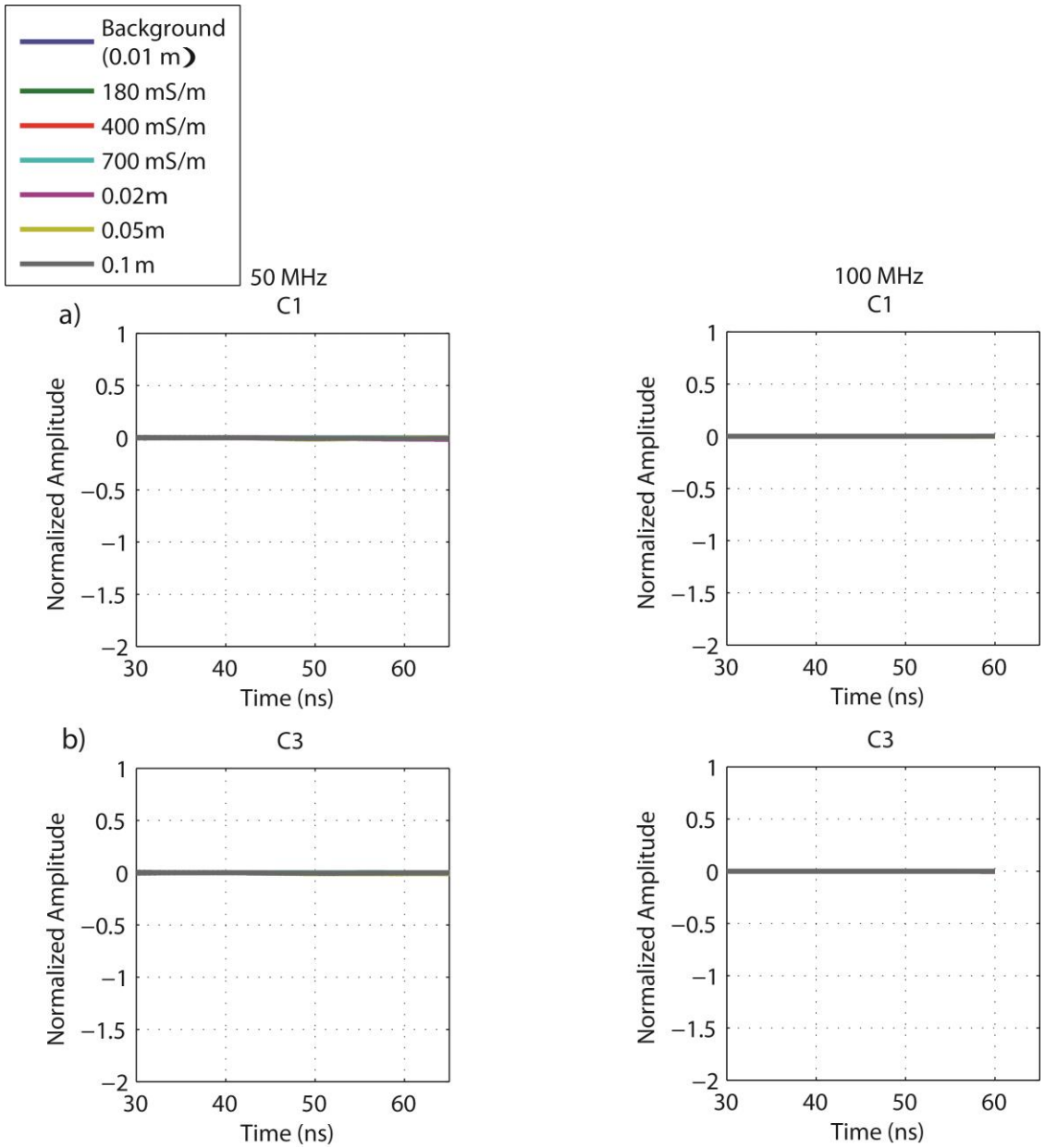

Figure 3.10: Models of cross-polarized GPR signal response to varying water electrical conductivity and fracture aperture. (Left) 50 MHz (Right) 100 MHz. a) C1, b) C3. No reflected signal is detected by cross-polarized componets.

3.2.3 Fracture Channels

Modeling responses of the rectangular channel (Figure 3.4a) with a fracture aperture of 0.02 m are plotted in figure 3.11. Both 50 and 100 MHz experimental results show that increasing the channel width increases the reflected amplitude response. Furthermore a rectangular channel exhibits small polarization effects in co-polarized signals as shown by the difference (P3 – P1) plots in figure 3.11c.

The modeling results from the experiment using a 0.06 m cylinder oriented in the y-direction (0^o) (Figure 3.4b) are displayed in Figures 3.12-3.13. Significant differences in amplitude responses are seen in the co-polarized signals with P3 giving a stronger response than P1 (Figure 3.12). P3 polarization has the E-field oriented parallel with the channel and for P1 the E-field is perpendicular to the channel. The difference in the co-polarized signals is caused by the E-field orientation. When the E-field is parallel with cylinder (P3) more energy is returned to the receiver, consistent with the findings by Roberts and Daniels (1996). Increasing the water electrical conductivity increases the amplitude response in both frequencies, but the P3 signal still demonstrates a stronger response than the P1 signal due to the orientation of the cylinder. There is no response from the cross-polarized signals because no depolarization occurs (Figure 3.13) when the impinging signal is at 0^o or 90^o to the axis of the channel.

Figures 3.14-3.15 show co-polarized and cross-polarized signals from a 0.06 m cylinder oriented 45^o relative to the sources and receivers (Figure 3.4c). The co-polarized signals P1 and P3 (Figure 3.14ab) show same amplitude and phase response as expected due to symmetry. The only difference is computational noise (Figure 3.14c). The cross-polarized signals give an amplitude response approximately an order of magnitude less that the co-polarized signals with reversed polarity (Figure 3.15). This result is similar to Lehman et al. (2000), where cross-

polarized and co-polarized signals were used to image a point scatterer, resulting in co-polarized data showing a strong reflection and cross-polarized data a weak opposite polarity reflection. Increasing the cylinder water electrical conductivity increases the amplitude response for both frequencies with the the co-polarized signals (Figure 3.14ab). Amplitude increase is the same in both co-polarized signals as show in difference between P3 and P1 (Figure 3.14c).The cross-polarized signals also show an increase in amplitude due to increased water electrical conductivity (Figure 3.15ab). The amplitude increase is the same in both cross-polarized signals as shown in difference plot of C3 – C1 (Figure 3.15c)

Next the reflection strengths from both co-polarized and cross-polarized cylinder models were analyzed using the amplitude envelope (Figures 3.16-3.20). The amplitude envelope is computed using the magnitude of the Hilbert transform of the traces, which is used to estimate reflection strength (Tanner et al., 1979). Figure 3.16 shows 50 and 100 MHz GPR traces along with the computed amplitude envelopes. Figures 3.17-3.20 plot the amplitude envelope of the co-polarized and cross-polarized signals from 0^o and 45^0 cylinder models for both frequencies and for varying water electrical conductivity. For co-polarized signals P3_0^o is strongest, P1_0^o the weakest, and P1_45^o P3_45^0 exhibit the same strength but fall between P3_0^o and P3_0^o (Figures 3.17a-3.20a). 50 MHz signals show greater difference in signal strength between the polarizations than the 100 MHz signals. The cross-polarized C1_45^0 and C3_45^0 signals are significantly weaker than the co-polarized signals. C1_0^0 and C3_0^o are not plotted because they did not receive any reflected energy from the cylinder. These observations are in agreement with the trace amplitudes observed in the single trace models presented earlier (Figures 3.12-3.15).

To compare the energy between 0^o and 45^o cylinder models, the vector sum of the polarization components are plotted together (Figures 3-17b-3.20b).

$$\text{Vector Sum } 0^o = \sqrt{P1^2 + P3^2} \quad (11)$$

$$\text{Vector Sum } 45^o = \sqrt{P1^2 + P3^2 + C1^2 + C3^2} \quad (12)$$

It is observed that the energy in Equation 11 equals the energy Equation 12. The vector sums combine reflected energy from all polarization components into one value. This suggests that the vector sum could be a technique used to combine all parts of the scattering matrix (Equation 7) and represent the total reflected energy. The scattering matrix represents the target response in the time domain from four polarizations that can be acquired with ground based GPR (Villela and Romo 2013).

3.2.4 Fracture Channels Result Summary

1. A fracture channel oriented orthogonal or parallel to sources and receivers will cause the co-polarized component that is parallel with the axis of the channel to show greater reflected amplitude than the component perpendicular to the channel.
2. The cross-polarized components will not detect a channel oriented parallel or orthogonal to the sources and receivers.
3. For a fracture channel oriented oblique (45^0) to source and receiver, the co-polarized signals have same amplitude due to symmetry, and the cross-polarized signals can detect the channel. The cross-polarized signal is weaker than, and opposite in polarity to the co-polarized signal.
4. Increasing the electrical conductivity in both orthogonal and oblique cylinders increases the amplitude response in co-polarized and cross-polarized signals.

5. The use of vector sums of the co-polarized and cross-polarized signals could be a way to combine all parts of the scattering matrix and produce an accurate image of the fracture channel.

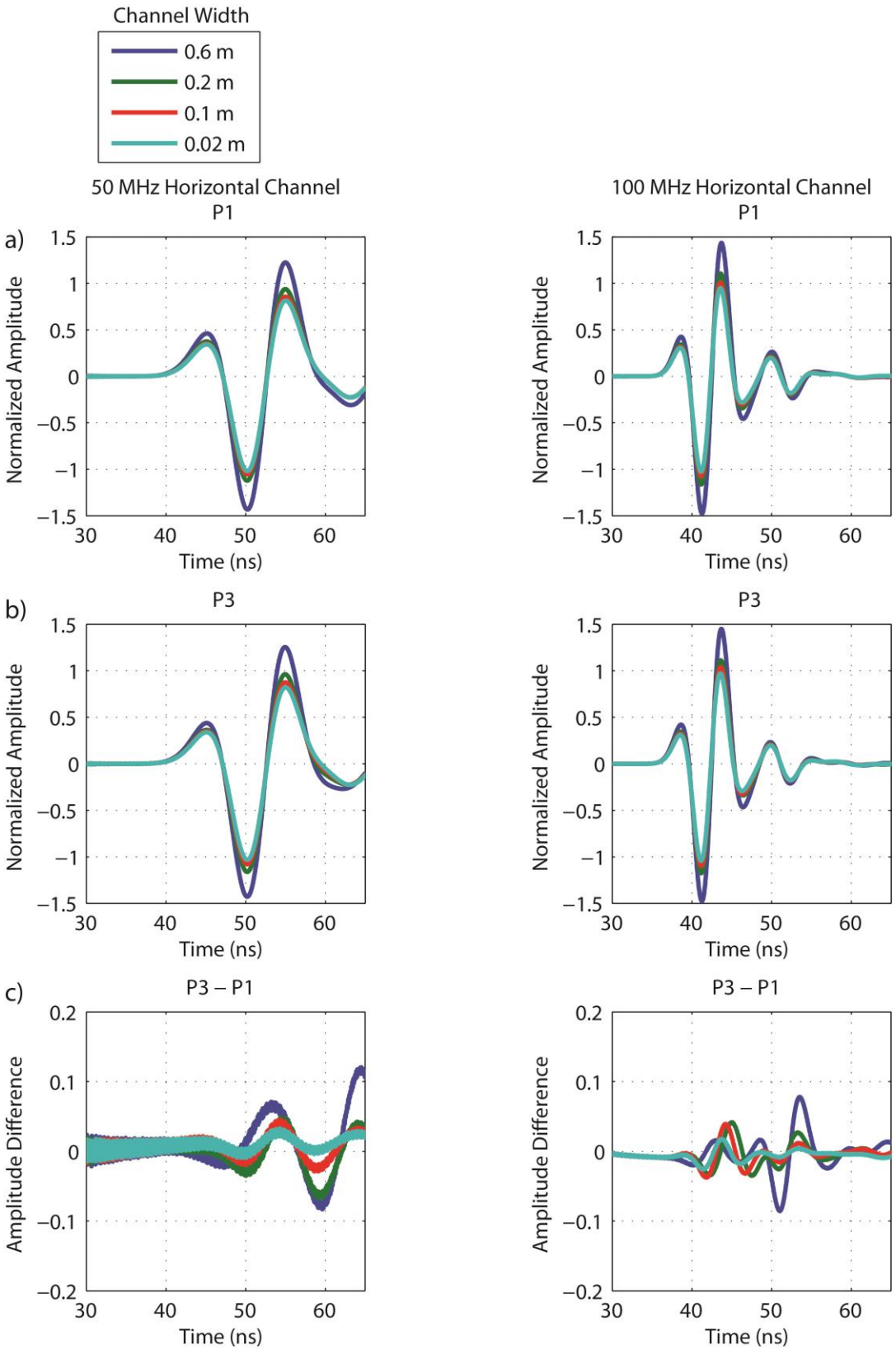

Figure 3.11: Rectangular channel model amplitude responses. Water electrical conductivity 28 mS/m. (Left) 50 MHz (Right) 100 MHz. a) P1, b) P3, C) P3-P1.

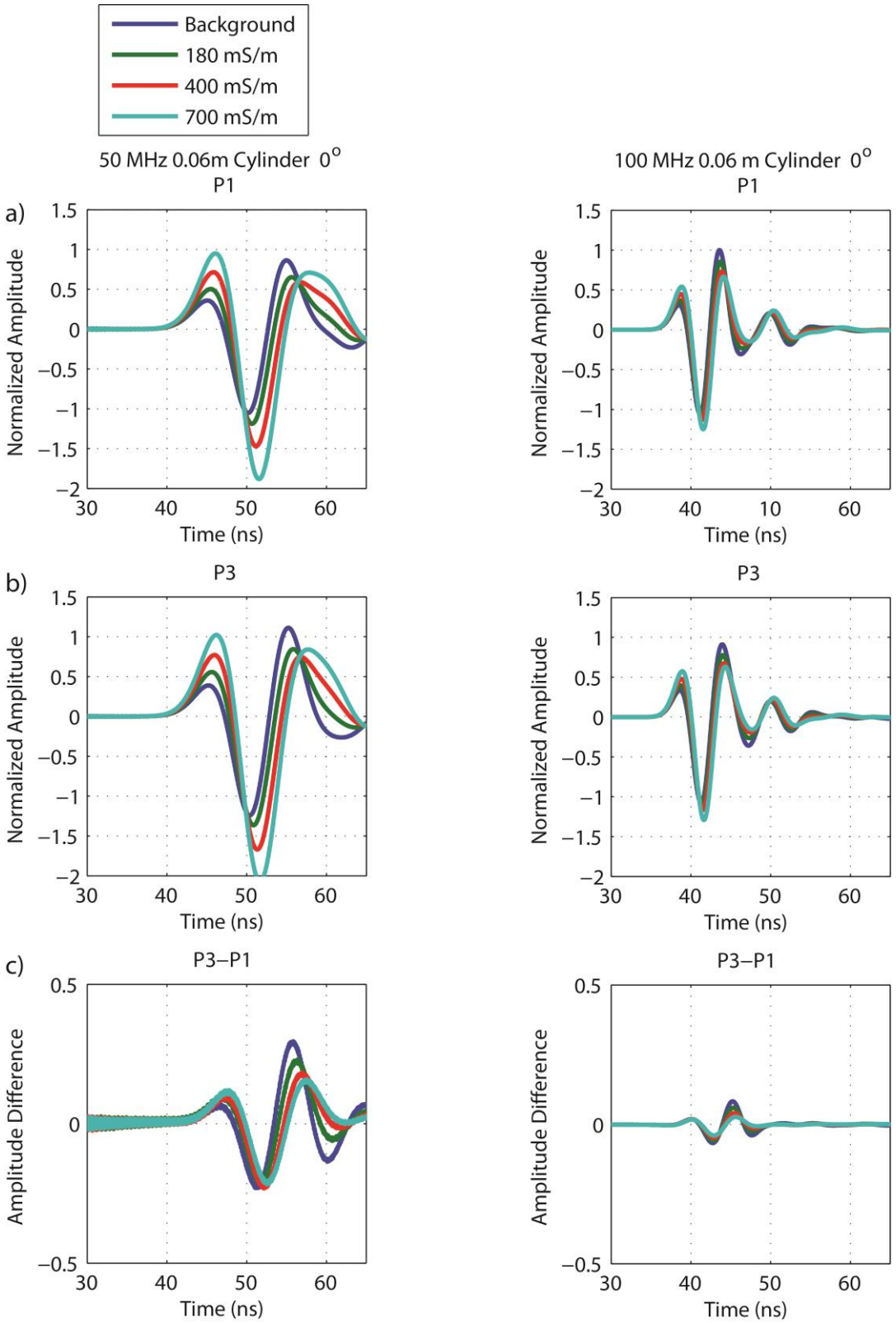

Figure 3.12: Co-polarized cylinder models oriented in the y-direction. (Left) 50 MHz (Right) 100 MHz. a) P1, b) P3, c) P3-P1.

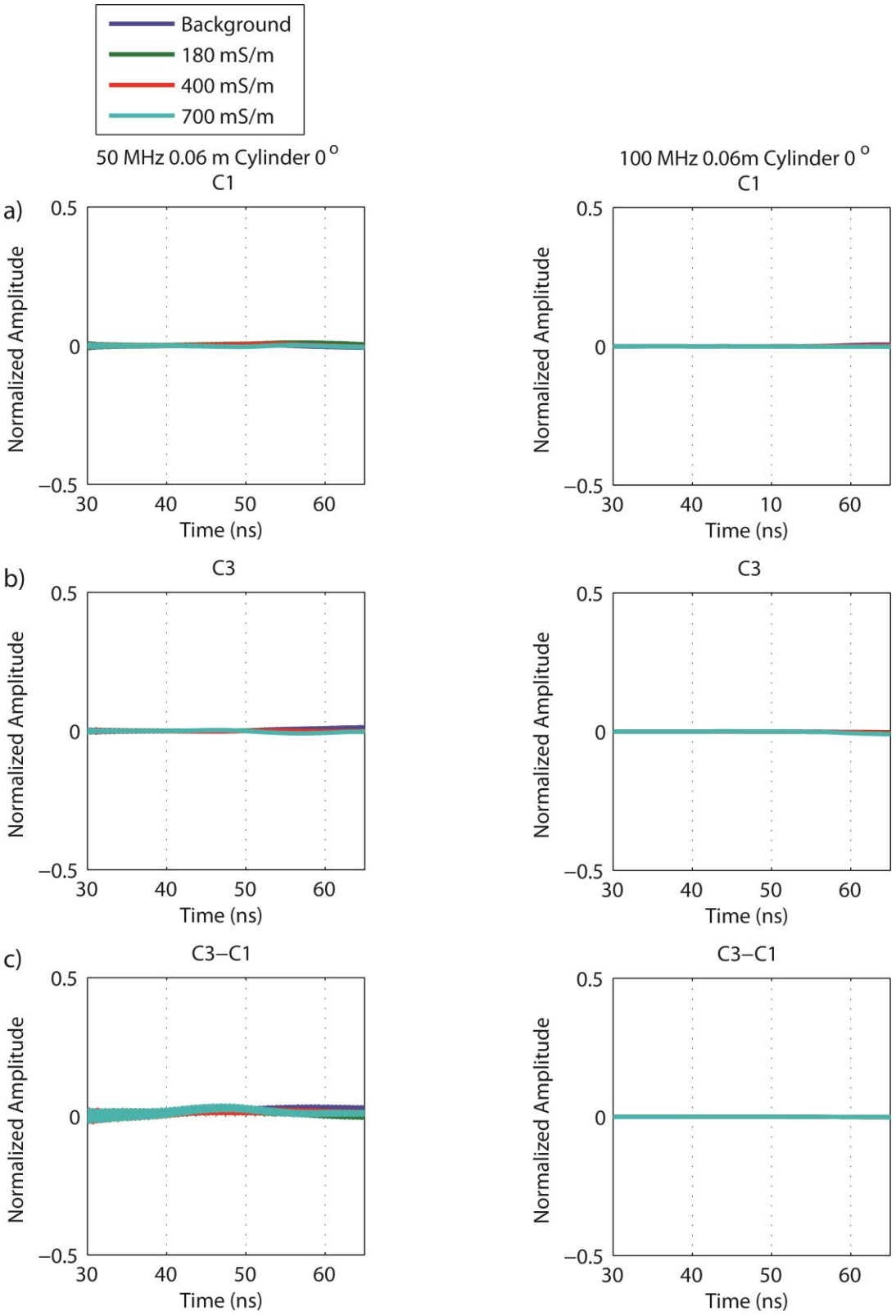

Figure 3.13: Cross-polarized cylinder models oriented in the y-direction. (Left) 50 MHz (Right) 100 MHz. a) C1, b) C3, c) C3-C1.

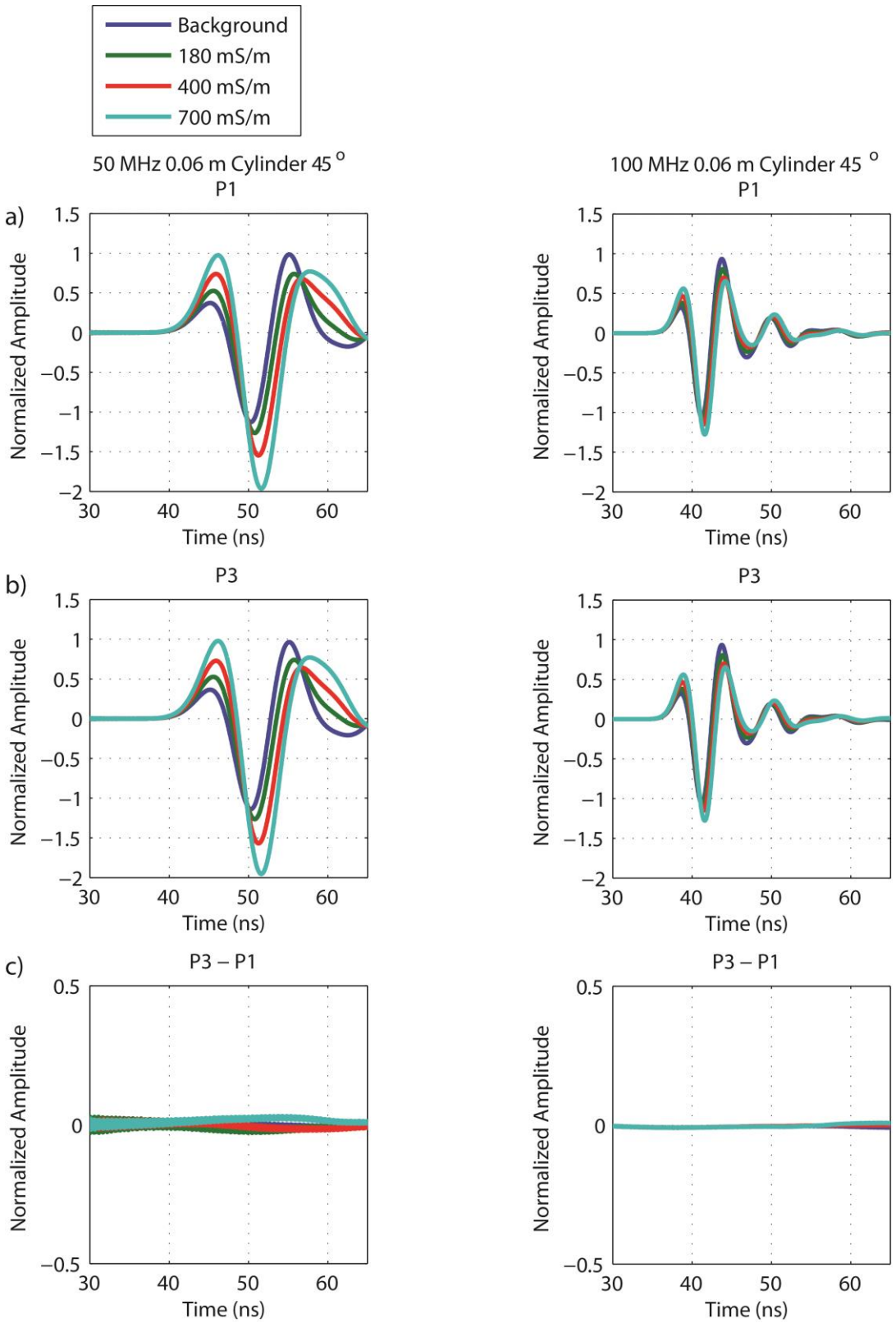

Figure 3.14: Co-polarized cylinder models oriented 45° to source and receiver. (Left) 50 MHz (Right) 100 MHz. a) P1, b) P3, c) P3-P1.

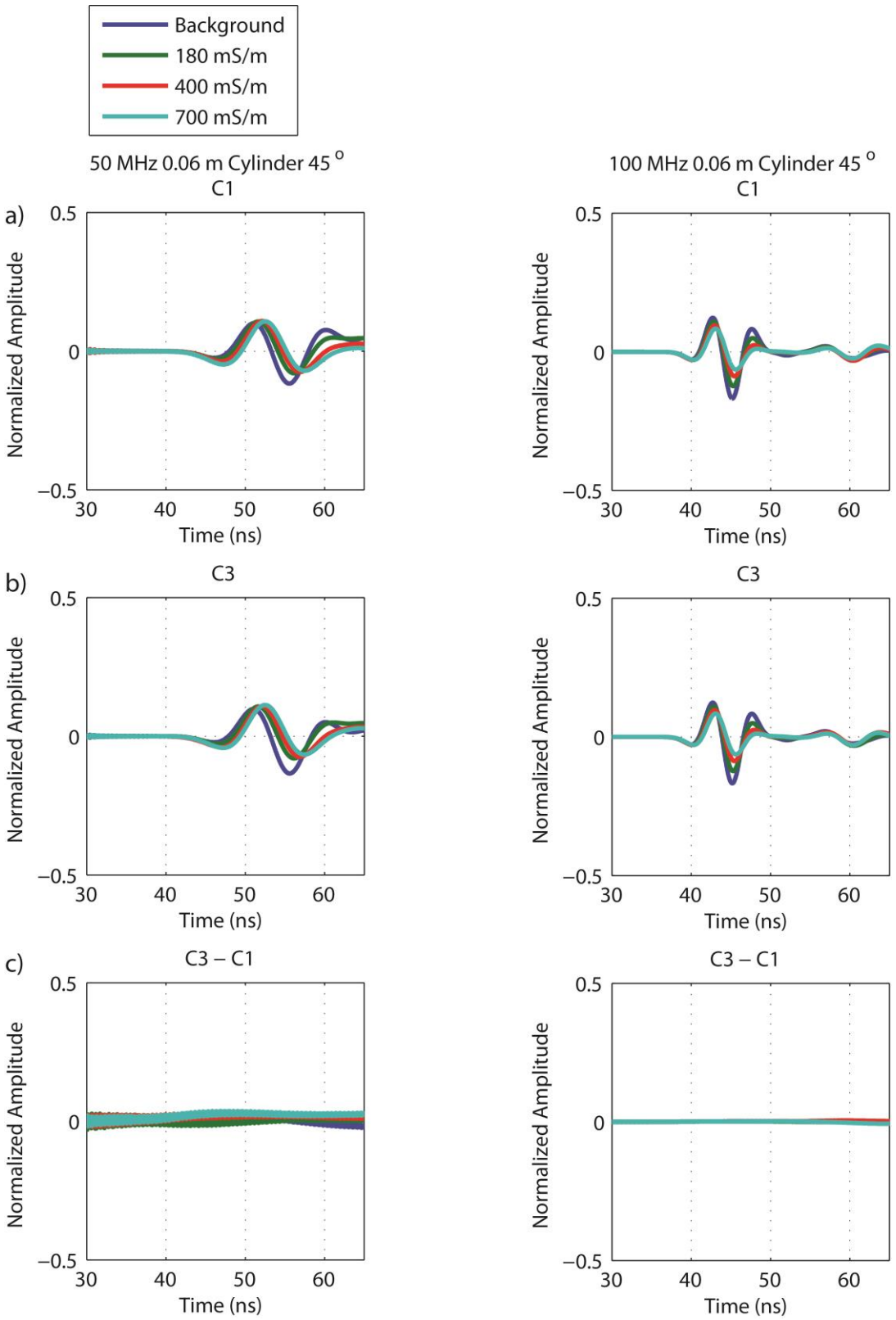

Figure 3.15: Cross-polarized cylinder models oriented 45° to source and receiver. (Left) 50 MHz (Right) 100 MHz. a) C1, b) C3, c) C3-C1.

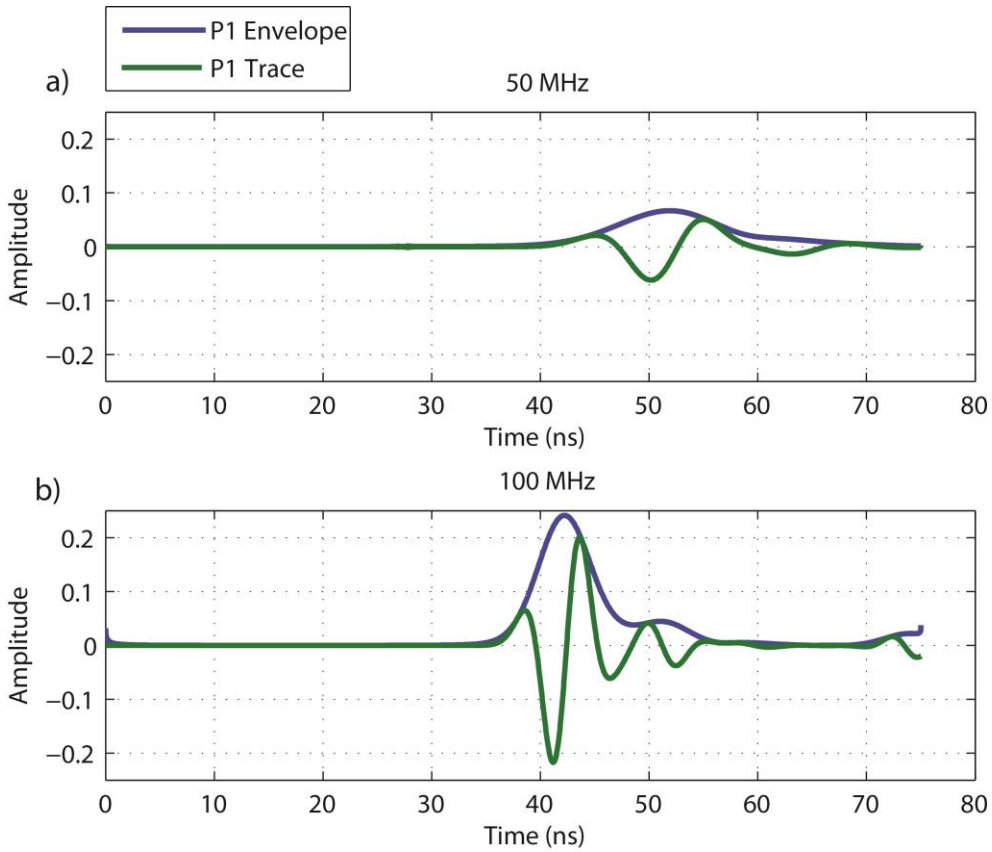

Figure 3.16: P1 trace and P1 amplitude envelope from background 0^{o} cylinder model. (a) 50 MHz, b) 100 MHz.

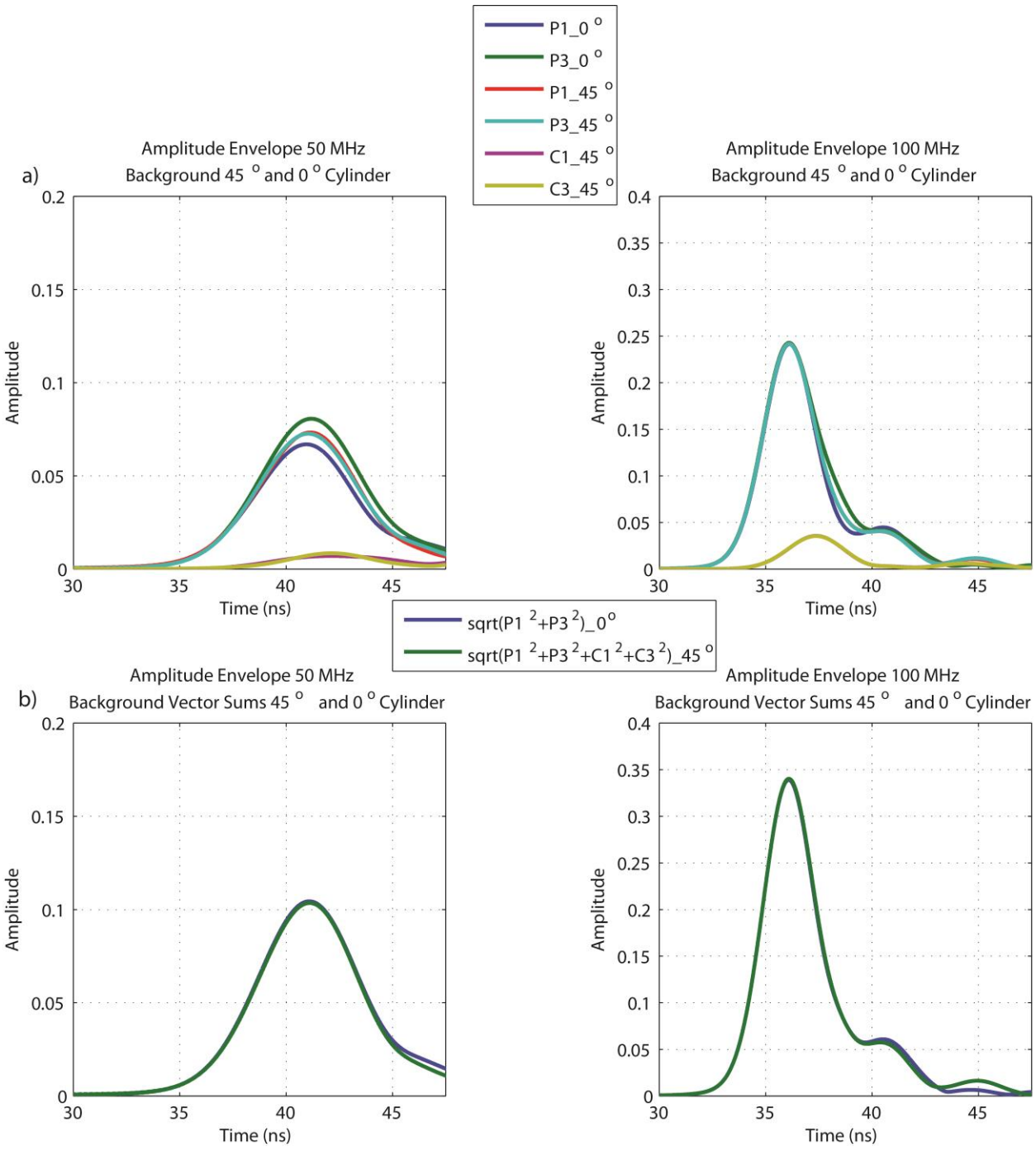

Figure 3.17: Amplitude envelopes for co-polarized and cross-polarized signals from 0^{o} and 45^{o} cylinder models of background electrical conductivity. (Left) 50 MHz (Right) 100 MHz. a) Amplitude envelopes of individual polarizations, b) Vector sums of all polarizations.

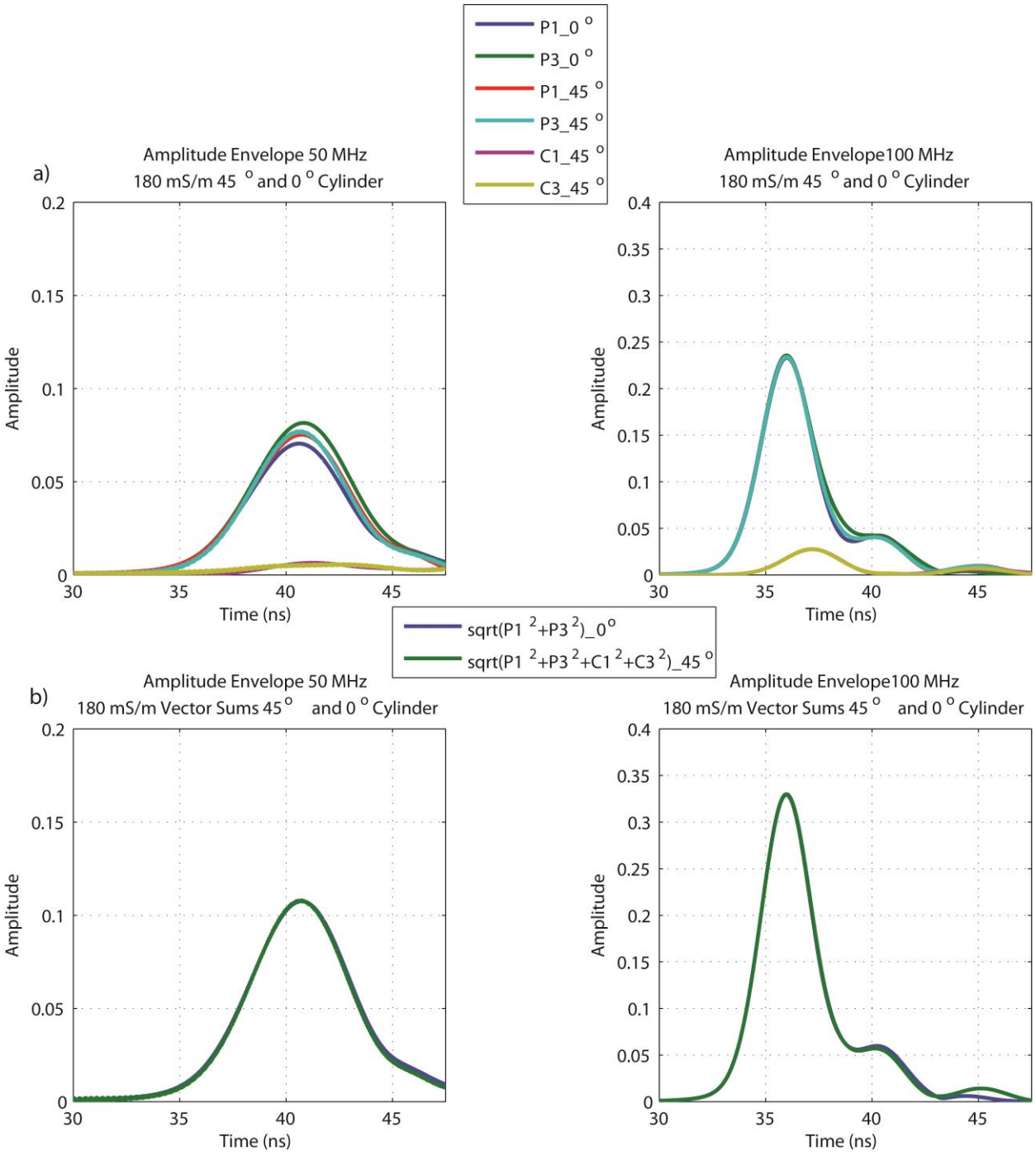

Figure 3.18: Amplitude envelopes for co-polarized and cross-polarized signals from 0° and 45° cylinder models of 180 mS/m. (Left) 50 MHz (Right) 100 MHz. a) Amplitude envelopes of individual polarizations, b) Vector sums of all polarizations.

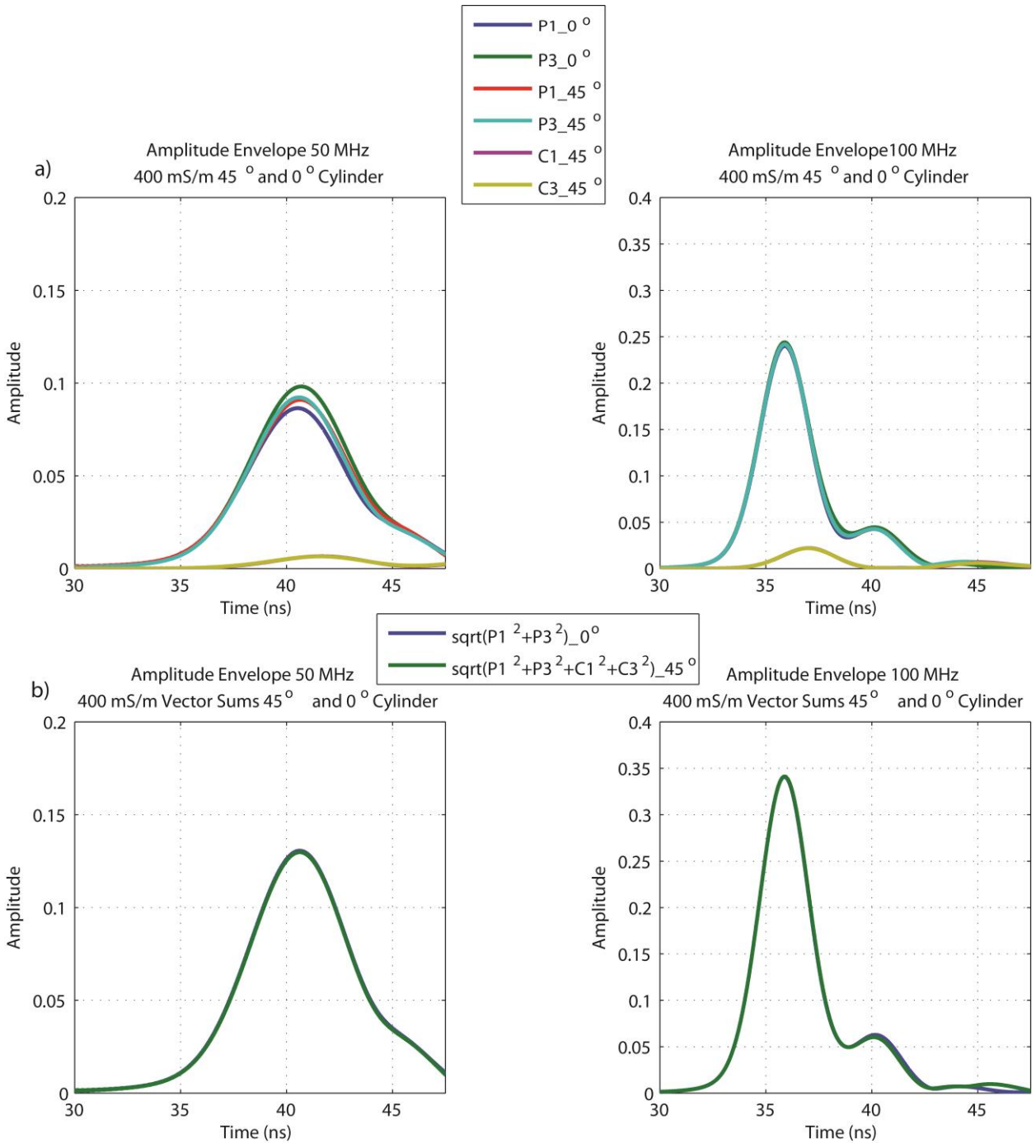

Figure 3.19: Amplitude envelopes for co-polarized and cross-polarized signals from 0° and 45° cylinder models 400 mS/m. (Left) 50 MHz (Right) 100 MHz. a) Amplitude envelopes of individual polarizations, b) Vector sums all polarizations

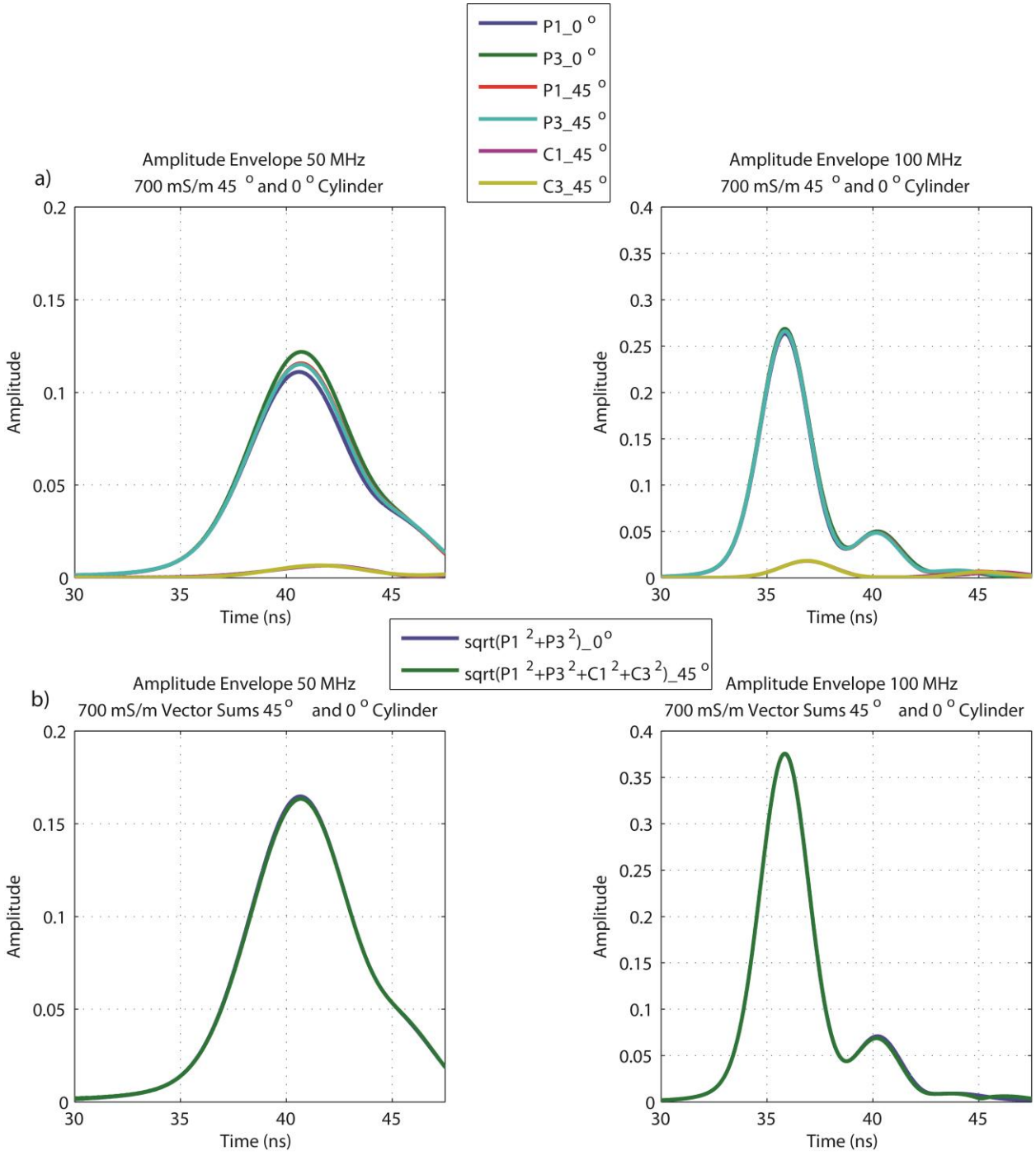

Figure 3.20: Amplitude envelopes for co-polarized and cross-polarized signals from 0^{o} and 45^{o} cylinder models of 700 mS/m. (Left) 50 MHz (Right) 100 MHz. a) Amplitude envelopes of individual polarizations, b) Vector sums of all polarizations.

3.2.5 Survey Line

Two-dimensional modeled radar cross sections are shown in figures 3.21-3.33. They are migrated and un-migrated 50 and 100 MHz sections over a fracture containing a channel in the form of a cylinder oriented 0^o and 45^o (Figure 3.5). To remove the effect of the horizontal fracture and evaluate imaging of the channel (i.e cylinder) a model containing only the horizontal fracture is subtracted (Figure 3.21). The un-migrated and migrated horizontal fracture co-polarized sections for both frequencies are identical because migration does not affect imaging of horizontal, planar targets. The co-polarized (P1 and P3) survey results are displayed in Figures 3.22- 3.25. The co-polarized signals of the horizontal fracture with a cylinder for both frequencies are all similar (Figures 3.22ab-3.25ab). The simulated profiles are dominated by the horizontal fracture reflection at approximately 40 ns. The P3 un-migrated section over the 0^o cylinder shows evidence of a diffraction due to the orientation of the cylinder along the same direction as the P3 source and receiver. After migration the diffraction is collapsed. P1-horizontal fracture and P3 – horizontal fracture modeling results are shown in Figures 3.22cd-3.25cd. The 0^o cylinder results show the P3 response being stronger than P1 response as expected due to cylinder orientation. The 45^o results show P3 and P1 responses having similar amplitudes due to symmetry. Migration appears to work better on the data over the 0^o cylinder models because 2D migration was applied (Figures 3.23cd and Figures 3.25cd). The 45^o cylinder is being intersected at an oblique angle where energy is reflected out of the plane so the 2D migration cannot completely collapse the reflected energy from the oblique cylinder.

The cross-polarized survey results are displayed in Figures 3.26-3.29. The 45^o cylinder is imaged by the cross-polarized data but the 0^o cylinder survey line shows no cross-polarized response. The cross-polarized data are able to detect the cylinder oriented at 45^o because the

GPR signal is depolarized. The 45^0 cylinder cross-polarized models show opposite polarity compared to the co-polarized P1 – horizontal fracture and P3 – horizontal fracture results. Additionally, the 45^o cross-polarized images show the same result with and without horizontal fracture subtraction (Figures 3.26-3.29 Left). This is because the cross-polarized signals receive no reflected energy from the horizontal fracture. In addition, the cross-polarized un-migrated data (Figure 3.26 and Figure 3.28) show small amplitudes near source and receiver and larger amplitudes farther away, whereas migrated cross-polarized signals (Figure 3.27 and Figure 3.29) show large amplitudes near source and receiver and weaker amplitudes farther away.

The summed results (P1+P3), (P1+P3) – horizontal fracture, and (C1+C3) are shown in Figures 3.30-33. The (P1+P3) un-migrated line over the 0^o cylinder shows evidence of a diffraction due to the cylinder orientation (Figure 3.30a and Figure 3.32a) but the migrated (P1+P3) lines for both 0^o and 45^o cylinders are similar in amplitude (Figure 3.31a and Figure 3.33a). The co-polarized sums from the different oriented cylinders suggest that as long as the polarizations are orthogonal to one another an accurate image of the target is acquired. After subtraction and migration the diffractions are collapsed better in the 0^o cylinder data than in the 45^o cylinder data (Figures 3.31b and Figure 3.33b). In the cross-polarized sums (C1+C3) only the 45^o cylinder data shows a detectable amplitude response because the 0^o cylinder does not cause the signal to depolarize (Figures 3.30c-3.33c). These observations are in agreement with the earlier section of single trace cylinder models.

Figures 3.34-3.37 compare the co-polarized and cross-polarized data from the 45^o cylinder models. Subtracting the horizontal fracture causes the co-polarized sections to show similar responses to the cross-polarized sections (Figure 3.34abcd-3.37abcd). The cross-polarized response is weaker in amplitude and opposite in polarity to the co-polarized responses.

The summed data sets (C1+C3) are weaker in amplitude and display opposite polarity compared to the sum of (P1+P3) after subtraction of the horizontal fracture (Figures 3.34ef-3.37ef). The cross-polarized signals do not image the horizontal fracture, but image the cylinder when oriented oblique to the survey line. This indicates that an interval selected in the co-polarized data could be used to track amplitude changes in the cross-polarized data.

3.2.6 Survey Line Result Summary

1. Co-polarized signals are dominated by the flat horizontal fracture and the channel (cylinder) is difficult to identify.
2. Cross-polarized signals only see the oblique channel and not energy reflected from the horizontal fracture.
3. The co-polarized signals after subtracting the horizontal fracture look similar to cross-polarized the signals.

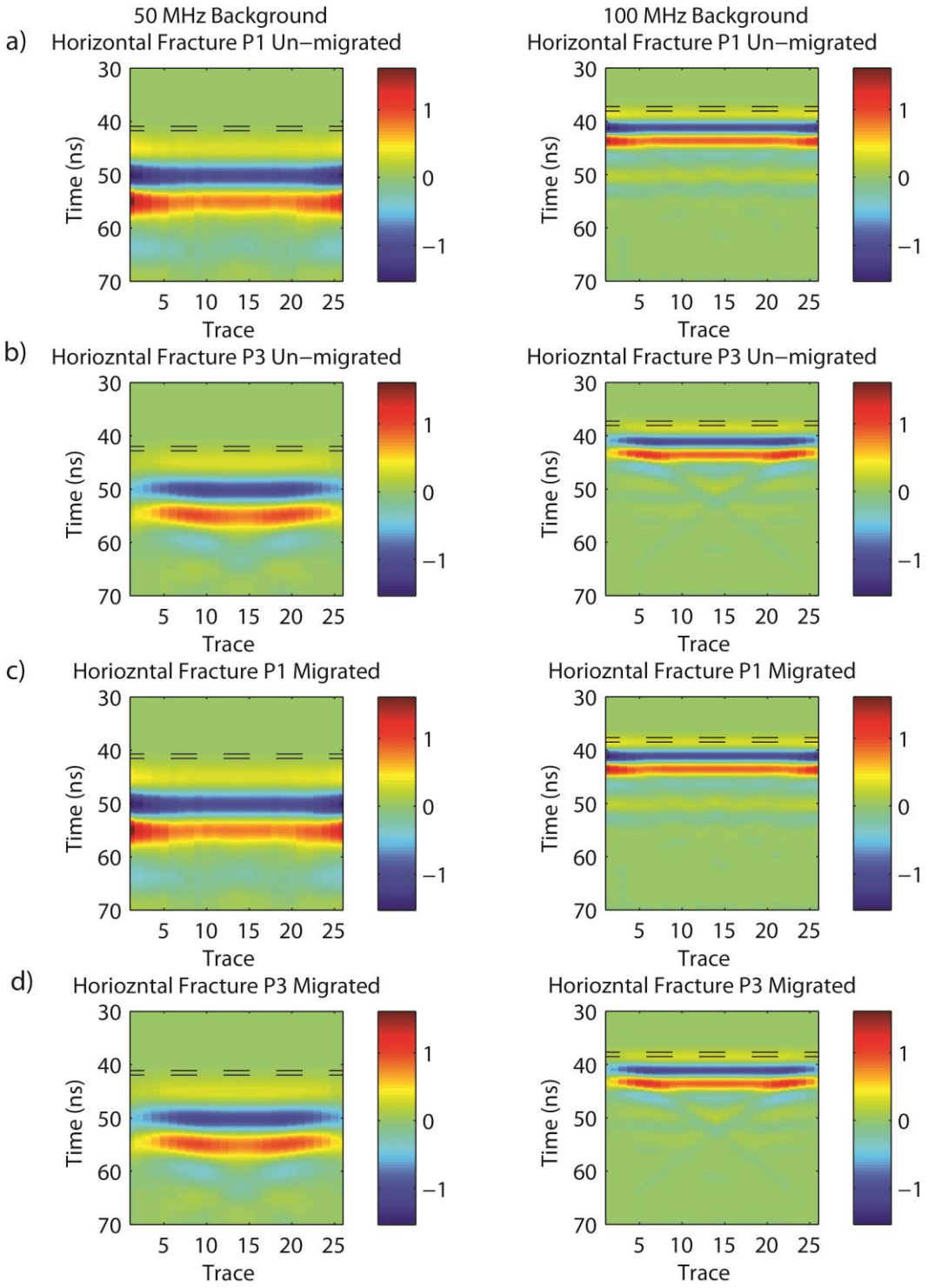

Figure 3.21: Un-migrated and migrated 50 and 100 MHz horizontal fracture modles. The fracture location is shown by a dashed line. (Left) 50 MHz (Right) 100 MHz. Water electrical conductivity of 28 mS/m. a) P1 horizontal fracture un-migrated, b) P3 horizontal fracture un-migrated, c) P1 horizontal fracture migrated d) P3 horizontal fracture migrated.

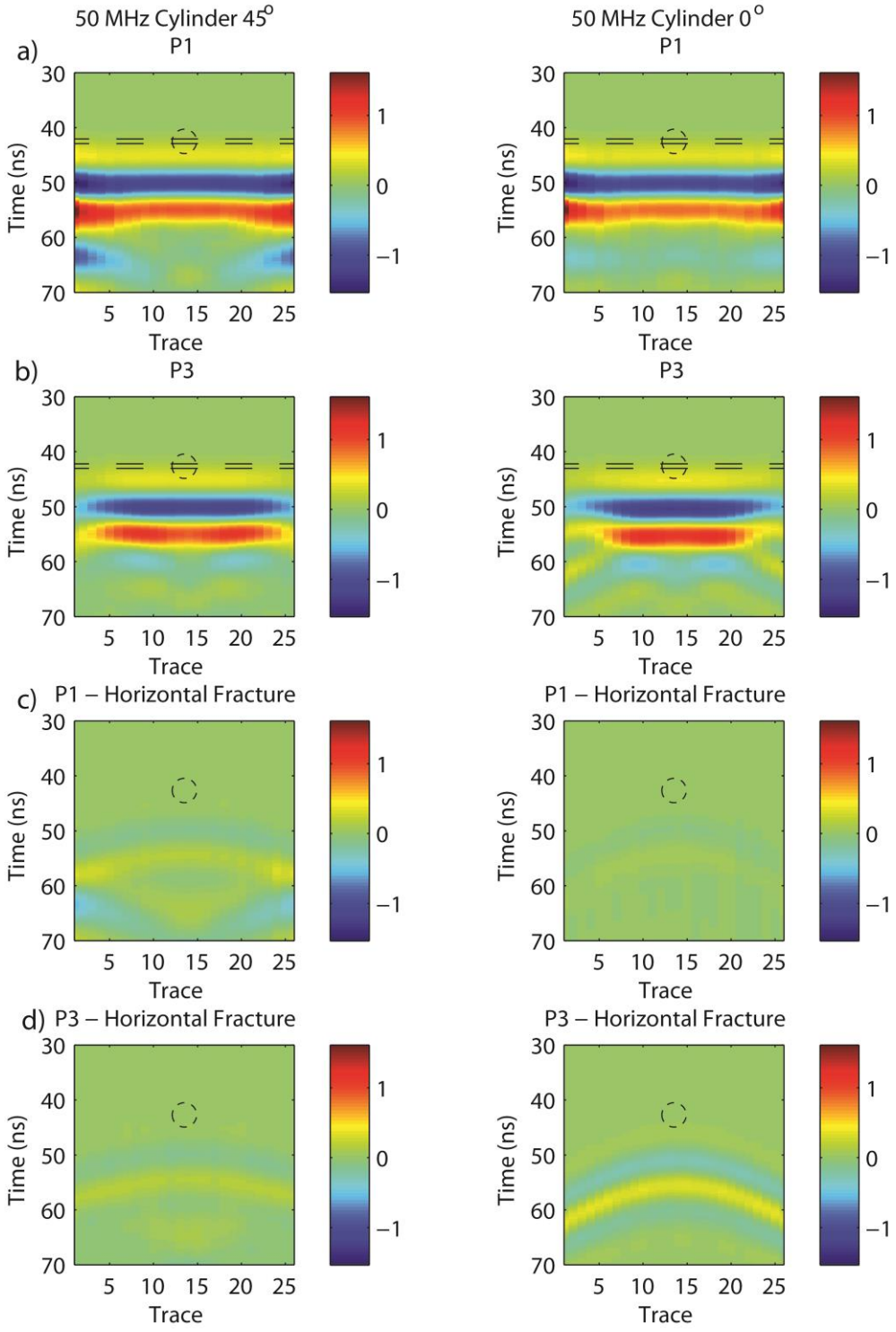

Figure 3.22: Un-migrated 50 MHz survey line over cylinder. (Left) 45^0 cylinder and (Right) 0^0 cylinder. Water electrical conductivity of 28 mS/m. a) P1 horizontal fracture with cylinder, b) P3 horizontal fracture with cylinder, c) P1 – horizontal fracture, d) P3 – horizontal fracture.

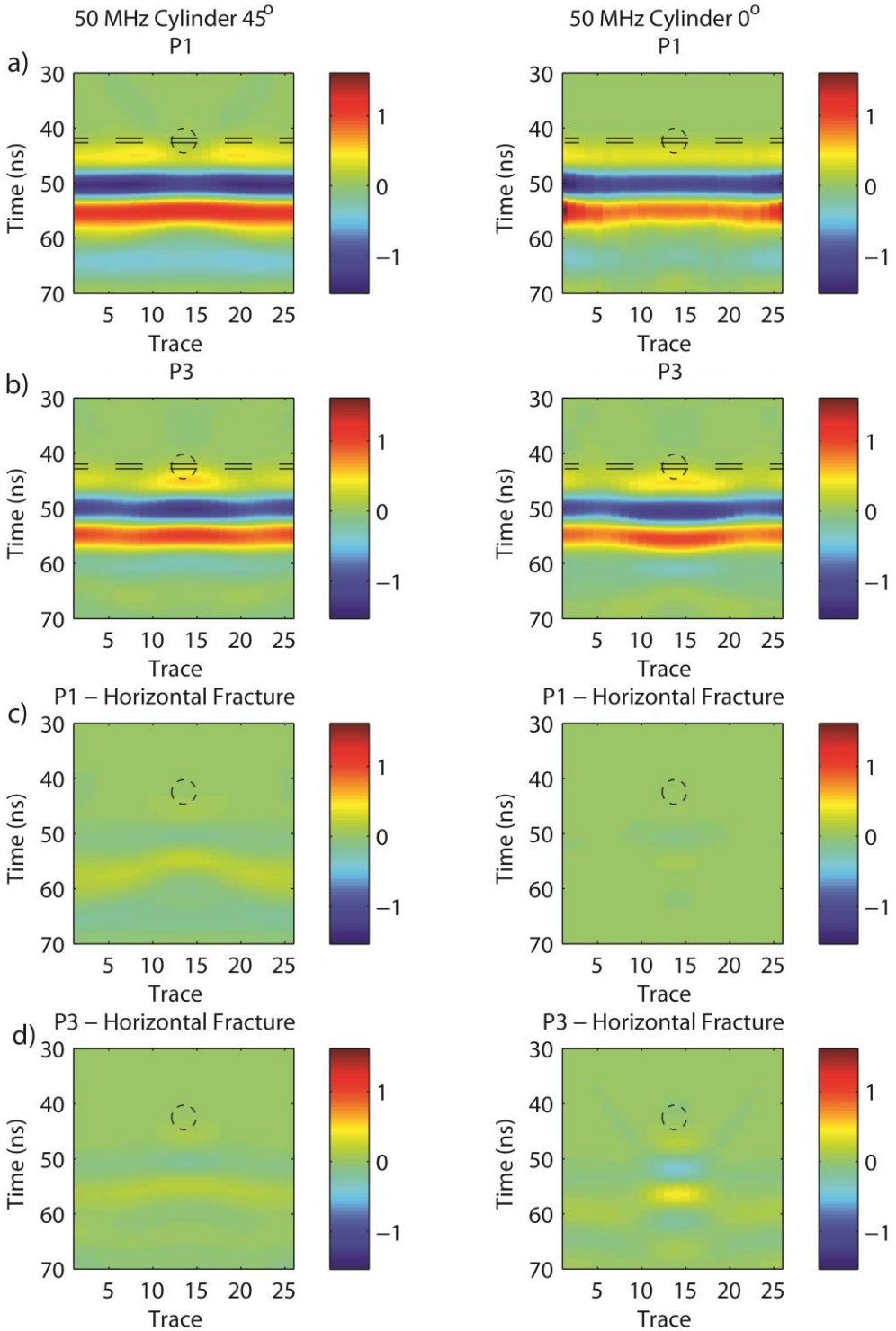

Figure 3.23: Migrated 50 MHz survey line over cylinder. (Left) 45^0 cylinder and (Right) 0^0 cylinder. Water electrical conductivity of 28 mS/m. a) P1 horizontal fracture with cylinder, b) P3 horizontal fracture with cylinder, c) P1 – horizontal fracture, d) P3 – horizontal fracture.

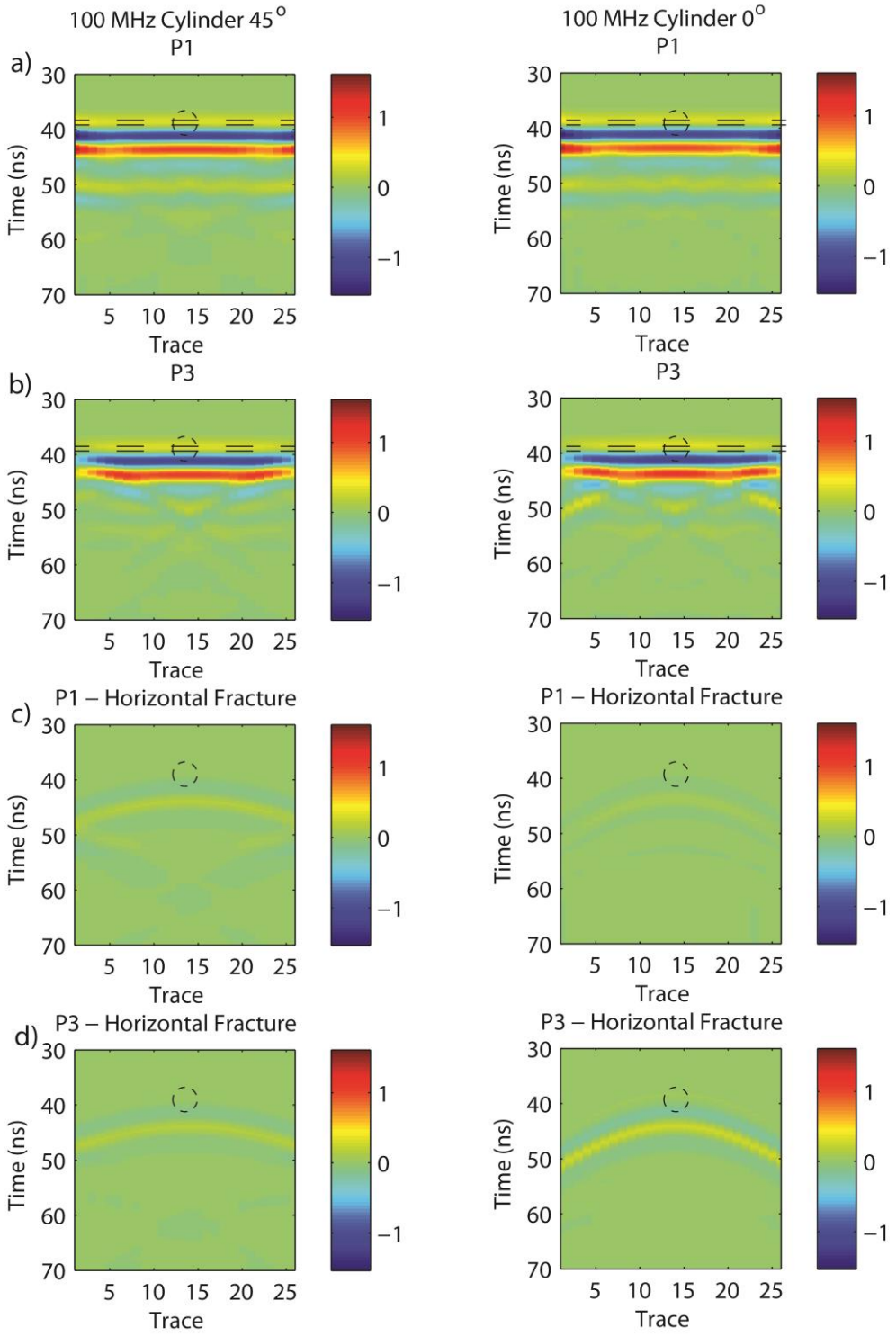

Figure 3.24: Un-migrated 100 MHz survey line over cylinder. (Left) 45^0 cylinder and (Right) 0^0 cylinder. Water electrical conductivity of 28 mS/m. a) P1 horizontal fracture with cylinder, b) P3 horizontal fracture with cylinder, c) P1 – horizontal fracture, d) P3 – horizontal fracture.

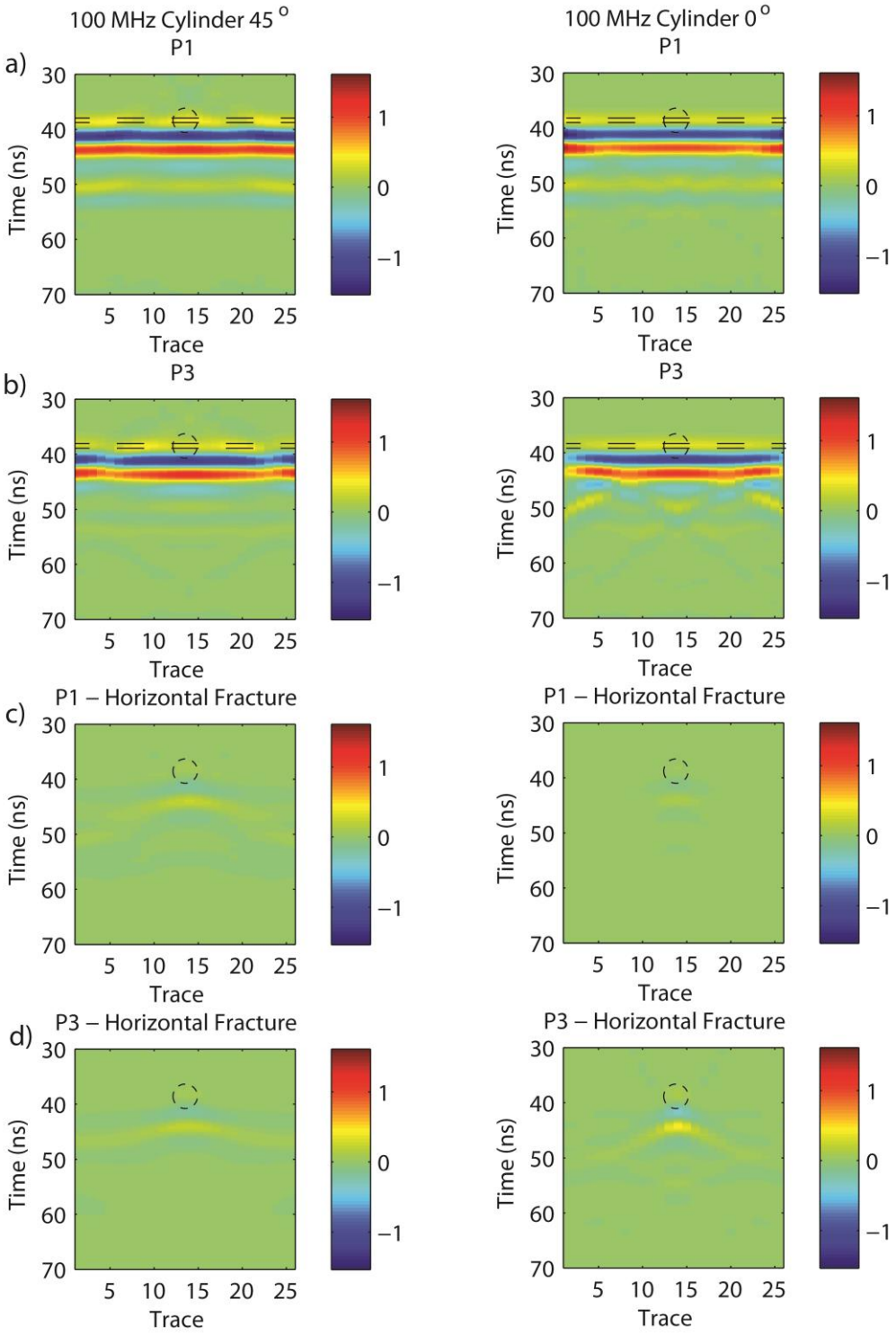

Figure 3.25: Migrated 100 MHz survey line over cylinder. (Left) 45^0 cylinder and (Right) 0^0 cylinder. Water electrical conductivity of 28 mS/m. a) P1 horizontal fracture with cylinder, b) P3 horizontal fracture with cylinder, c) P1 – horizontal fracture, d) P3 – horizontal fracture.

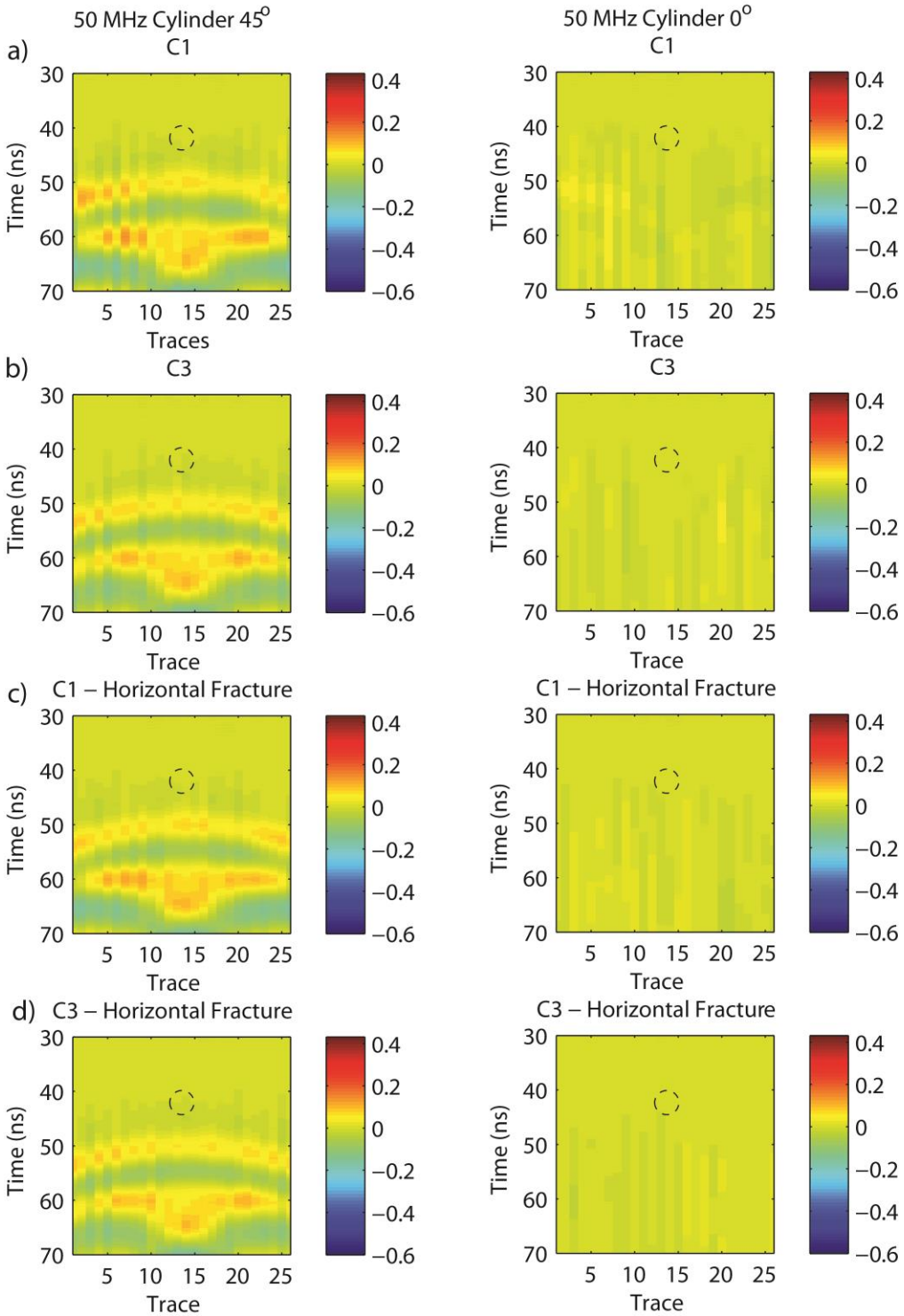

Figure 3.26: Un-migrated 50 MHz survey line over cylinder. (Left) 45^0 cylinder and (Right) 0^0 cylinder. Water electrical conductivity of 28 mS/m. a) C1 horizontal fracture with cylinder, b) C3 horizontal fracture with cylinder, c) C1 – horizontal fracture, d) C3 – horizontal fracture.

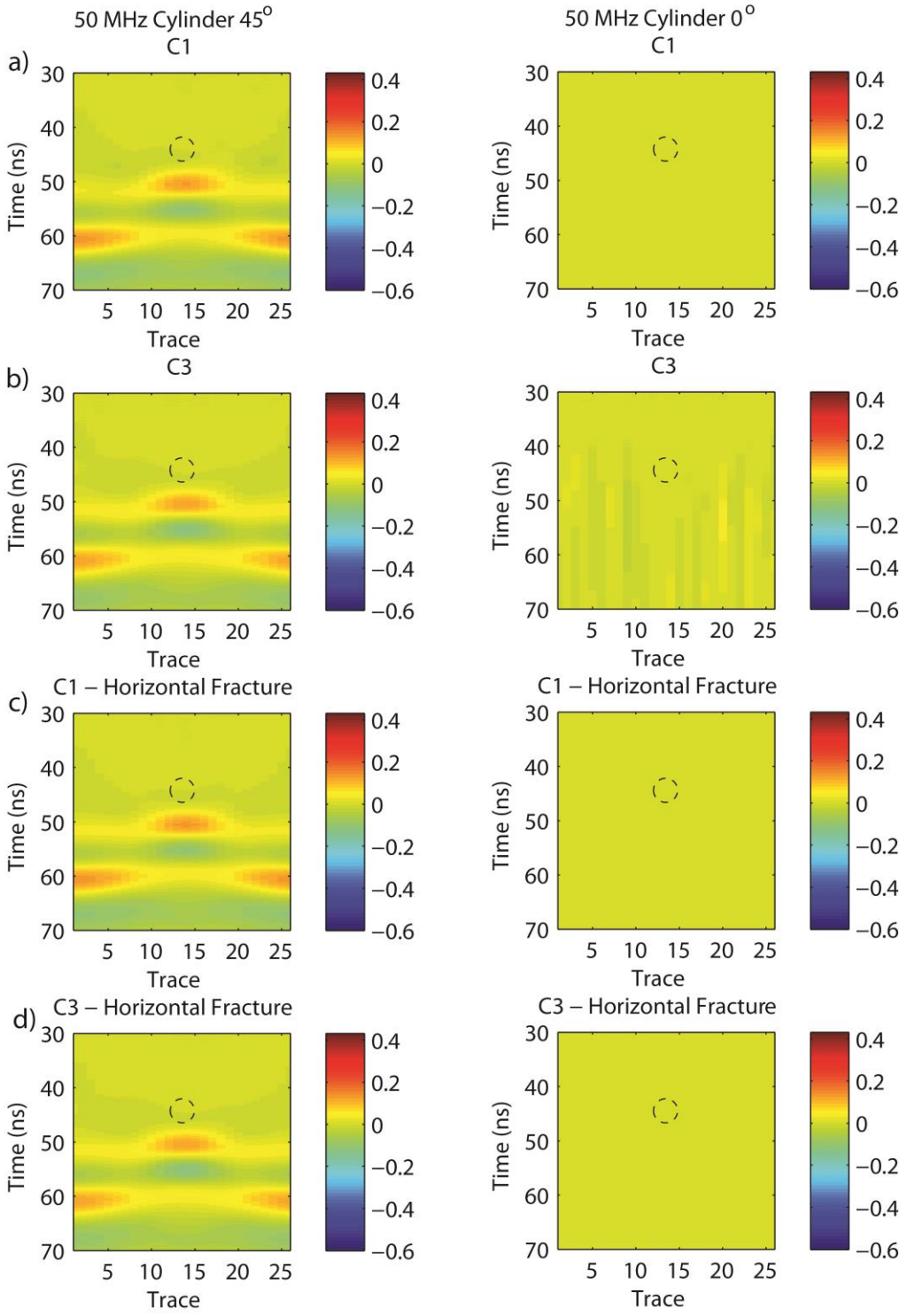

Figure 3.27: Migrated 50 MHz survey line over cylinder. (Left) 45^0 cylinder and (Right) 0^0 cylinder. Water electrical conductivity of 28 mS/m. a) C1 horizontal fracture with cylinder b) C3 horizontal fracture with cylinder c) C1 – horizontal fracture d) C3 – horizontal fracture.

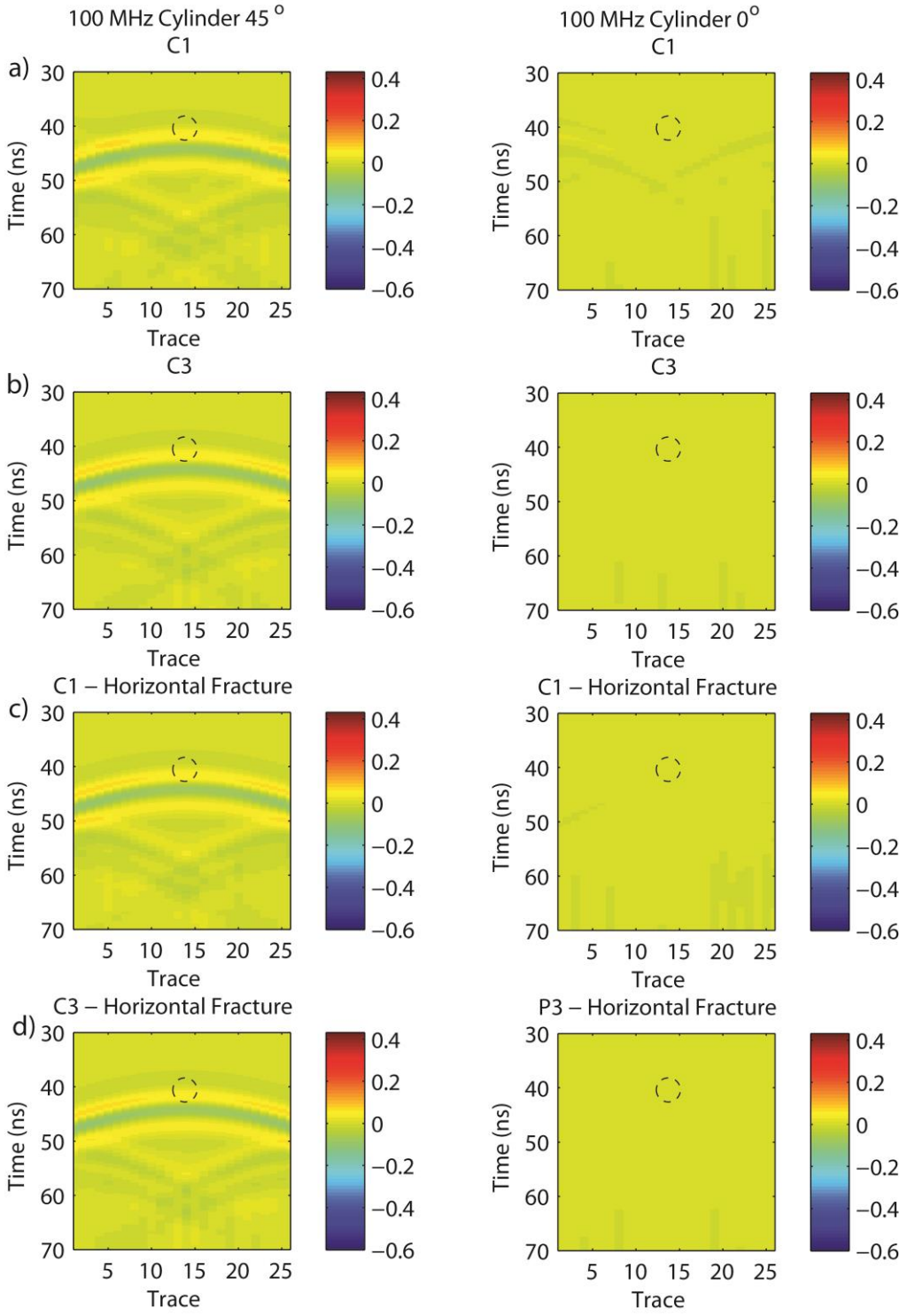

Figure 3.28: Un-migrated 100 MHz survey line over cylinder. (Left) 45^0 cylinder and (Right) 0^0 cylinder. Water electrical conductivity of 28 mS/m. a) C1 horizontal fracture with cylinder, b) C3 horizontal fracture with cylinder, c) C1 – horizontal fracture, d) C3 – horizontal fracture.

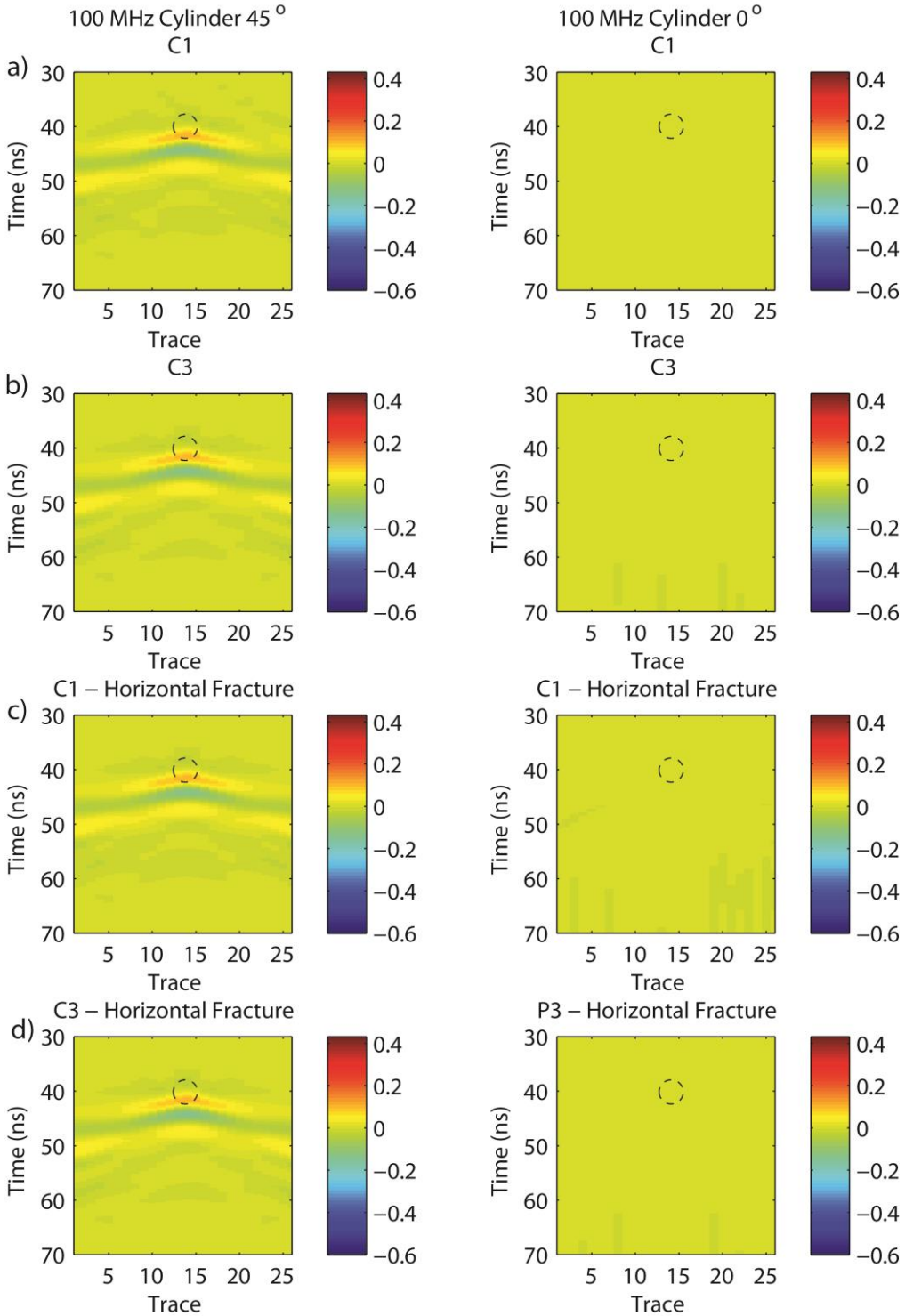

Figure 3.29: Migrated 100 MHz survey line over cylinder. (Left) 45^0 cylinder and (Right) 0^0 cylinder. Water electrical conductivity of 28 mS/m. a) C1 horizontal fracture with cylinder, b) C3 horizontal fracture with cylinder, c) C1 – horizontal fracture, d) C3 – horizontal fracture.

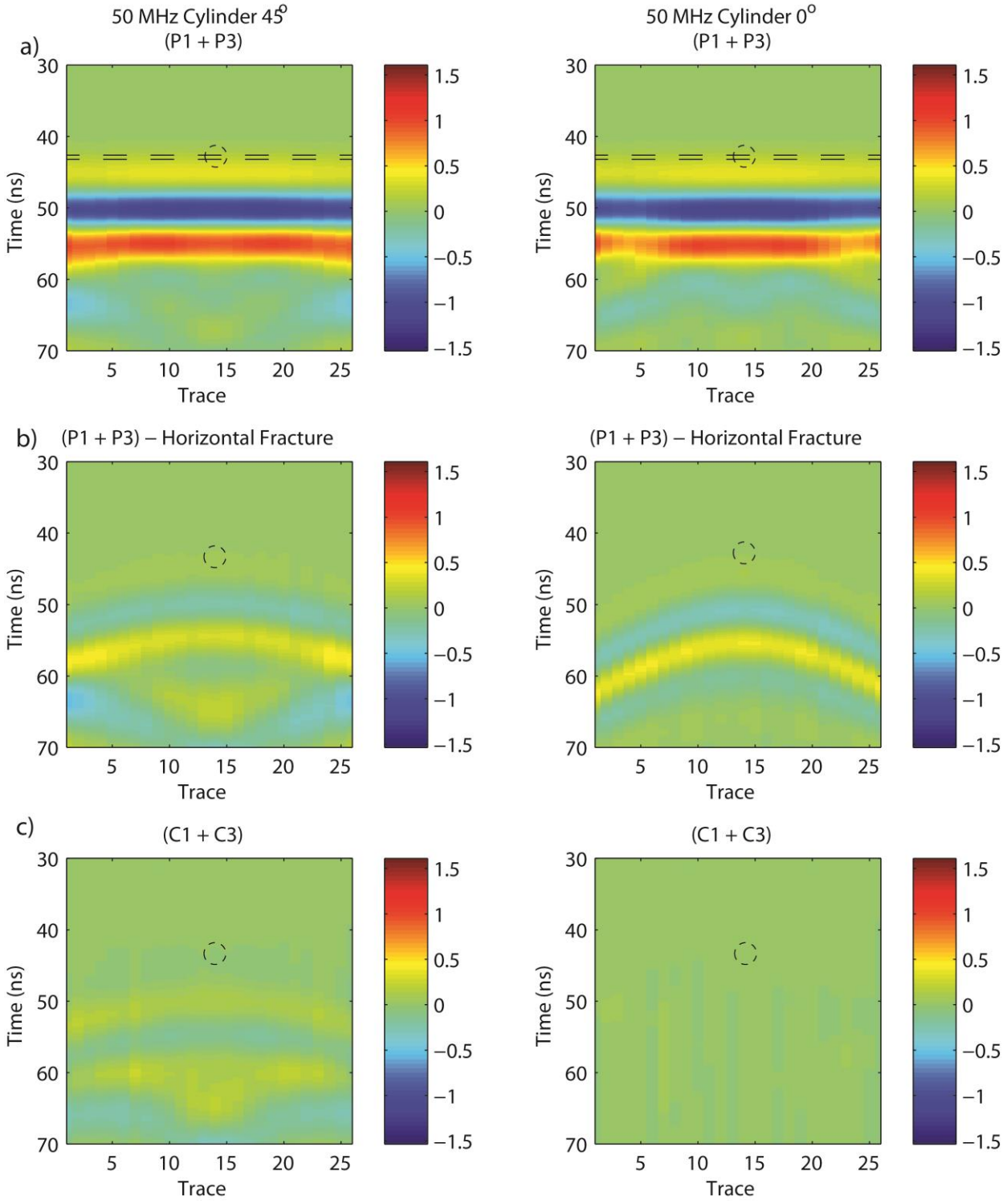

Figure 3.30: Un-migrated 50 MHz survey line over cylinder. (Left) 45^0 cylinder and (Right) 0^0 cylinder. Water electrical conductivity of 28 mS/m. a) (P1+P3) horizontal fracture with cylinder, b) (P1+P3) - horizontal fracture, c) (C1+C3).

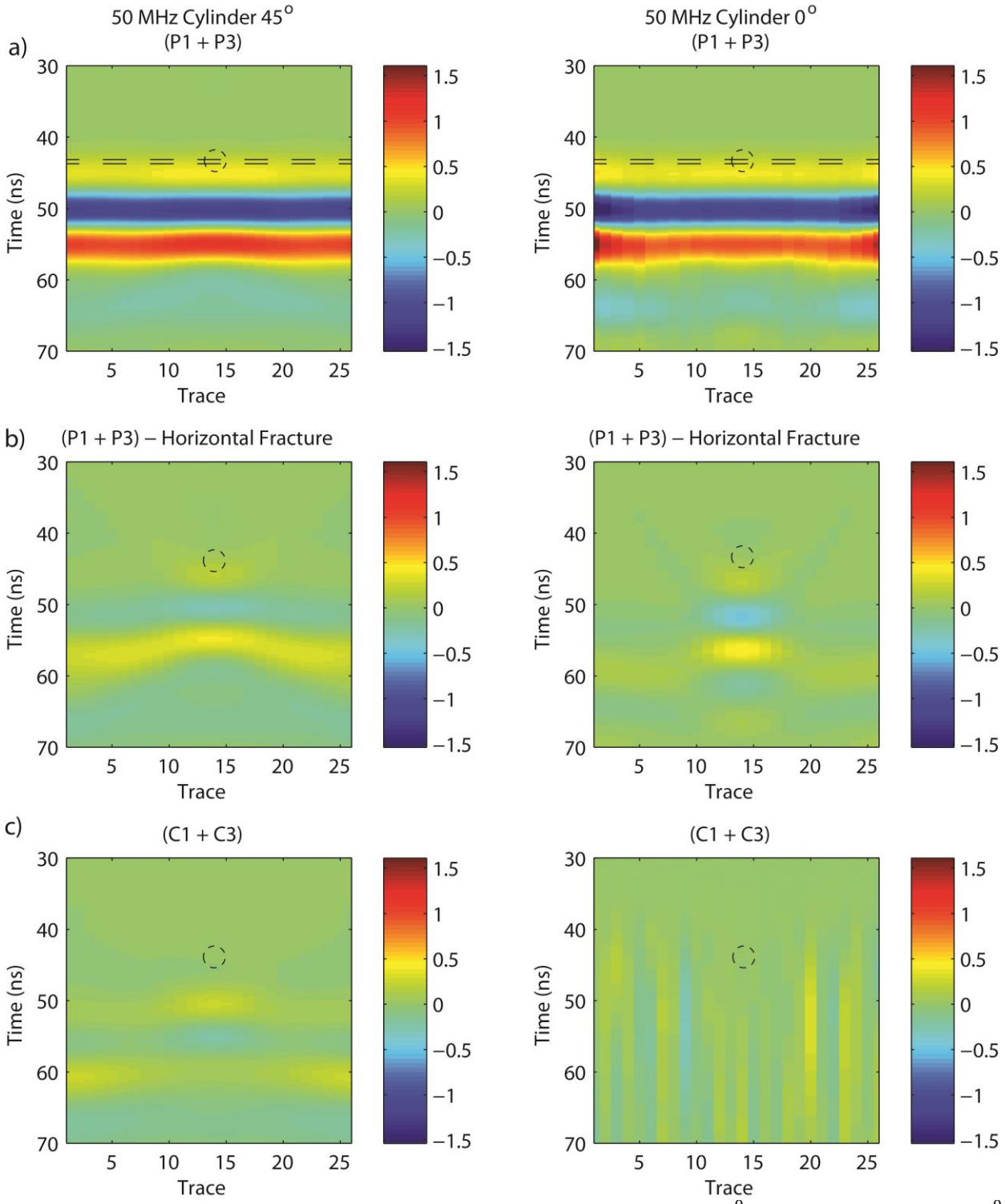

Figure 3.31: Migrated 50 MHz survey line over cylinder. (Left) 45^0 cylinder and (Right) 0^0 cylinder. Water electrical conductivity of 28 mS/m. a) (P1+P3) horizontal fracture with cylinder, b) (P1+P3) - horizontal fracture, c) (C1+C3).

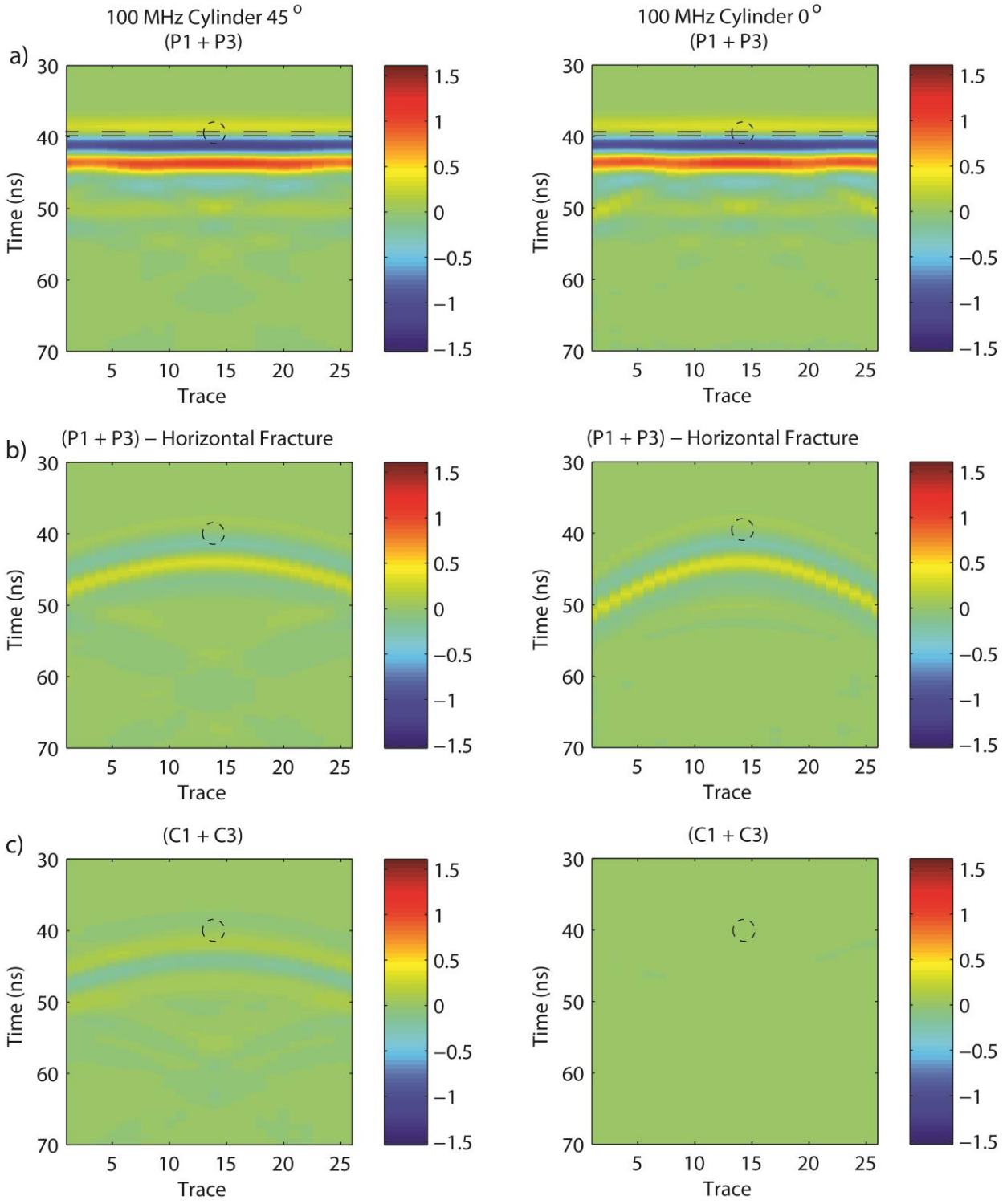

Figure 3.32: Un-migrated 100 MHz survey line over cylinder. (Left) 45^0 cylinder and (Right) 0^0 cylinder. Water electrical conductivity of 28 mS/m. a) (P1+P3) horizontal fracture with cylinder, b) (P1+P3) - horizontal fracture, c) (C1+C3).

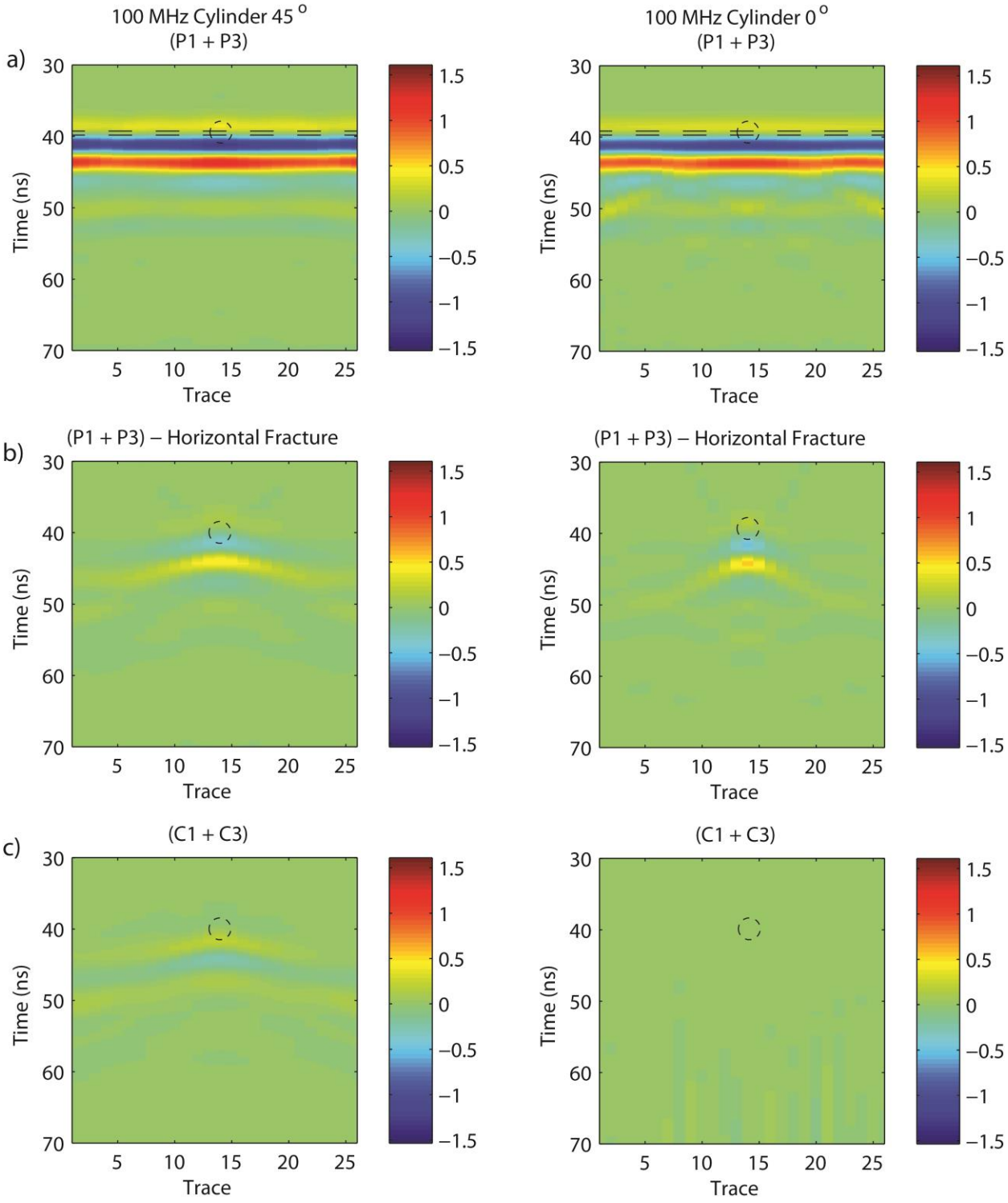

Figure 3.33: Migrated 100 MHz survey line over cylinder. (Left) 45^0 cylinder and (Right) 0^0 cylinder. Water electrical conductivity of 28 mS/m. a) (P1+P3) horizontal fracture with cylinder, b) (P1+P3) - horizontal fracture, c) (C1+C3).

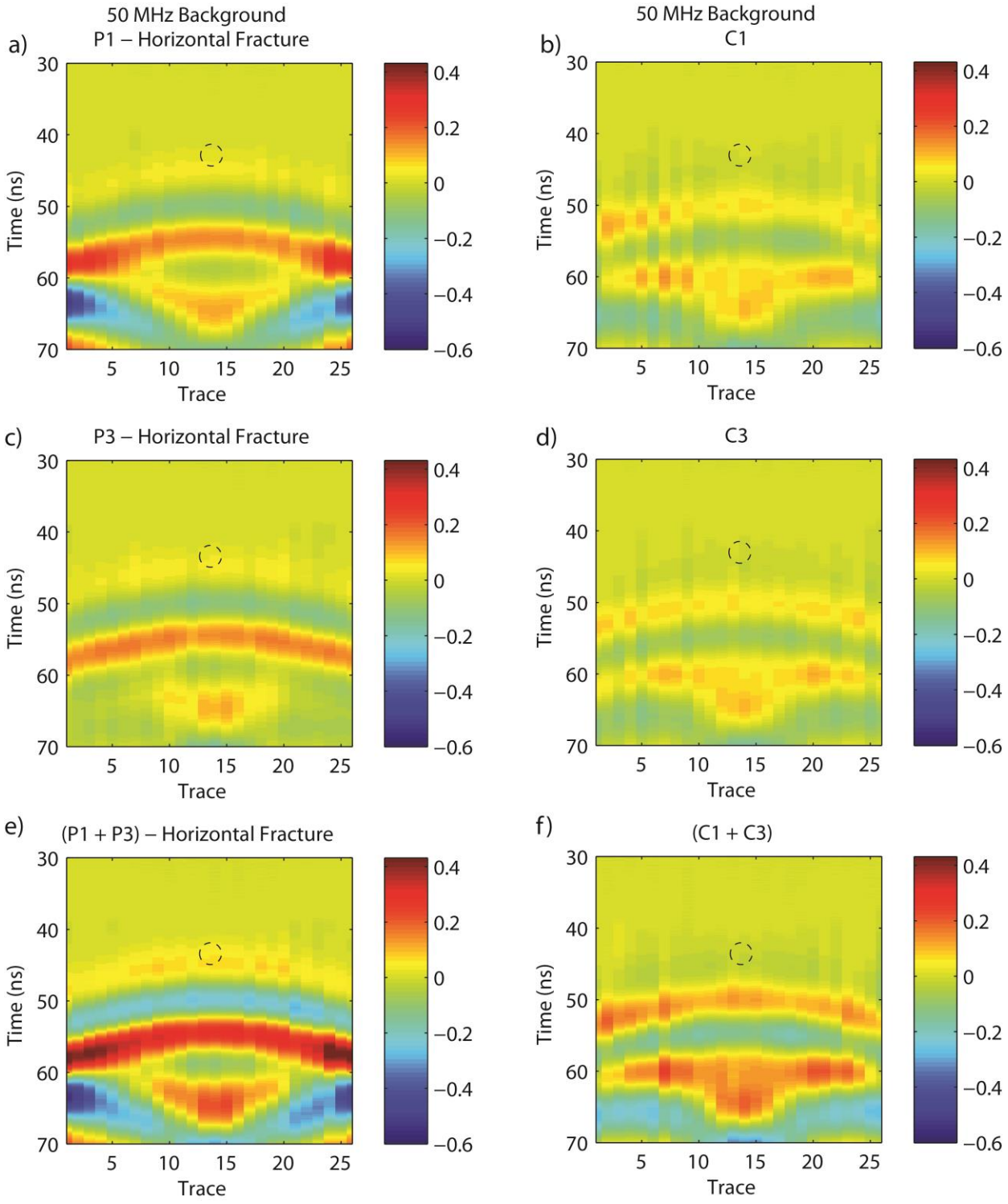

Figure 3.34: Un-migrated 50 survey line over cylinder oriented 45^{o} to antennas. Water electrical conductivity of 28 mS/m. a) P1 – horizontal fracture, b) C1, c) P3- horizontal fracture, d) C3, e) (P1+P3) – horizontal, f) (C1+C3).

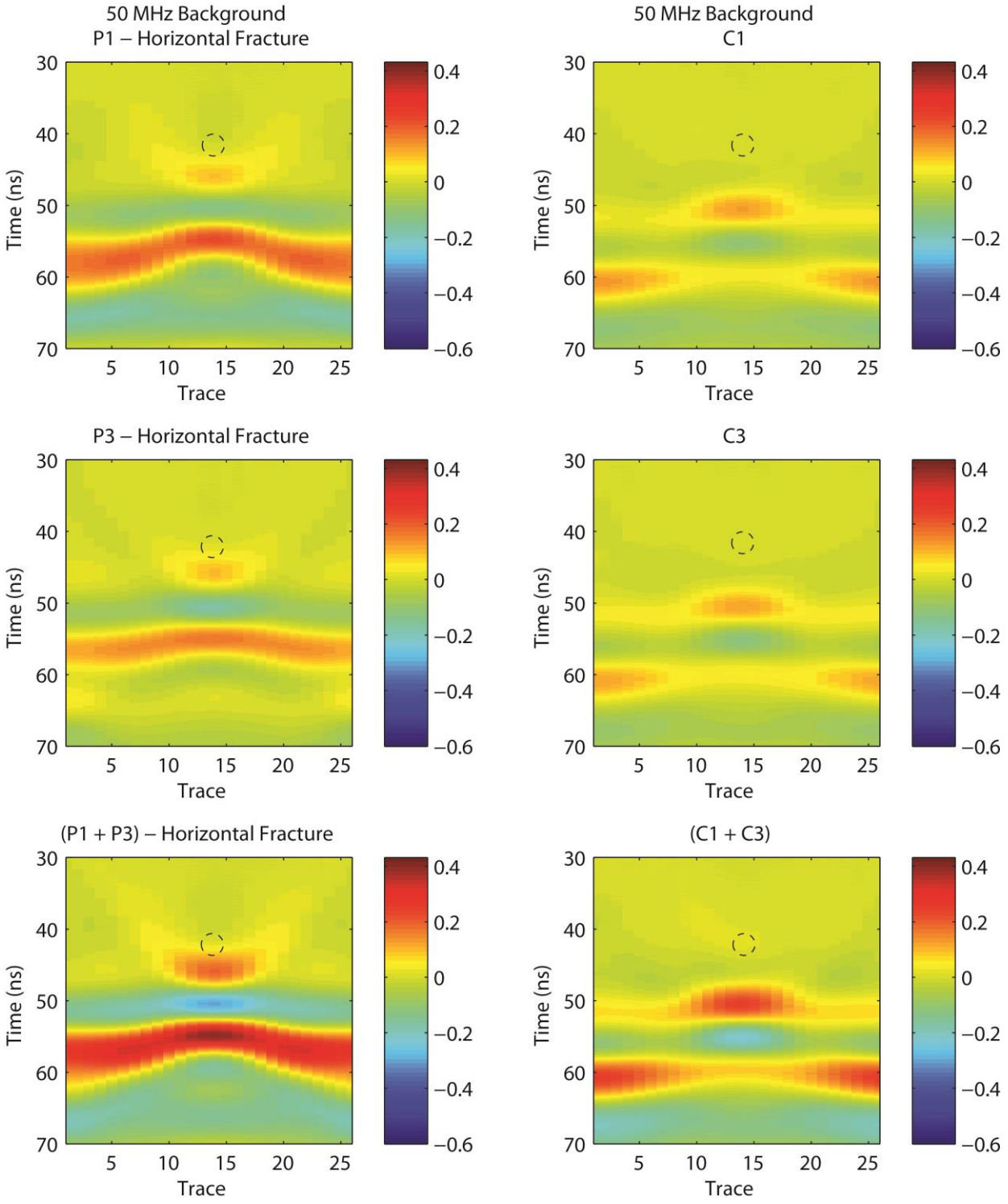

Figure 3.35: Migrated 50 MHz survey line over cylinder oriented 45^{o} to antennas. Water electrical conductivity of 28 mS/m. a) P1 – horizontal fracture, b) C1, c) P3- horizontal fracture, d) C3, e) (P1+P3) – horizontal, f) (C1+C3).

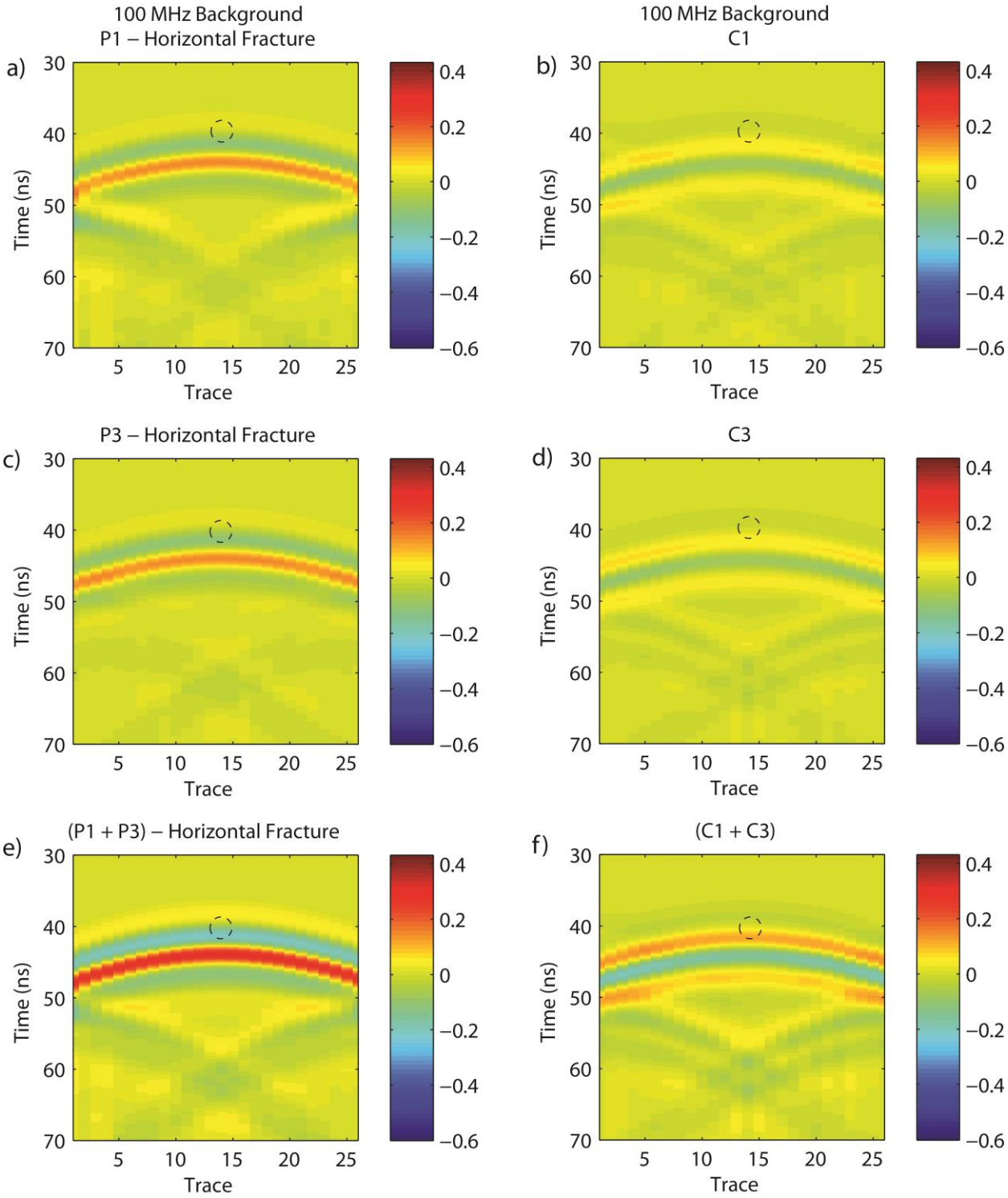

Figure 3.36: Un-migrated 100 MHz survey line over cylinder oriented 45^{o} to antennas. Water electrical conductivity of 28 mS/m. a) P1 – horizontal fracture, b) C1, c) P3- horizontal fracture, d) C3, e) (P1+P3)– horizontal fracture, f) (C1+C3).

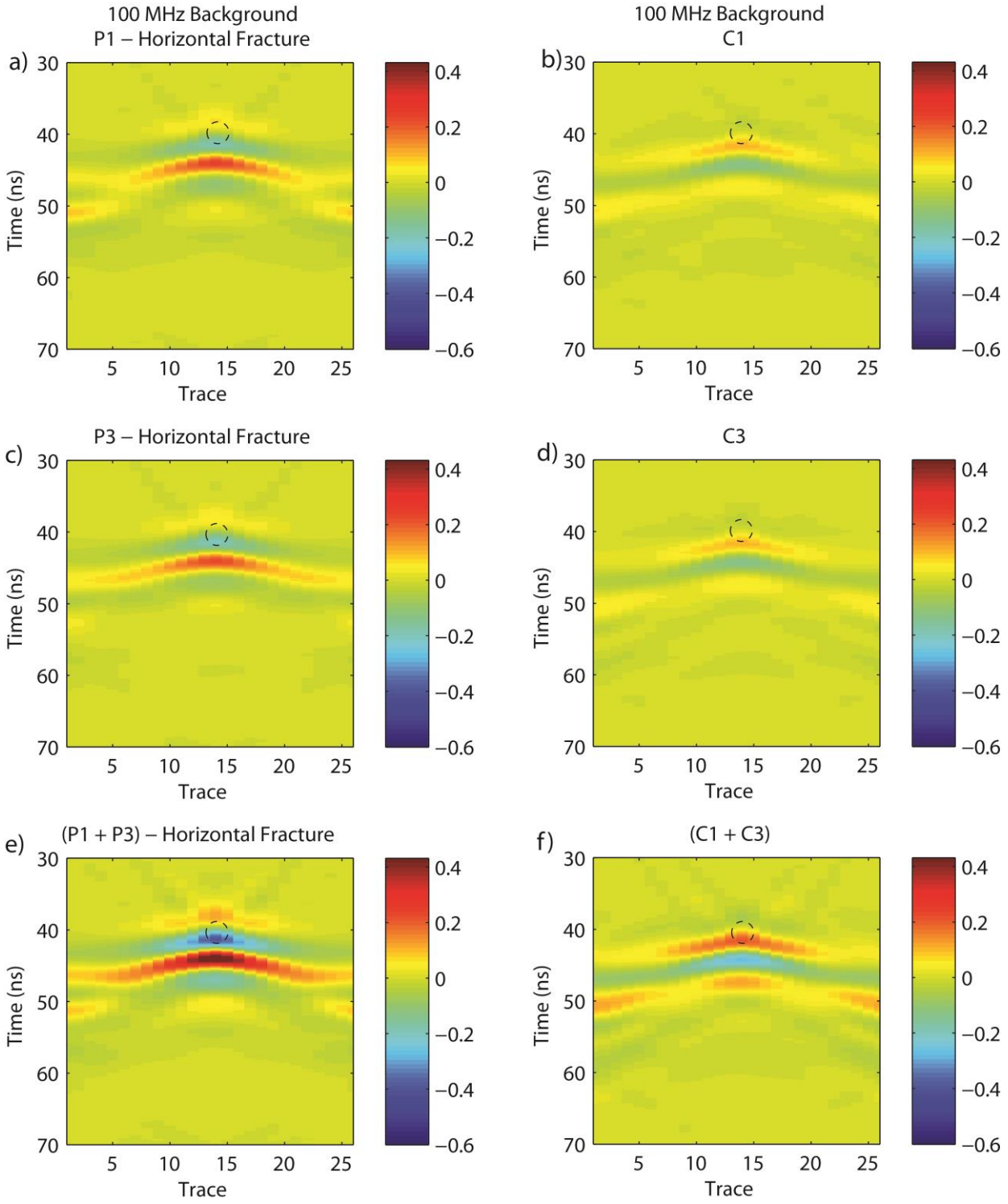

Figure 3.37: Migrated 100 MHz survey line over cylinder oriented 45^{o} to antennas. Water electrical conductivity of 28 mS/. a) P1 – horizontal fracture, b) C1, c) P3- horizontal fracture, d) C3, e) (P1+P3) – horizontal, f) (C1+C3).

3.3 FDTD Numerical Modeling Discussion

The objective of the numerical modeling was to simulate GPR acquisition parameters (Figure 3.1) used at the Altona Flat Rock Site, analyze fracture response from changing fracture aperture, water electrical conductivity, and the presence of a channel along the fracture plane.

The horizontal fracture models demonstrated the expected effects of fracture aperture and water electrical conductivity on signal reflection amplitude and phase. Increasing the fracture aperture increased reflection amplitude in both 50 and 100 MHz. Increasing the electrical conductivity of the fracture increased the amplitude in both the 50 and 100 MHz, with the 50 MHz showing greater change in amplitude. Increasing the electrical conductivity also causes a phase delay that is more pronounced in the 50 MHz data than the 100 MHz data. These observations are in agreement with EM theory (Balanis, 1989) and published works by Tsoflias and Becker (2008), Sambuelli and Calzoni (2010), and Kana et al., (2013).

The simulated channel model results showed that the orientation and dimensions of the channel causes differences in radar response between varying polarizations. The rectangular channel showed small differences between the co-polarized components (Figure 3.11). The cylindrical channel showed significant changes between co-polarized and cross-polarized signals depending on the orientation of the cylinder. A cylinder orientated at 0^{o} to the y-axis showed no response from cross-polarized components but did show a response in the co-polarized data, where P3 was stronger than P1, as expected (Roberts and Daniels 1996). The P3 response was stronger because the cylinder is parallel with source and receiver and this relationship held for increasing water electrical conductivity (Figure 3.12). The 45^{o} cylinder showed response from all four polarizations, with C1 having the same amplitude as C3, but opposite wavelet polarity from the co-polarized components. Analogous observations from a point scatterer where reported by

(Lehmann et al. 2000) (Figures 3.14-3.15). P1 and P3 showed the same response due to symmetry. Increasing the water electrical conductivity increased the co-polarized response significantly. The cross-polarized data also showed a smaller amplitude increase. Increasing the electrical conductivity in the 0^o cylinder causes co-polarized signal difference to increase (Figure 3.12c). Increasing the electrical conductivity in the 45^o cylinder does not caused the co-polarized or cross-polarized signals difference to increase (Figures 3.14c-3.15c).

The survey line models are similar to field acquisition parameter used at the Altona Flat Rock site. Models comparing 0^o and 45^o oriented cylinders demonstrate that as long as two co-polarized signals are collected orthogonal to one another and summed (P1+P3), the images of the cylinder are similar (Figures 3.30b-3.33b). The similarity between the co-polarized responses suggests that orientation of antennas on the surface is unimportant. As long as polarizations are orthogonal to each other and summed, an accurate image of the subsurface is obtained. This observation was field tested by Tsoflias et al. (2012) when he collected two sets of co-polarized signals oriented 45^0 apart and showed that there was no appreciable difference between the sums.

I compared the co-polarized signals and cross-polarized signals from the 45^o cylinder to identify a means to extract information from cross-polarized signals. These models demonstrate that the co-polarized signals are dominated by the horizontal fracture and the cross-polarized signals only see the cylinder when oriented obliquely to the survey line. Subtracting a horizontal fracture from the co-polarized response demonstrated that the co-polarized and cross-polarized signals are similar with the co-polarized stronger in amplitude and opposite polarity (Figures 3.34-3.37). This subtraction result holds for the sums (P1+P3) and (C1+C3). This indicates that the co-polarized components can be used to guide the analysis of the cross-polarized components in the Altona Flat Rock site data.

Modeling confirms that acquisition of two orthogonal polarizations is needed to fully image a horizontal fracture containing channels. When the channel is oriented parallel or orthogonal to the survey line, summation of the co-polarized data captures all scattered energy. When the channel is oriented oblique to the survey line, anisotropy is apparent in the cross-polarized data, use of the complex trace amplitude envelope and vector summation of the polarization components results in an accurate representation of the scattered energy.

Chapter 4: Altona Flat Rock Field Study

4.1 Methods

4.1.1 Field Site

Three dimensional (3D) multipolarization time lapse GPR data was collected at the Altona Flat Rock site located approximately 15 km northwest of Plattsburg, NY (Figure 4.1). This site is well suited for a ground based GPR survey because bare rock is exposed due to past glacial activity (Rayburn et al., 2005). The rock exposed is Cambrian Potsdam Sandstone, a well-sorted and highly lithified quartzose sandstone. Several laterally extensive subhorizontal (dipping $<3^{o}$) bedding plane partitions are visible in surrounding outcrops. The saturated fracture of interest for this research is located 7.6 m below the surface and intersects with all wells at the field site. The 7.6 m fracture is the first hydraulically conductive fracture below the water table. Results from hydraulic tests show the fracture to have a mean hydraulic aperture of approximately 0.5 mm (Talley et al., 2005).

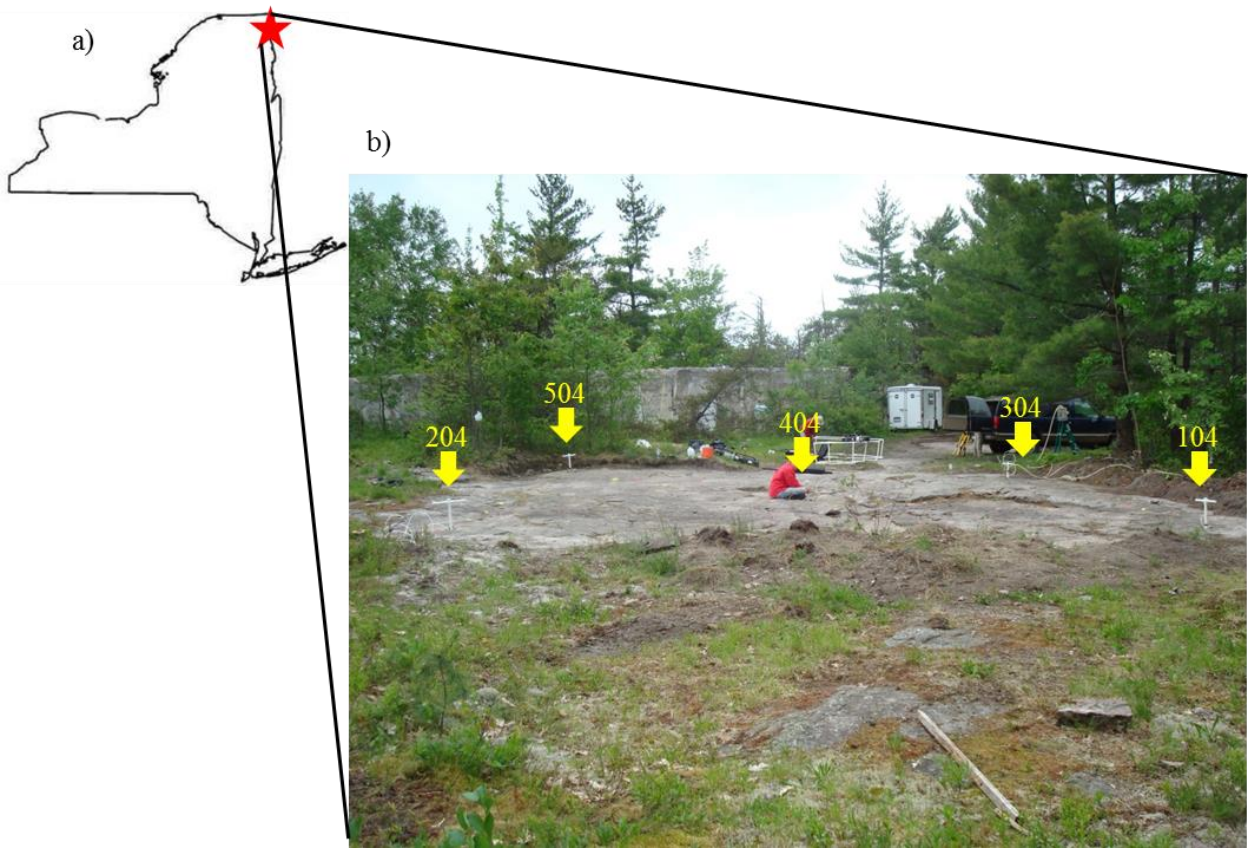

Figure 4.1: Field site. a) Outline of New York State with red star representing approximate location of Altona, NY. b) Field site at Altona, NY with wells labeled.

4.1.2 Tracer Tests

The site is equipped with five open boreholes, 15-cm in diameter, located in a square pattern with one central borehole. A series of saline tracer tests were performed between the five boreholes and were monitored by ground based GPR surveys (Figure 4.2). The saline tracer (table salt) was used to increase the water electrical conductivity in the fracture, which causes changes in the amplitude and phase of the reflected GPR signal, and can be used to highlight fracture channels (Tsoflias and Becker, 2008). Table salt is a good tracer because it behaves predictably in a system therefore formation water quickly returns to normal background electrical conductivity after pumping (Talley et al., 2005). The tracer tests performed were controlled dipole (recirculation) tests and a natural gradient test. Three dipole tests were performed between wells 204-304 (E-W) with water electrical conductivity increasing for each test. Dipole tests were also conducted between wells 104-504 (N-S), and between the outer wells 104,204,304,504 and the central well 404 with various water electrical conductivities. The natural gradient test was performed at well 204 where saline tracer was mixed in the borehole and no artificial gradient was induced. The natural flow of groundwater is to the southeast, approximately in the direction of well 204 to 304 (Hawkins and Becker, 2012). During the tracer tests inflatable rubber packers were placed below the fracture of interest in each well to isolate the fracture from deeper, hydraulically conductive fractures. After each tracer test water was pumped from the fracture until water electrical conductivity returned to background conditions. The orientation of the tracer tests varied in order to image how fluid-flow and flow channeling changes with hydraulic gradient direction.

Before each dipole tracer test water was pumped between the injection well and the pumping well until steady heads and constant electrical conductivity were registered at each well

to confirm good circulation. The pump rate for the E-W dipoles was approximately 8 liters per minute and for the N-S dipole approximately 5 liters per minute. The N-S dipole could not sustain the higher pumping rate attained in the E-W dipole tests indicating relatively poor conductivity between wells 104 and 504. A steady flow rate enabled a uniform dipole to be generated between the injection and pumping wells, allowing for recirculation of the saline tracer. A schematic for the controlled dipole (recirculation) tests is displayed in (Figure 4.3). Water was passed through a 20 L mixing tank on the surface so that tracer concentration and flow rate could be controlled. Tracer concentration was measured at the pumping well and in the mixing tank with a digital electrical conductivity probe approximately every 4-5 minutes (Table 4.1). Table salt was added to the mixing tank during GPR data acquisition to compensate for tracer mass loss due to the natural gradient and to maintain constant fracture water electrical conductivity throughout the test. By maintaining similar electrical conductivity in the mixing tank and out of the pumping well insured that the electrical conductivity of the fracture remained consistent throughout each GPR survey. The E-W dipoles attained steady water electrical conductivities of approximately ~180 mS/m, ~400-500 mS/m, and ~700 mS/m. The N-S dipole was held at a constant electrical conductivity of ~400 mS/m. For the small dipoles, between the outer wells and inner well, fracture electrical conductivities were between ~500-700 mS/m.

The natural gradient test was performed by injecting saline tracer and pumping in well 204. By maintaining the same injection and pumping rate water mixed constantly in the injection borehole allowing the natural gradient to disperse the saline tracer. The natural gradient test borehole electrical conductivities ranged between ~4500-5000 mS/m.

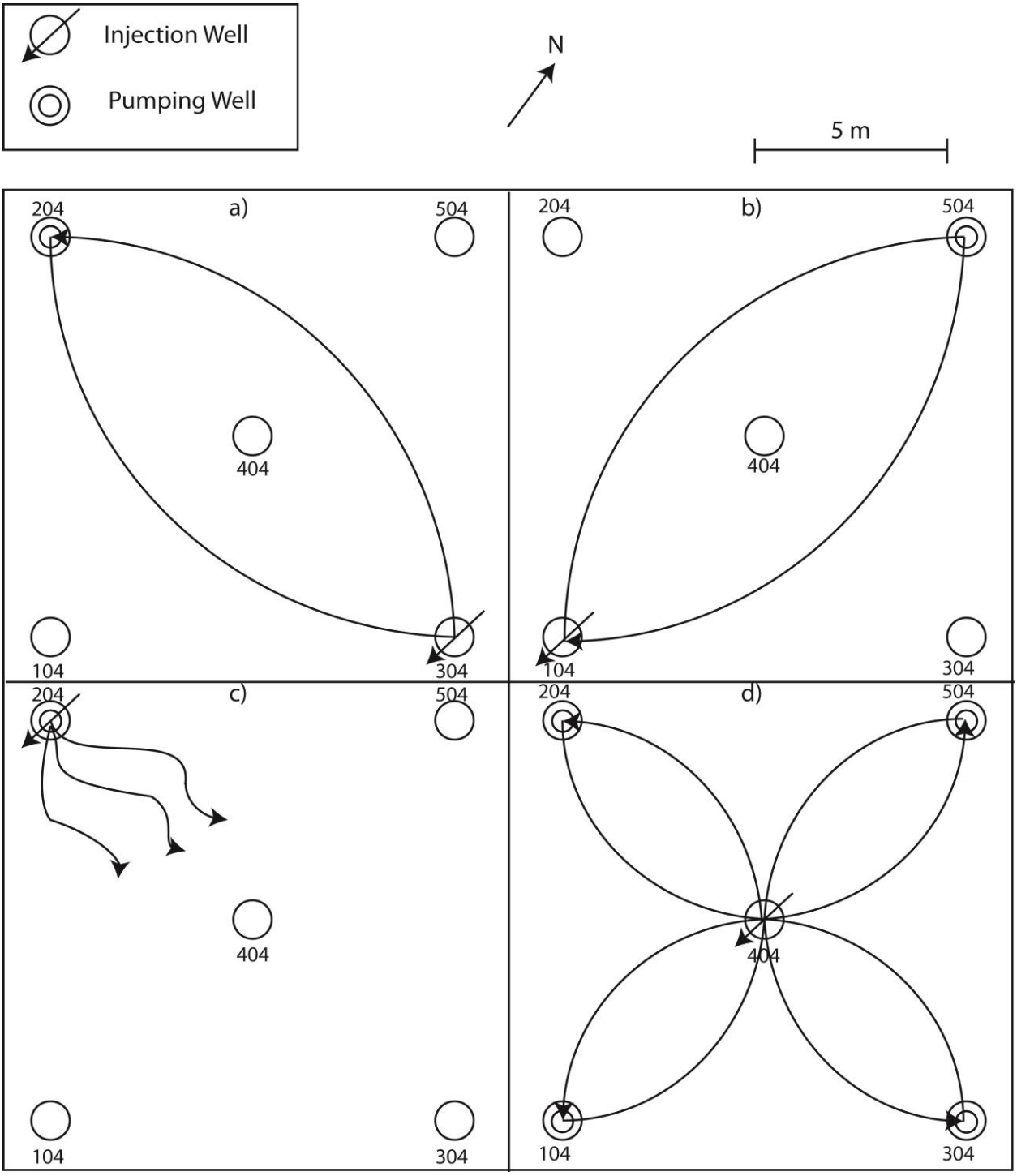

Figure 4.2: Field site diagram showing borehole locations and identifying the injection and pumping boreholes used for the tracer tests. Arrows indicate direction of saline tracer flow. a) E-W Dipole. b) N-S Dipole, c) Natural Gradient, d) Small Dipoles conducted separately between outer boreholes and inner borehole 404.

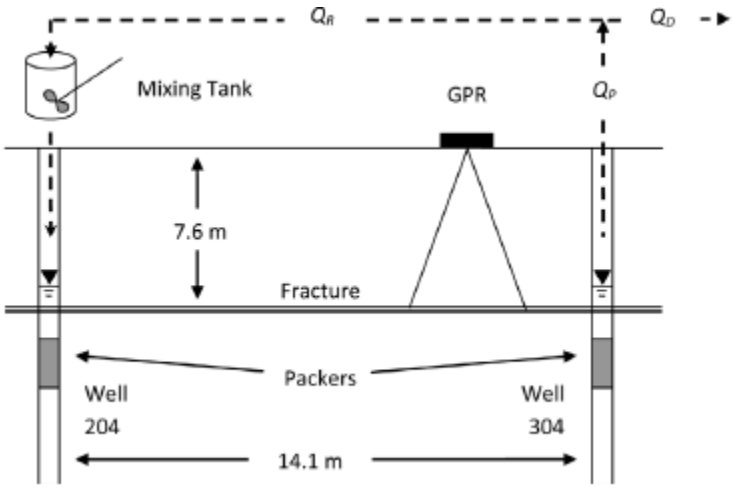

Figure 4.3: Cross-sectional schematic of a tracer experiment. Water from well 304 was reinjected into well 204 to create recirculation. Salt was added into the surface mixing tank. Rates for pumping, reinjection, and discharge are denoted as Q_p Q_r, and Q_D, respectively (From Becker and Tsoflias, 2008).

Tracer Test	Average conductivity pumping well (mS/m)	Average conductivity in injection tank (mS/m)	Average conductivity (mS/m)
50 MHz E-W 180 mS/m	182	210	196
100 MHz E-W 180 mS/m	192	214	203
50 MHz E-W 400 mS/m	468	494	481
100 MHz E-W 400 mS/m	459	497	478
50 MHz E-W 700 mS/m	715	772	744
100 MHz E-W 700 mS/m	691	765	728
50 MHz N-S 400 mS/m	350	443	397
100 MHz N-S 400 mS/m	357	424	391
50 MHz Natural Gradient	4711	4800	4756
100 MHz Natural Gradient	5036	5099	5068
Small Dipole 104-404	500	679	590
Small Dipole 204-404	519	537	528
Small Dipole 304-404	683	690	687
Small Dipole 504-404	571	601	586

Table 4.1: Average conductivity measurements for each tracer test from pumping borehole and injection tank.

4.1.3 Data Acquisition (GPR)

GPR surveys were collected during each tracer test to image the 7.6 m fracture and identify flow paths between wells by monitoring the saline tracer. 3D GPR surveys were conducted at the Altona Flat Rock site using 50 and 100 MHz PulseEKKOPRO systems. These two frequencies were selected to image the fracture because 50 MHz distinguishes changes in electrical conductivity well while 100 MHz gives better resolution of the fracture aperture (Tsoflias and Becker, 2008). There were a total of 16 surveys collected designated by their frequency, tracer test orientation, and tracer concentration (Table 4.2). Background surveys were collected at normal formation water electrical conductivity (~58 mS/m). The gird dimensions were 11.0 m by 10.25 m for the 100 MHz data, 10.5 m by 10.25 m for the 50 MHz data, and 8.0 m by 10.25 m for the 50 MHz small grids (Figure 4.4). Survey acquisition parameters for both frequencies were line spacing 0.5 m, trace spacing of 0.25 m, 32 trace stacks, 308 ns record length, and 0.8 ns sampling interval.

Specialized frames were built to collect multiple polarizations at each trace location (Figure 4.5). The 50 MHz antennas were held at 2.15m separation and the 100 MHz antennas were held at 1.20m separation. The frames held two transmitting and two receiving antennas at a fixed distance apart allowing for the collection of two co-polarized orientations and two cross-polarized orientations at each trace location (Figure 4.6).

The focus of my study is on the contribution of the cross-polarized components C1 and C3 to fracture channel imaging. To acquire multiple polarizations I used two different GPR systems one from the University of Kansas and the other from the University of Texas at Austin. When using two different systems calibrations between systems must be applied to correct for

instrument bias (Sato and Miwa 2000). Calibration tests were performed before and after each tracer test to identify differences in performance between the two systems and to assess their temporal stability (Figure 4.7). GPR calibration data was acquired by placing the frame with the two GPR systems at the same location on the surface. Thirty traces were collected then the system was rotated counter-clockwise (90^{o}) and an additional thirty traces were collected. By placing the systems on the same location each time allowed assessment of the temporal stability of the systems. Rotating the systems placed both sets of antennas at identical positions on the surface allowing calibration of the systems relative to each other. These calibration tests can then be used to create a calibration factor to correct for differences between the two GPR systems.

50 MHz	**100 MHz**
Background	Background
180 mS/m E-W	180 mS/m E-W
400 mS/m E-W	400 mS/m E-W
700 mS/m E-W	700 mS/m E-W
400 mS/m N-S	400 mS/m N-S
Natural Gradient	Natural Gradient
Small Dipole 404-104	
Small Dipole 404-504	
Small Dipole 404-304	
Small Dipole 404-504	

Table 4.2: GPR surveys collected designated by saline tracer test and frequency. Each survey consists of four different polarization grids.

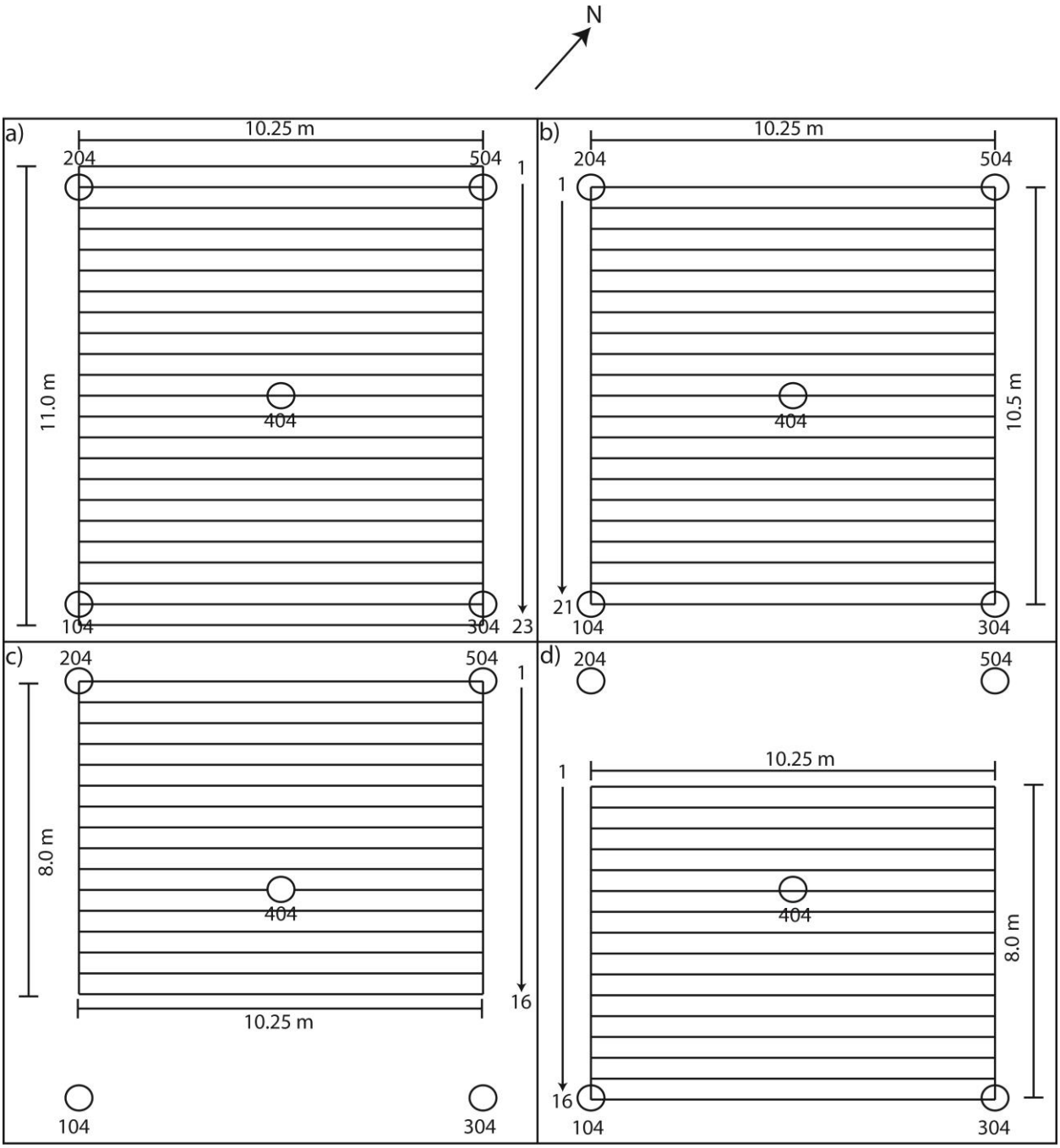

Figure 4.4: GPR survey grids. Lines collected SW-NE. a) 100 MHz grid, b) 50 MHz grid, c) North small dipole grid, d) South small dipole grid.

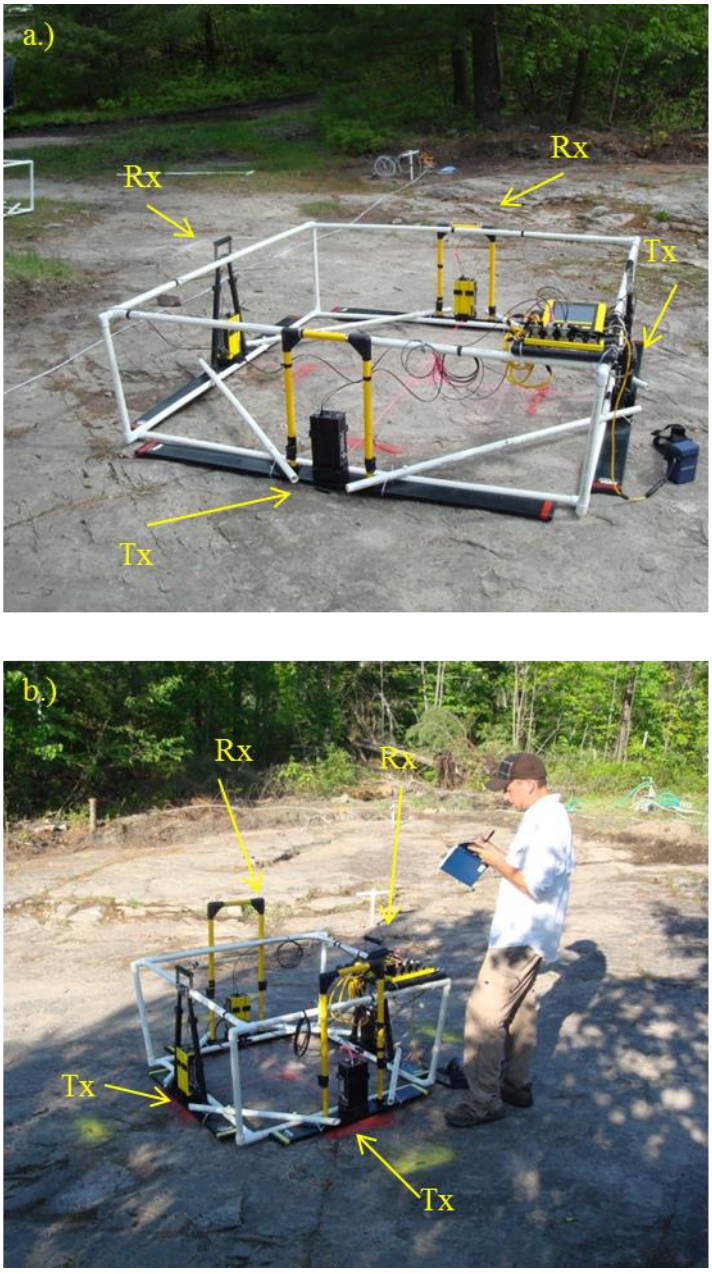

Figure 4.5: PVC frames used to acquire multipolarization GPR data. Tx stands for transmitter and Rx for receiver. a) 50 MHz, b) 100 MHz.

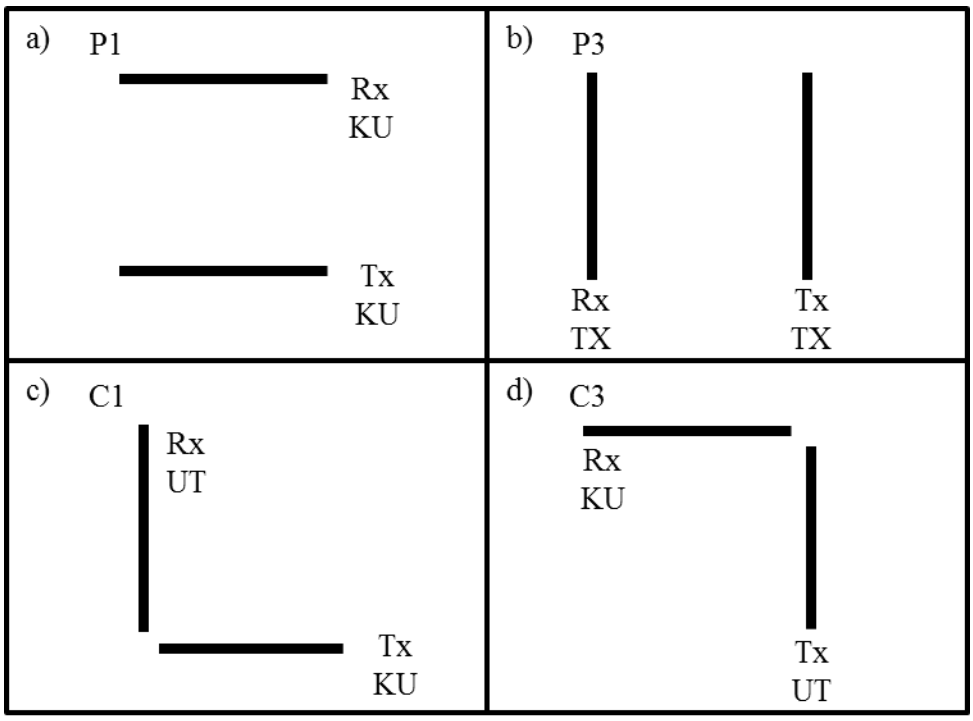

Figure 4.6: Co-polarized and cross-polarized antenna orientations. Tx stands for transmitter and Rx for receiver, and labeled by system KU for the University of Kansas UT for University of Texas. a) P1 polarization, b) P3 polarization, c) C1 polarization, d) C3 polarization.

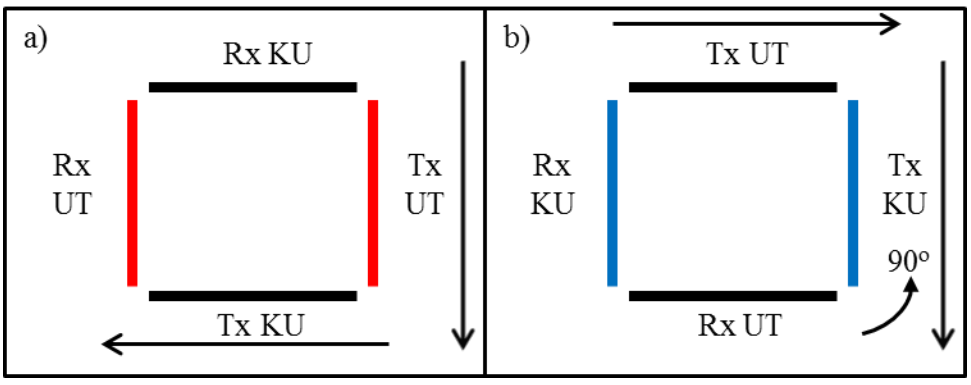

Figure 4.7: Calibration setup with arrows indicating antenna orientation, antennas labeled Tx for transmitter Rx for receiver, and labeled by GPR system KU for the University of Kansas UT for University of Texas at Austin. (Red) P3 normal (Blue) P1 rotated. a) Calibration survey, b) Rotated calibration survey.

4.1.4 GPR Data Processing and Analysis

The GPR data was processed using standard methods commonly employed in GPR surveys, with the exception of the mulit-channel system calibration. The data processing steps described below were completed using Sensors and Software's EKKO View Deluxe and MathWorks MATLAB software (Table 4.3). First, a Dewow filter was applied to remove low frequency noise from the data. The low frequency noise is inherent in the GPR antennas and is induced by the antennas themselves. Next, a low-pass filter of 156.25 Hz was applied to remove high frequency noise from the data. After frequency filtering, 2D Kirchoff migration was applied to collapse diffractions and correct for the minimal dip of the fracture. A migration velocity of 0.11 m/ns was obtained by CMP tests conducted at site. Data was then loaded into MATLAB and time zero corrections were applied to correct for instrumentation time drift. Figures 4.8-4.9 show cross-polarized components (C1 and C3) before and after processing. Then the data was written into SEG-Y format and loaded into Seismic Microtechnology's Kingdom Suite for interpretation.

The 7.6 m fracture of interest is located at approximately ~140 ns two-way travel time and is visible in the co-polarized components (P1 and P3) as a trough (Figures 4.10ace-4.11ace). The cross-polarized components (C1 and C3) show no coherent reflection (Figures 4.10bdf-4.11bdf) corresponding to the horizontal fracture. Tsoflias et al. (2012) picked the minimum amplitude of the trough in the co-polarized components and generated amplitude maps to identify fracture channeling. Since there was no coherent event that could be picked in the cross-polarized components I used the co-polarized components to guide my analysis. Modeling in previous chapter (Figures 3.34-3.37) indicate that the co-polarized signal energy is located in

same position as the cross-polarized energy. I picked the zero crossings above and below the fracture trough in the co-polarized components and transferred those horizons onto the corresponding cross-polarized components. The zero crossings from P1 were transferred to C1, P3 to C3, and (P1+P3) to (C1+C3). The sums (P1+P3) and (C1+C3) are created by summing the individual polarization components. The zero crossing time picks were then exported into MATLAB for analysis.

4.1.5 GPR Calibration and Scaling

Subsequently, the two GPR systems were calibrated. Calibrating the two systems ensures that differences in recorded signal amplitude caused by the different instrumentation are minimized. To calibrate the systems I calculated the root mean square (RMS) amplitude for each trace in the calibration surveys from 58-112 ns, a range below the direct arrival to above the fracture for both the UT and KU systems.

$$X_{rms} = \sqrt{\frac{1}{n}(x_1^2 + x_2^2 + \cdots + x_n^2)} \qquad (13)$$

Where x is the amplitude at each sample point. The RMS value is calculated by the square root of the arithmetic mean of the squares of n samples. The 58-112 ns interval of the subsurface is expected to remain invariant during the tracer tests and therefore should yield similar RMS amplitudes in time-lapse. The P3 normal and P1 rotated positions are used to calculate the calibration factors (Figure 4.7). These polarizations were used because the antennas were located at the same positions on the surface insuring the same point in the subsurface is measured. I then calculated the average of the thirty RMS values from the calibration surveys and bulk shifted the UT system average to match the KU system average to generate calibration factors. Figures 4.12-4.13 show the 50 MHz and 100 MHz 700 mS/m E-W calibration factor calculation. The calibration factor scales the amplitudes from the UT system to correct for the instrument

difference between the two systems (Table 4.4). A calibration factor is computed and applied to the UT system (C3 polarization) for each GPR survey. The calibration factors are on the order of $\pm 10\%$ indicating that instrument performance is comparable.

After the instrument calibration factors were applied each survey and polarization was scaled to its corresponding background survey. Scaling the surveys to background water electrical conductivity accounts for the temporal amplitude instability of the GPR systems. To scale each survey to background an RMS value from 84-100 ns for the 50 MHz and 80-92 ns for the 100 MHz was calculated at each trace location in each survey. These ranges were selected because they correspond to a reflector above the fracture that is unaffected by the saline tracer. The RMS value for each trace was then divided by the corresponding background RMS value to generate a scaling matrix for each survey (Figures 4.14-19). This operation was done separately for C1 and C3 polarizations. The scaling matrixes were then applied to produce the final scaled-calibrated dataset.

Next C1 and C3 were summed (C1+C3) to enhance cross-polarized imaging of the channel as demonstrated in the numerical modeling (Figures 3.34-3.37) .The last step before generating amplitude maps of the fracture was to remove lines 1 and 21 from the 50 MHz grids, lines 1 and 2 from the 100 MHz grids, line 1 from North Dipole grids, and line 16 from South Dipole grids (Figure 4.4). These lines were removed because of anomalous high amplitudes observed along the edges of the survey grids. Amplitude maps of the fracture were created in MATLAB by calculating the RMS between the zero crossings time picks selected in Kingdom Suite on the co-polarized profiles.

Processing Steps
1.) Dewow filter (EKKO View Deluxe)
2.) Low-pass filter of 156.25 MHz (EKKO View Deluxe)
3.) 2-D Kirchoff migration using 0.11 m/ns velocity (EKKO View Deluxe)
4.) Time zero corrections (MATLAB)
5.) Zero crossings picked (Kingdom Suite)
6.) Calibration factor applied (MATLAB)
7.) Scaling matrixes applied (MATLAB)
8.) Sum C1 and C3 Polarizations (MATLAB)
9.) Remove lines from 50 and 100 MHz grids (MATLAB)

Table 4.3: Processing steps for GPR data.

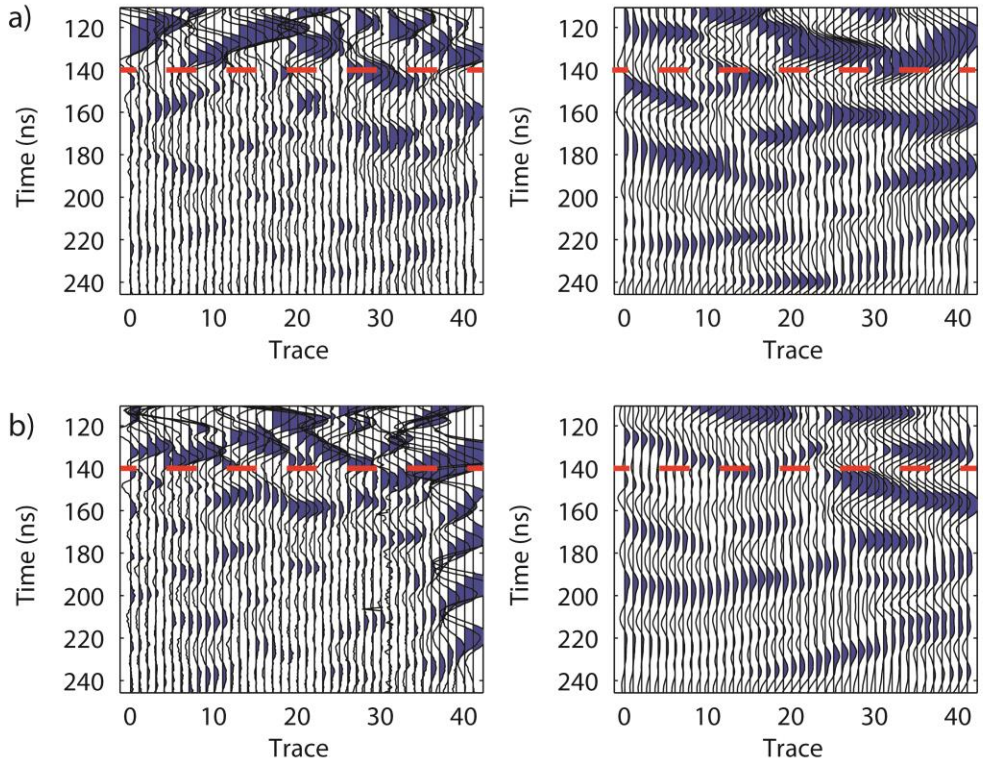

Figure 4.8: Line 16 from 50 MHz 700 mS/m grid. Gain applied for display purposes. Approximate fracture location marked at 140 ns by red dashed line. (Left) dewow applied (Right) processing steps 1-4 applied (Table 4.3). a) C1, b) C3.

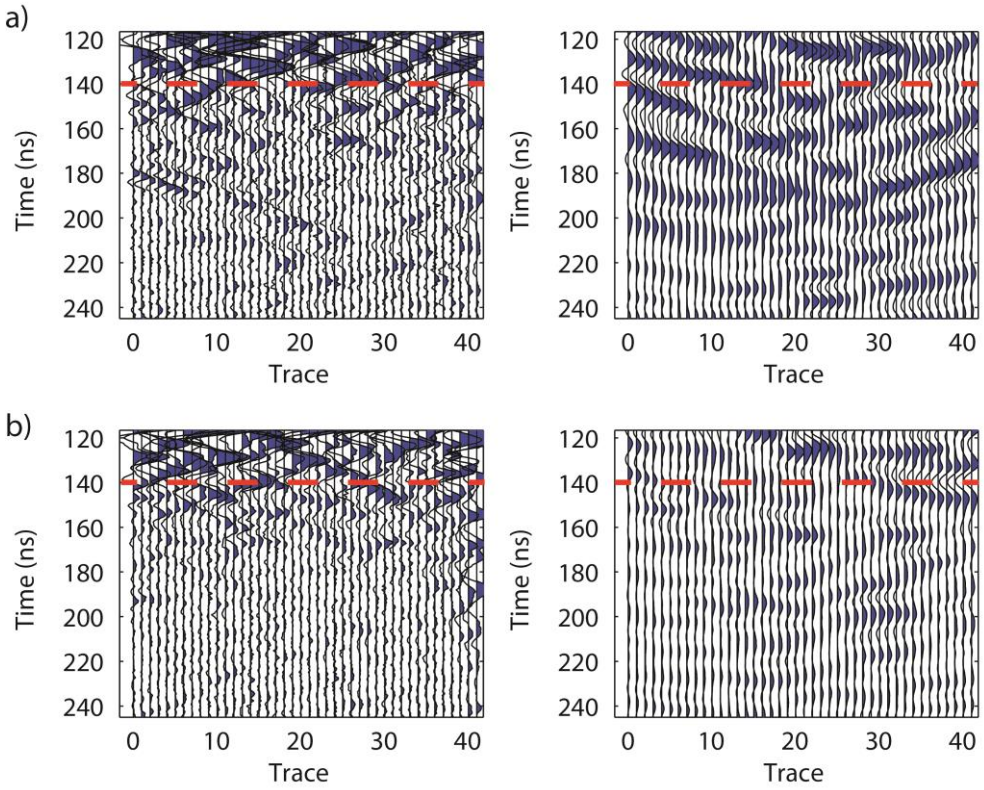

Figure 4.9: Line 16 from 100 MHz 700 mS/m grid. Gain applied for display purposes. Approximate fracture location marked at 140 ns by red dashed line. (Left) dewow applied (Right) processing steps 1-4 applied (Table 4.3). a) C1, b) C3.

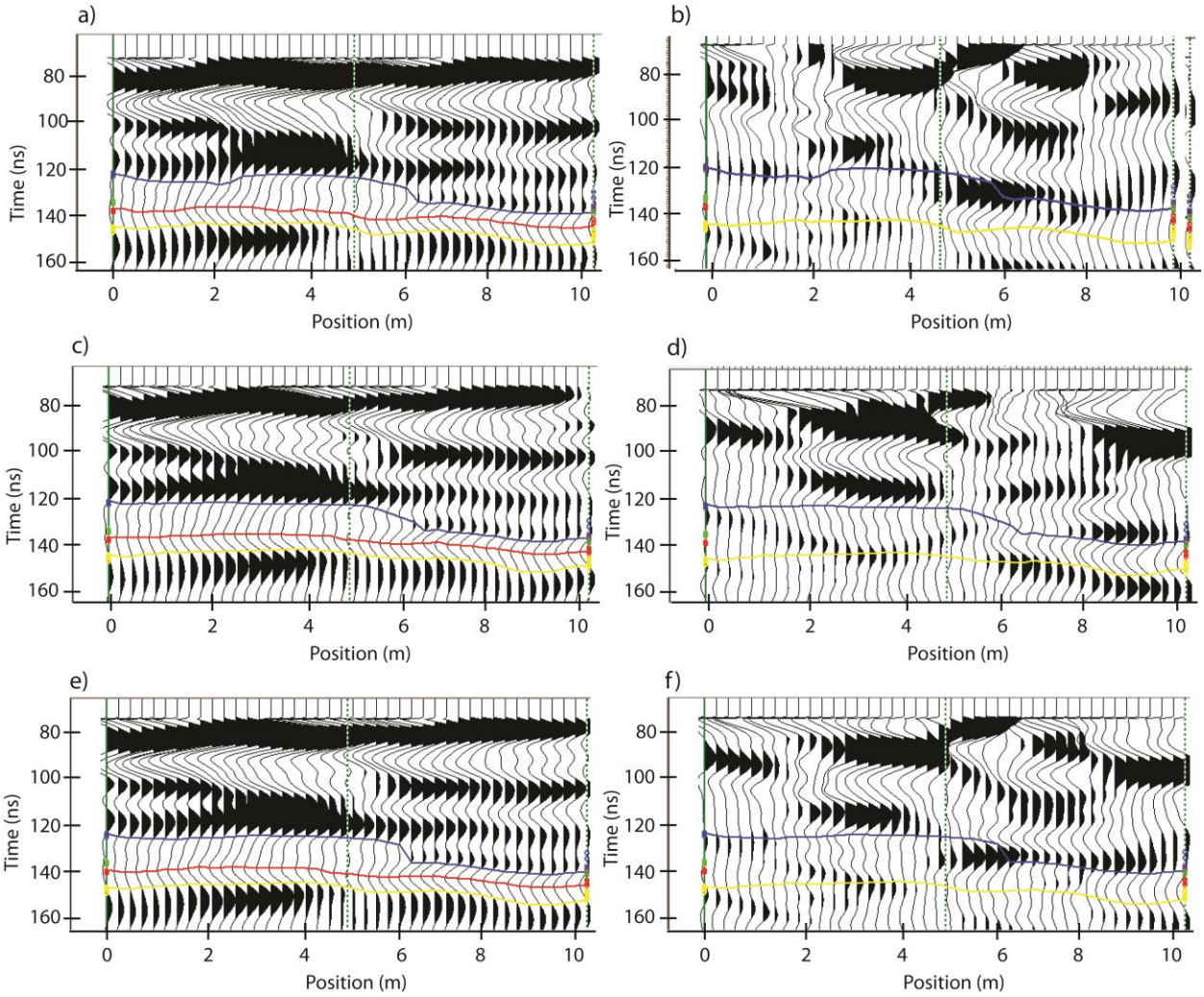

Figure 4.10: Line 16 from 50 MHz 700 mS/m grid showing the interpreted fracture hrozion at 140 ns. Blue line is the zero crossing above fracture, yellow line is the zero crossing below fracture, and red line is the maximum through pick of fracture reflection. Zero crossing time picks were transferred to the corresponding cross-polarized components to identify the interval of the fracture a) P1, b) C1, c) P3, d) C3, e) P1 + P3, f) C1 + C3.

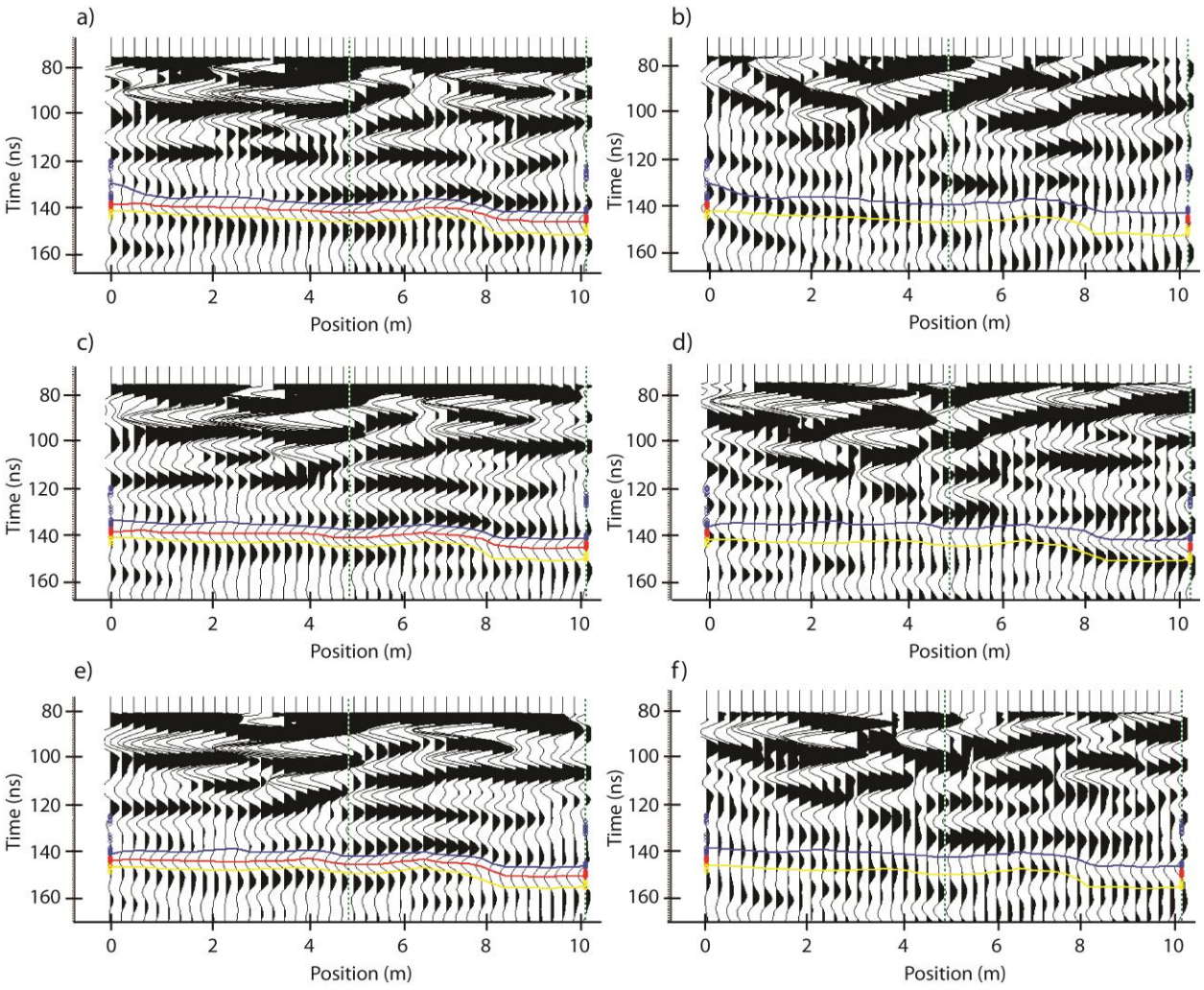

Figure 4.11: Line 16 from 100 MHz 700 mS/m grid showing the interpreted fracture hrozion at 140 ns. Blue line is the zero crossing above fracture, yellow line is the zero crossing below fracture, and red line is the maximum through pick of fracture reflection. Zero crossing time picks were transferred to the corresponding cross-polarized components to identify the interval of the fracture a) P1, b) C1, c) P3, d) C3, e) P1 + P3, f) C1 + C3.

50 MHz	Calibration Factor	100 MHz	Calibration Factor
Background	1.0414	Background	1.0980
180 mS/m E-W	0.8956	180 mS/m E-W	0.8969
400 mS/m E-W	1.0911	400 mS/m E-W	1.0065
700 mS/m E-W	1.1043	700 mS/m E-W	0.9191
400 mS/m N-S	1.0078	400 mS/m N-S	0.9034
Natural Gradient	1.0115	Natural Gradient	0.9307
Small Dipole 404-104	0.9869		
Small Dipole 404-204	1.0254		
Small Dipole 404-304	1.0782		
Small Dipole 404-504	1.0991		

Table 4.4: Calibration factors applied to UT system (C3 polarization) to correct for instrument amplitude difference between the KU and UT GPR systems.

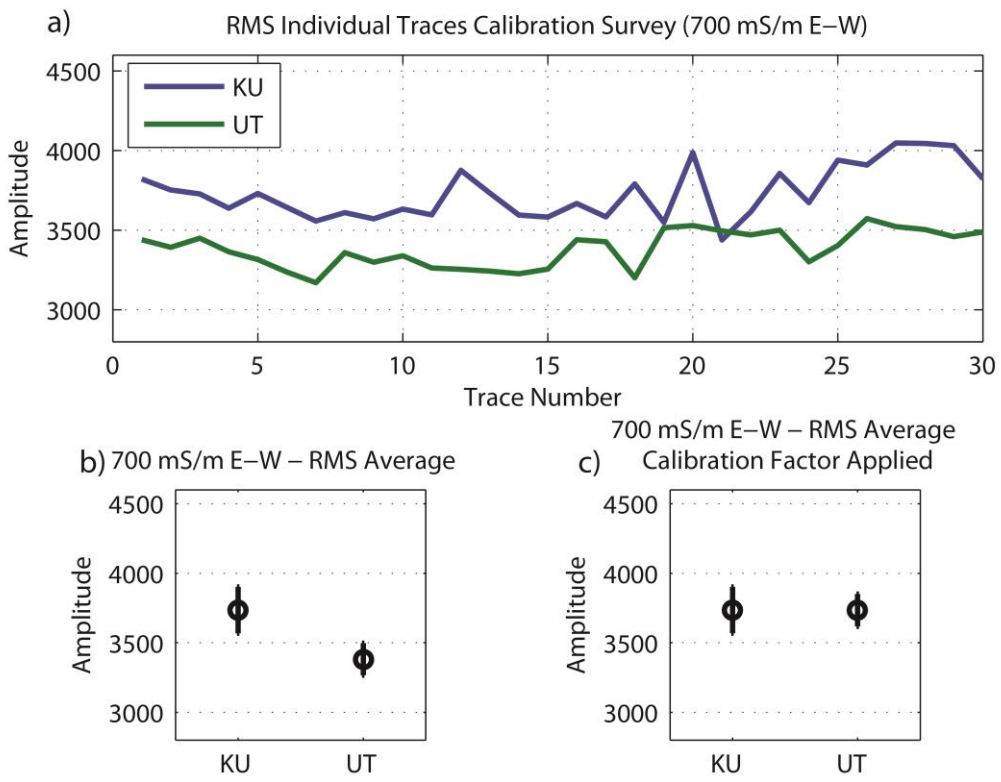

Figure 4.12: Visual representation of calculating the amplitude calibration factor for the 50 MHz 700 E-W survey. a) The RMS is calculated from 58-112 ns for each trace in the calibration survey, b) Average RMS for both systems, c) The UT system is bulk shifted to match the KU system to generate a calibration factor that is then applied to UT system data. Note b) and c) plotted with one STD.

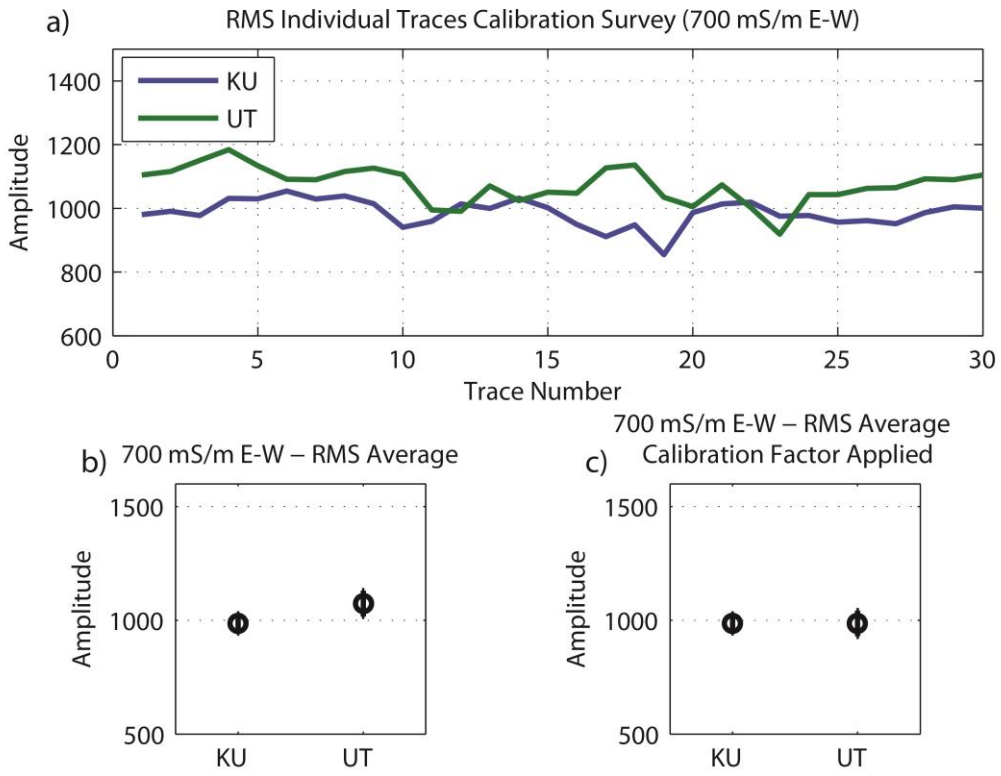

Figure 4.13: Visual representation of calculating the amplitude calibration factor for the 100 MHz 700 E-W survey. a) The RMS is calculated from 58-112 ns for each trace in the calibration survey, b) Average RMS for both systems, c) The UT system is bulk shifted to match the KU system to generate a calibration factor that is then applied to UT system data. Note b) and c) plotted with one STD.

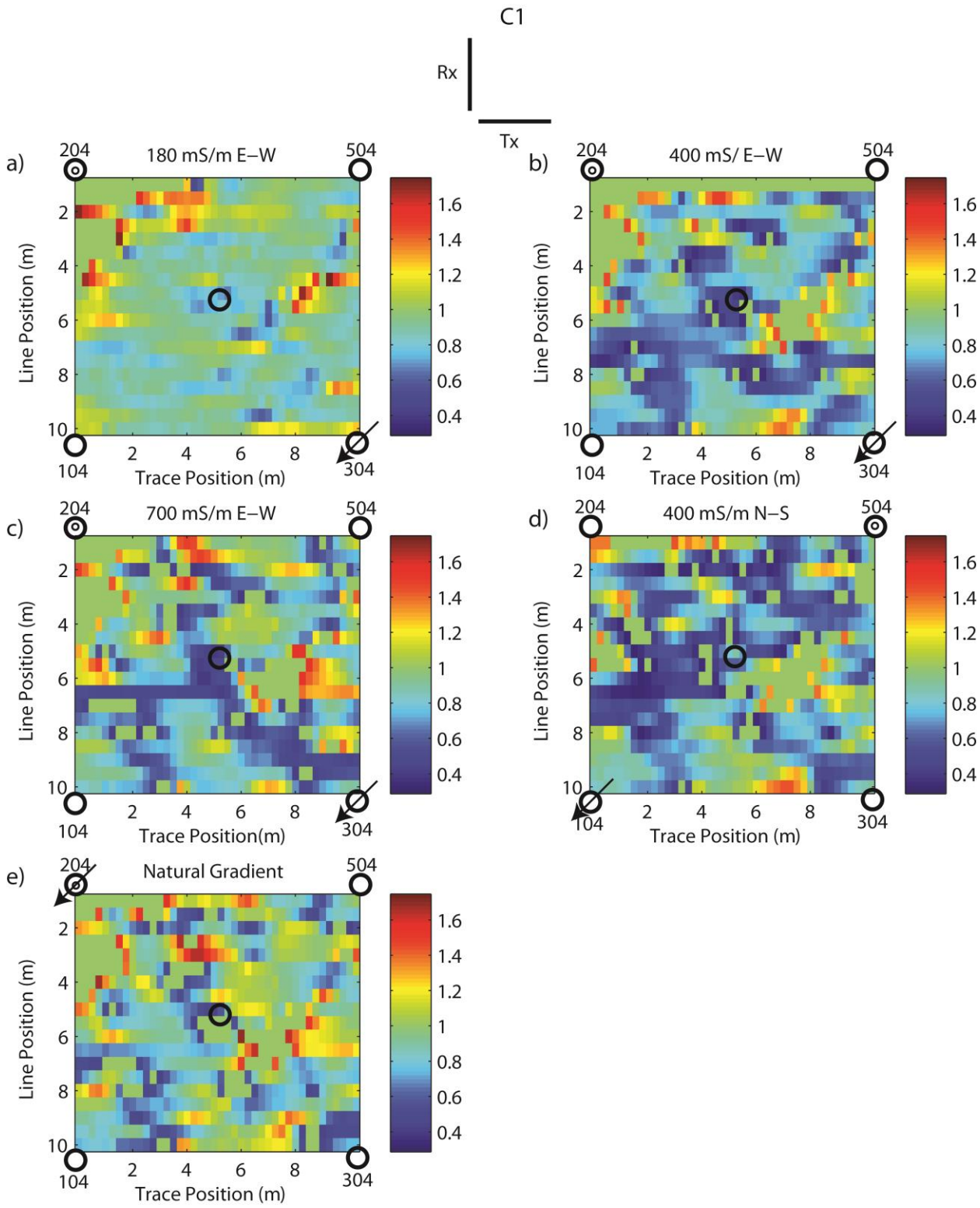

Figure 4.14: Scaling matrixes applied to C1 50 MHz surveys. a) 180 mS/m E-W, b) 400 mS/m E-W, c) 700 mS/m E-W, d) 400 mS/m N-S, e) Natural Gradient.

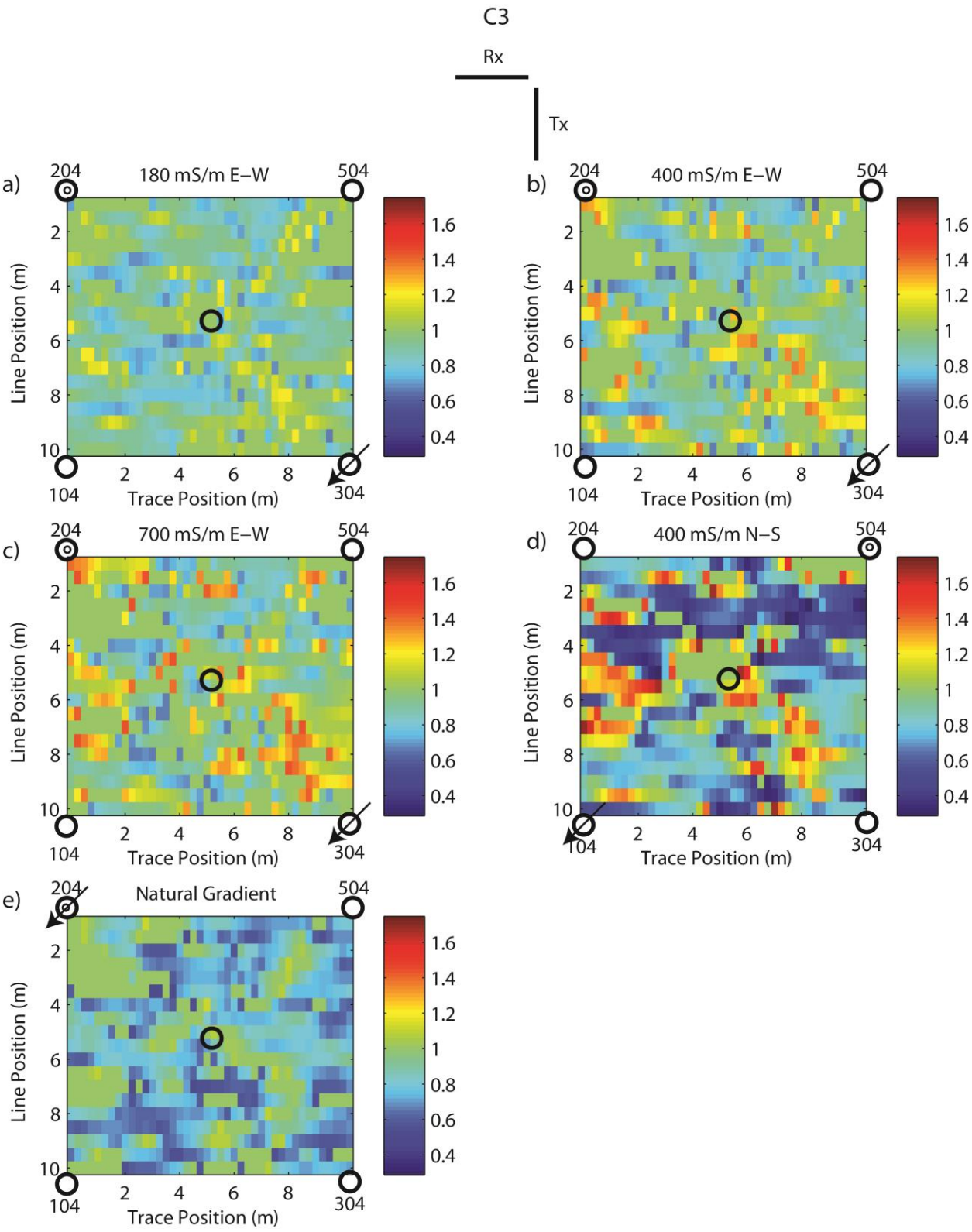

Figure 4.15: Scaling matrixes applied to C3 50 MHz surveys. a) 180 mS/m E-W, b) 400 mS/m E-W, c) 700 mS/m E-W, d) 400 mS/m N-S, e) Natural Gradient.

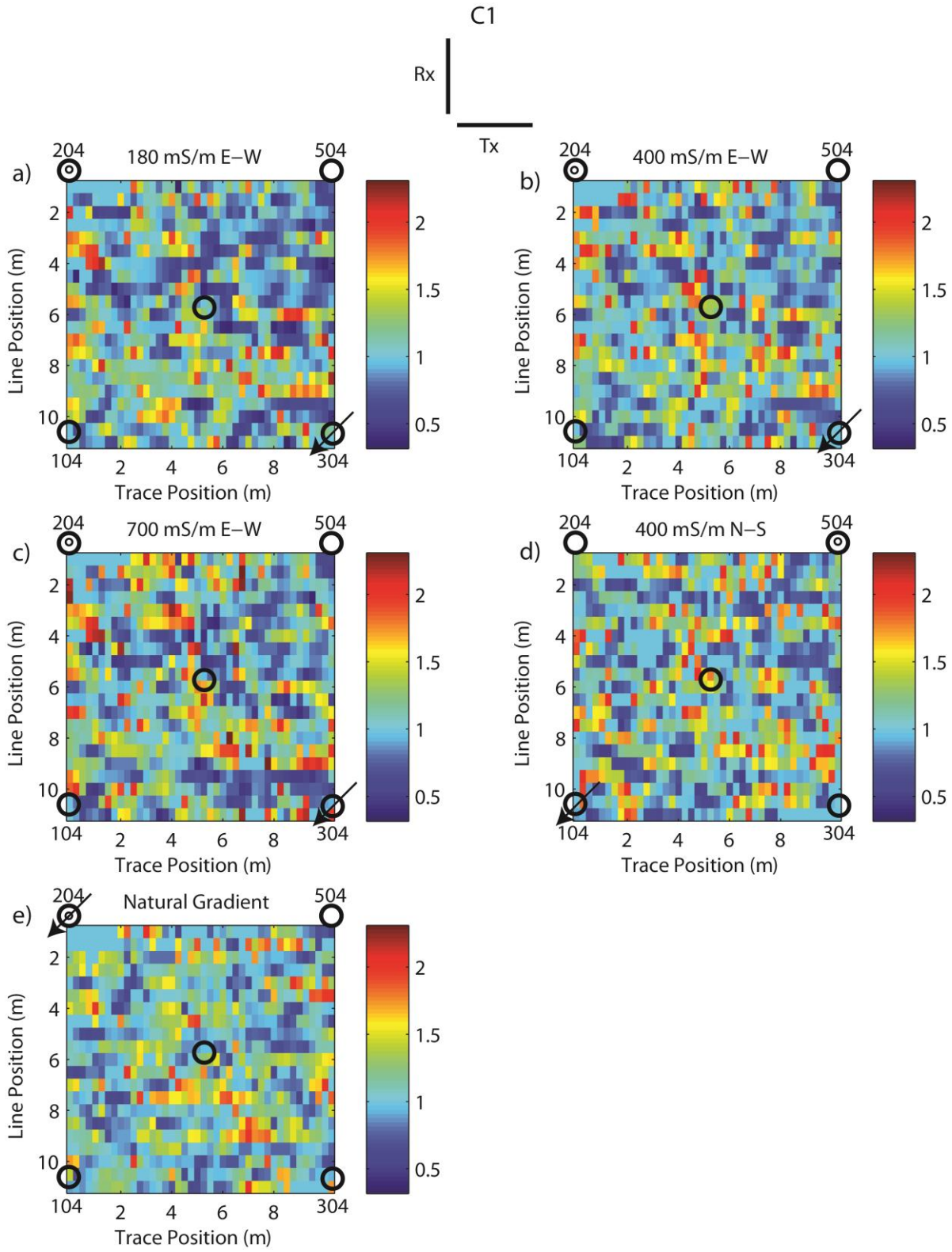

Figure 4.16: Scaling matrixes applied to C1 100 MHz surveys. a) 180 mS/m E-W, b) 400 mS/m E-W, c) 700 mS/m E-W, d) 400 mS/m N-S, e) Natural Gradient

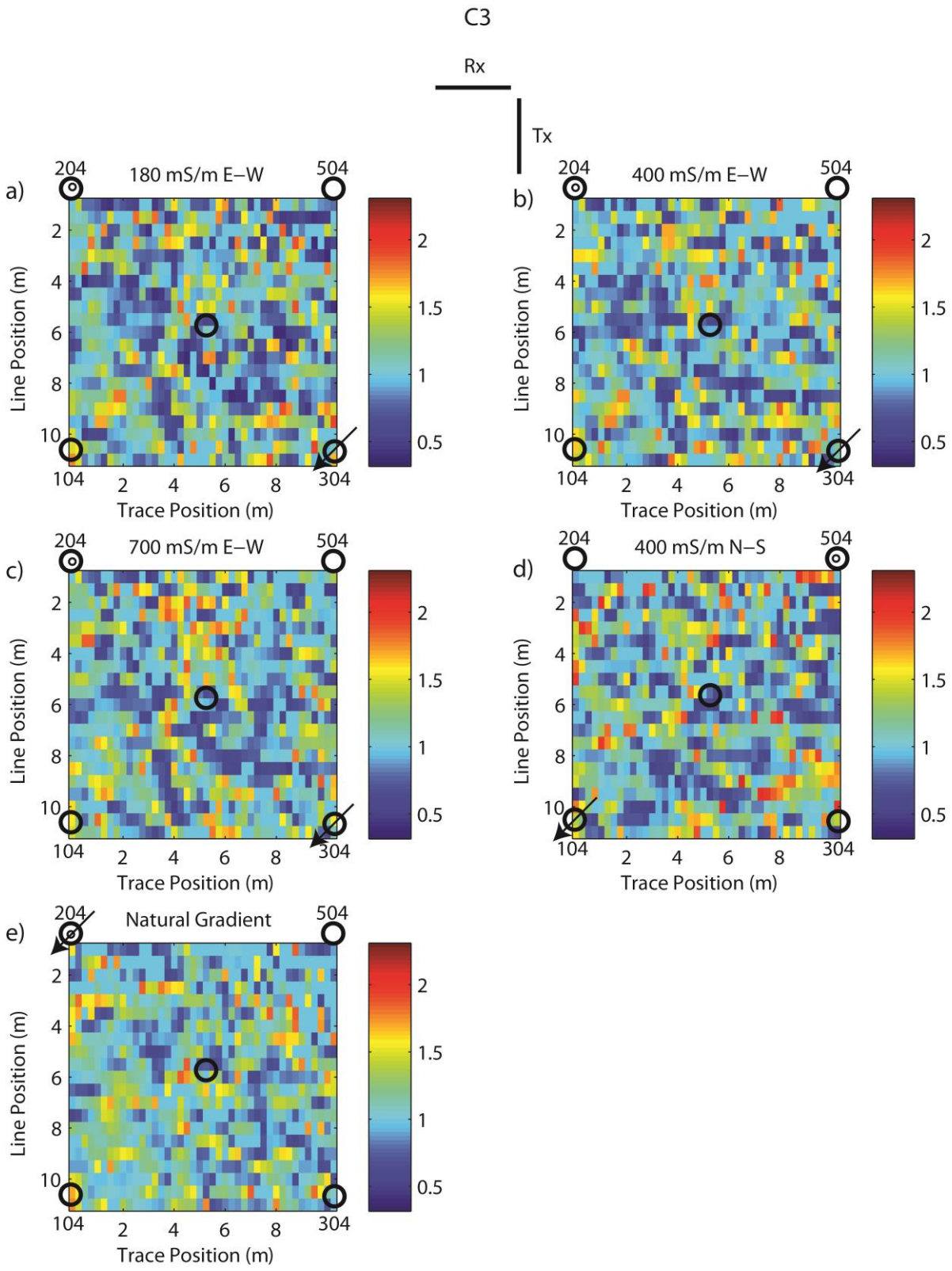

Figure 4.17: Scaling matrixes applied to C3 100 MHz surveys. a) 180 mS/m E-W, b) 400 mS/m E-W, c) 700 mS/m E-W, d) 400 mS/m N-S, e) Natural Gradient.

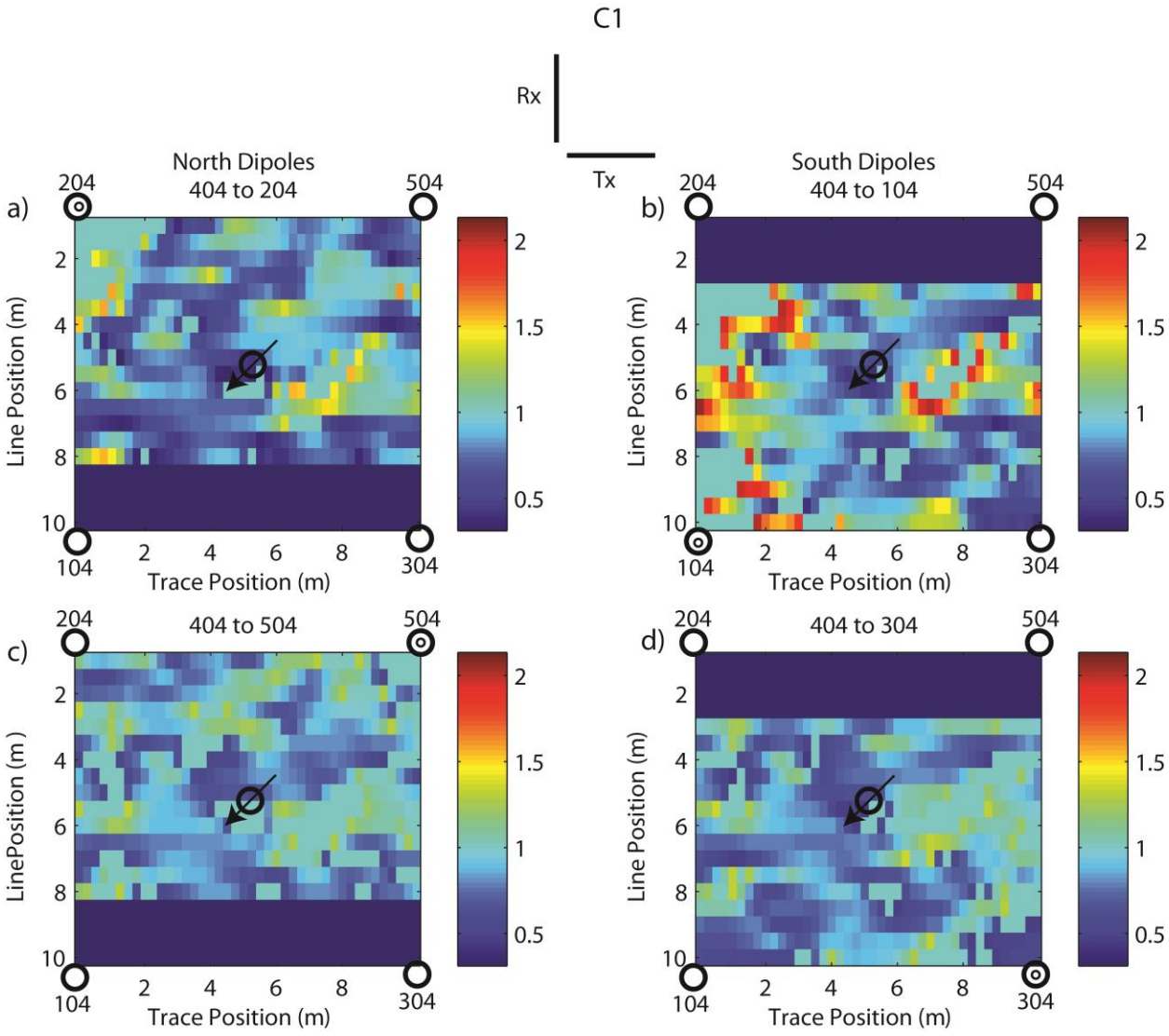

Figure 4.18: Scaling matrixes applied to C1 50 MHz small dipole surveys. (Left) North Dipoles. (Right) South Dipoles. a) 404 to 204, b) 404 to 104, c) 404 to 504, d) 404 to 304.

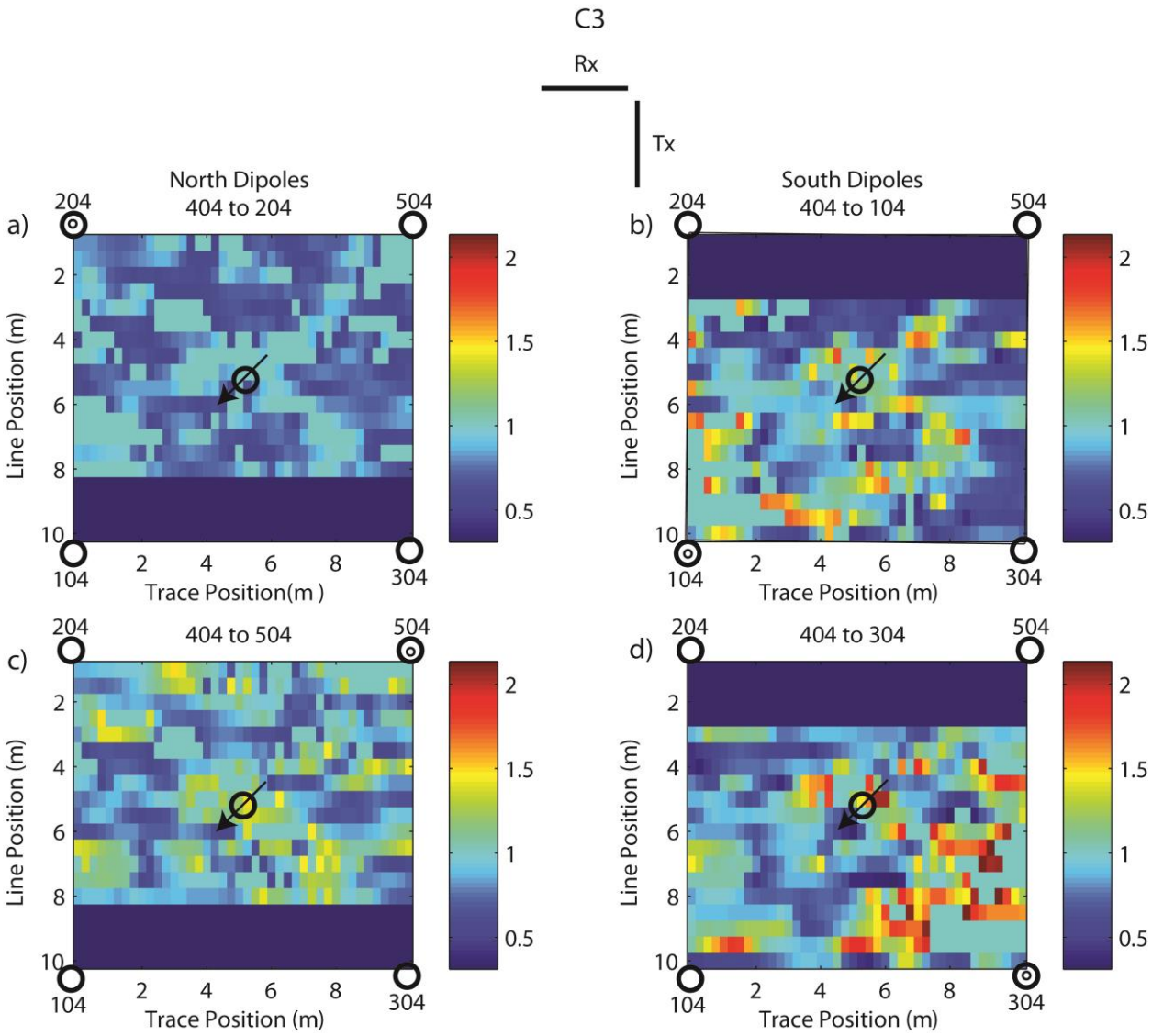

Figure 4.19: Scaling matrixes applied to C3 50 MHz small dipole surveys. (Left) North Dipoles. (Right) South Dipoles. a) 404 to 204, b) 404 to 104, c) 404 to 504, d) 404 to 304.

4.2 Altona Tracer Test GPR Results

The purpose of the field study was to extract useful information from the cross-polarized components (C1 and C3). Models in the previous chapter show that the cross-polarized components do not image horizontal planar targets (Figure 3.10) and only channels oriented oblique to survey line are imaged (Figures 3.12-3.15). GPR surveys were collected SW to NE (Figure 4.4) therefore, the cross-polarized components should identify fracture channeling oriented E-W or N-S. The co-polarized components (P1 and P3) should provide images of the horizontal fracture and channels oriented parallel and perpendicular to the survey lines. The co-polarized data is analyzed in a complementary thesis by Matt Baker (2013).

4.2.1 50 MHz GPR Surveys

50 MHz cross-polarized raw and scaled-calibrated amplitude maps of the 7.6 m fracture are shown in Figures 4.20-4.23. C1 and C3 background surveys are significantly weaker than other surveys and show no amplitude trend between wells (Figures 4.20a-4.23a). C1 and C3 raw amplitude maps show no consistent trends (Figures 4.20 and 4.22). All C1 grids show stronger amplitude anomalies near pumping wells 204 for E-W grids and 504 for N-S grid (Figures 4.20-4.21). The metallic pump located in the pumping borehole may have caused the anomalies. C1 scaled-calibrated amplitude maps show a strong amplitude trend from well 204–304 in the 400 mS/m, 700 mS/m, and Natural Gradient tracer test data (Figure 4.21cdf). Data from the C1 scaled-calibrated 400 mS/m experiment shows similar amplitude trends as the E-W surveys i.e. orthogonal to the direction of the flow dipoles. This result suggests tracer is being lost to the natural gradient, which flows to the southeast (Figure 4.21e). C3 scaled-calibrated E-W and Natural Gradient surveys show weaker amplitude trends than C1 E-W surveys (Figure 4.23). No

pumping interference is observed in the C3 data with the exception of the 400 mS/m N-S gird (Figure 4.23e).

Figures 4.24-4.26 show summed (C1+C3) amplitude maps. In the raw and scaled-calibrated summing the individual polarizations reduces the polarization affects caused by dipole antennas and it enhances the cross-polarized images of the channels (Lehmann et al. 2000; Tsoflias et al. 2012). Background sums have weakest amplitudes and show no amplitude trends between wells (Figure 4.24a-4.25a). Raw and scaled-calibrated sum amplitude maps 400 mS/m E-W, 700 mS/m E-W, and Natural Gradient show good flow channeling between wells 204-304 with channels becoming more apparent with increasing electrical conductivity (4.24bcdf-4.25bcdf). A log scale amplitude map created for the scaled-calibrated data (Figure 4.26) clearly shows strong evidence of a channel from 204-304 in 400 mS/m, 700 mS/m, and Natural Gradient surveys. This suggests a narrow E-W oriented flow channels between wells 204-304 during the E-W and Natural Gradient dipole flow tests. N-S 400 mS/m scaled-calibrated (Figure 4.25-4.26e) show amplitudes trending E-W also, but distributed over a larger area of the fracture surface.

To analyze the change in amplitude of the fracture interval caused by the saline tracer, average amplitude plots were created. Average amplitude of the RMS interval plotted with one STD for each survey and polarization are shown in Figures 4.27-4.28. C1 average amplitude raw and scaled-calibrated events are stronger in the majority of the surveys than C3 (Figure 4.27). The C1 180 mS/m E-W survey data exhibits strong amplitude and large STD. Both C1 and C3 raw average data amplitudes show no trend with increasing electrical conductivity, but scaled-calibrated data show increasing amplitude with increasing electrical conductivity (Figure 4.27). Both the raw and scaled-calibrated sums (C1+C3) show increasing amplitude with increasing

electrical conductivity (Figure 4.28) in agreement with numerical modeling (Figure 3.15). The 180 mS/m E-W and 400 mS/m N-S survey have high amplitudes with large STD resulting from high amplitude values near pumping wells 204 and 504 respectively. Those high amplitude areas are localized and are not considered representative to the rest of the survey. The large amplitudes may be the result of interference of the the metallic pump. Therefore, averages were also calculated without these high amplitude values and are shown by dashed lines in figures 4.27-4.28. The dashed line trends are in better agreement with expected amplitude trends resulting from varying the electrical conductivity of water in the fracture. In addition the STD of the corresponding surveys is in better agreement with the variability observed in other surveys conducted at the field site.

4.2.2 50 MHz GPR Surveys Summary

1. Calibration and scaling are needed to account for instrument response and temporal changes in amplitude. After scaling evidence of flow channeling becomes apparent.
2. C1 and C3 do not image the horizontal fracture or channels oriented perpendicular or parallel to survey line. They only image channels oblique to survey lines.
3. Weak evidence of flow channels is present in individual polarizations.
4. Summing the individual polarizations (C1+C3) shows clear amplitude trends consistent with the orientation of the dipole flow tests.
5. Increasing water electrical conductivity increases the RMS amplitude of the fracture reflection.

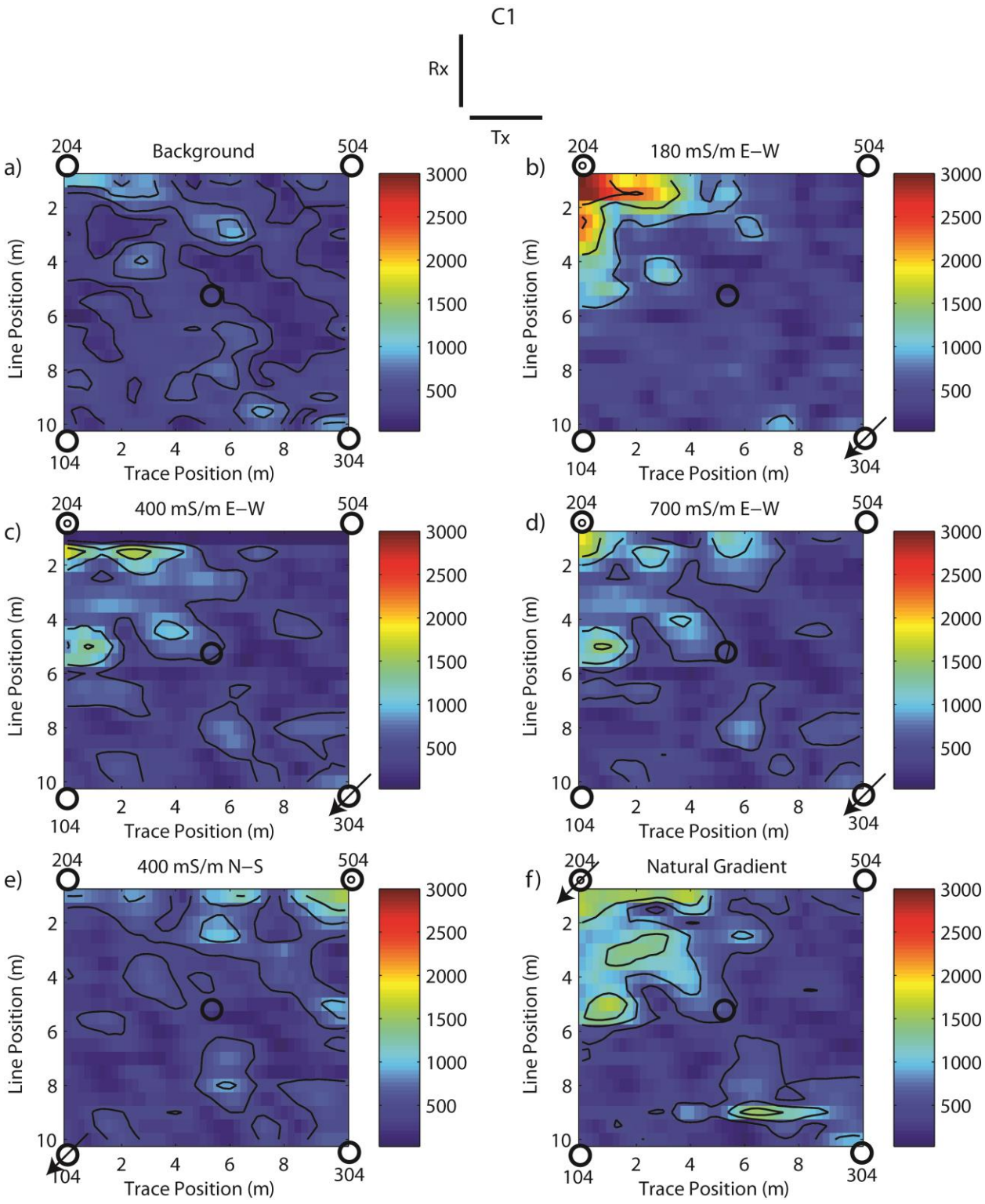

Figure 4.20: 50 MHz C1 raw amplitude maps of fracture. Color signifies amplitude units, contour interval is 500 units. a) Background, b) 180 mS/m E-W, c) 400 mS/m E-W, d) 700 mS/m E-W, e) 400 mS/m N-S, f) Natural Gradient.

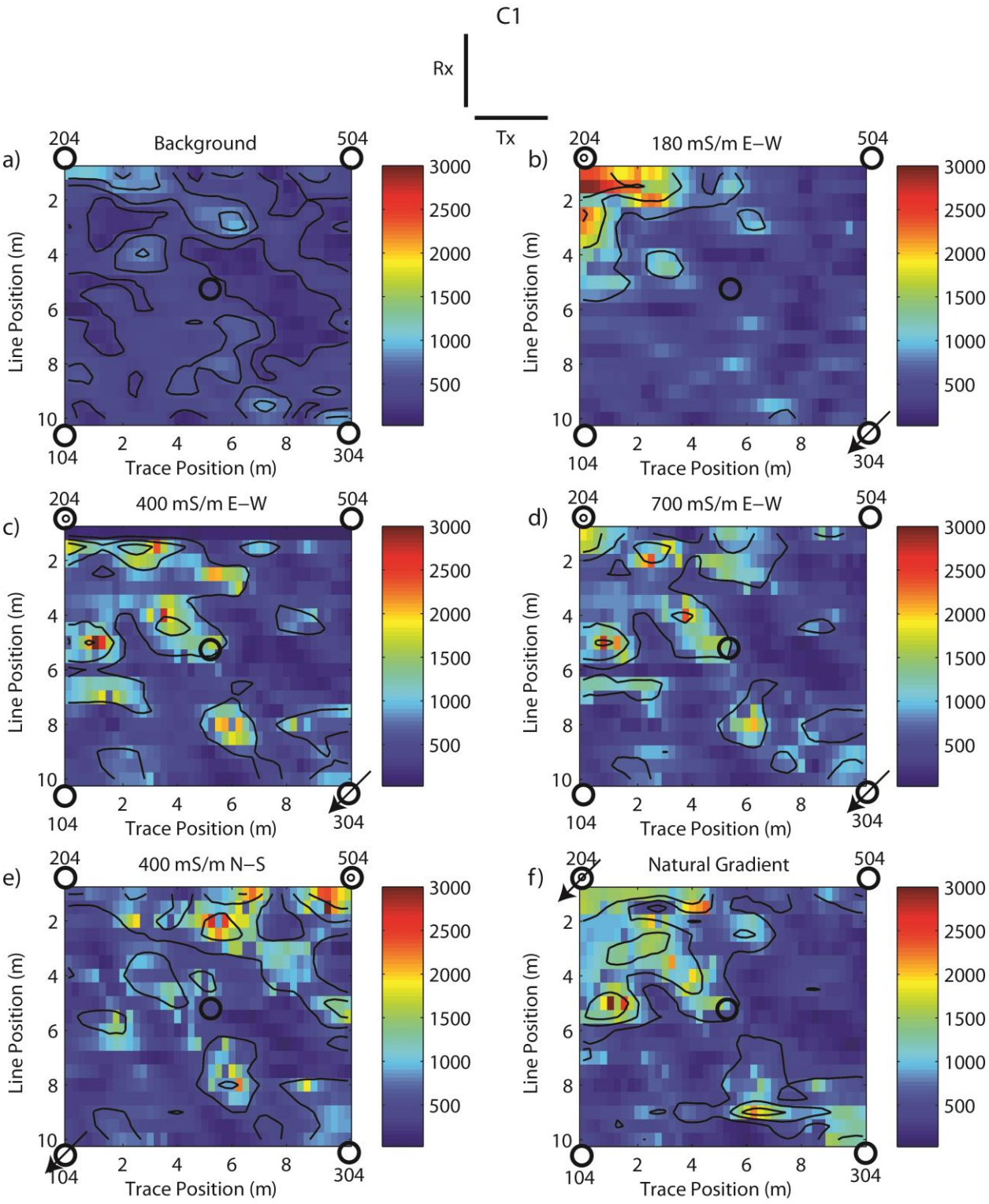

Figure 4.21: 50 MHz C1 scaled-calibrated amplitude maps of fracture. Color signifies amplitude units, contour interval is 500 units. a) Background, b) 180 mS/m E-W, c) 400 mS/m E-W, d) 700 mS/m E-W, e) 400 mS/m N-S, f) Natural Gradient.

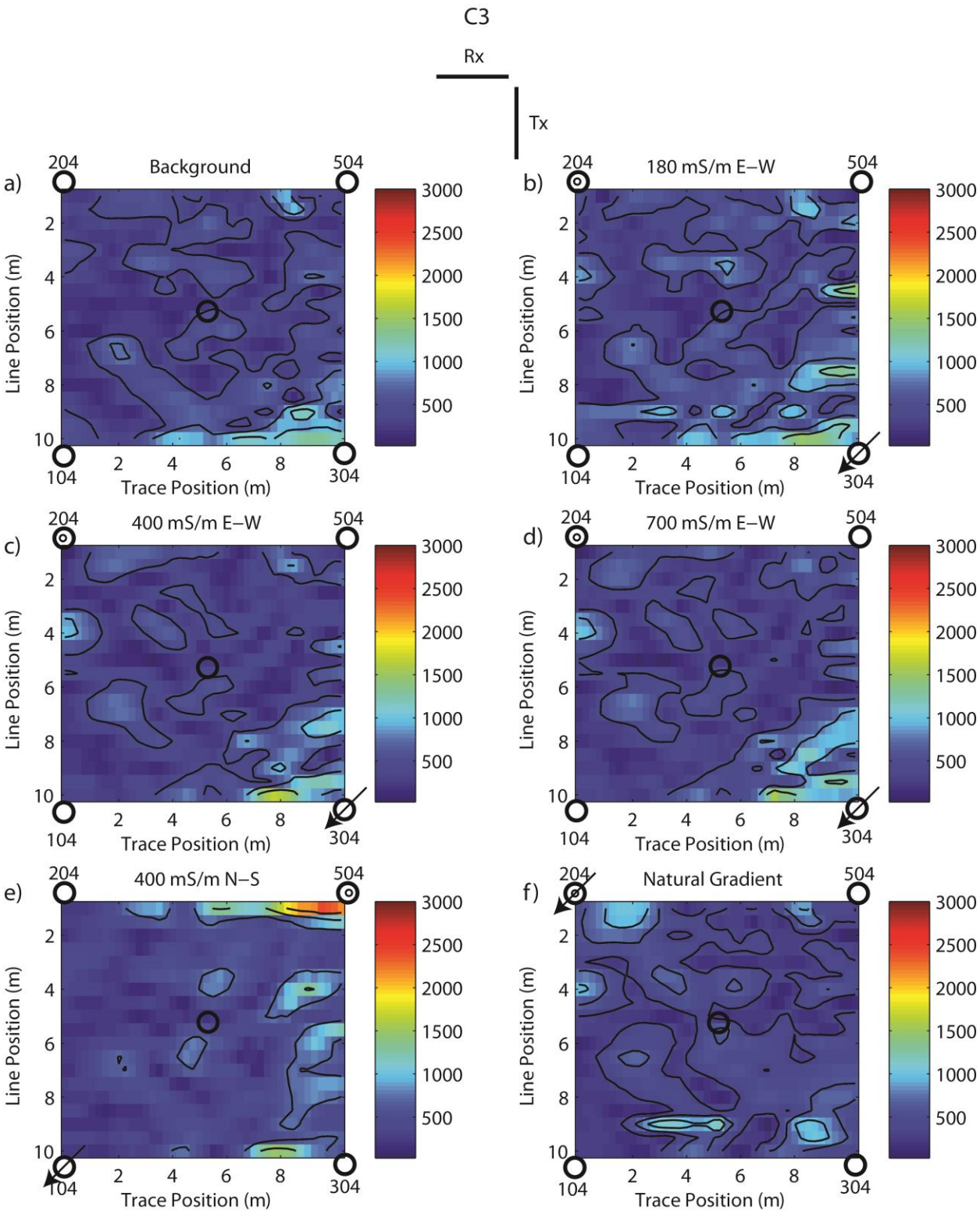

Figure 4.22: 50 MHz C3 raw amplitude maps of fracture. Color signifies amplitude units, contour interval is 500 units. a) Background b) 180 mS/m E-W, c) 400 mS/m E-W, d) 700 mS/m E-W, e) 400 mS/m N-S, f) Natural Gradient.

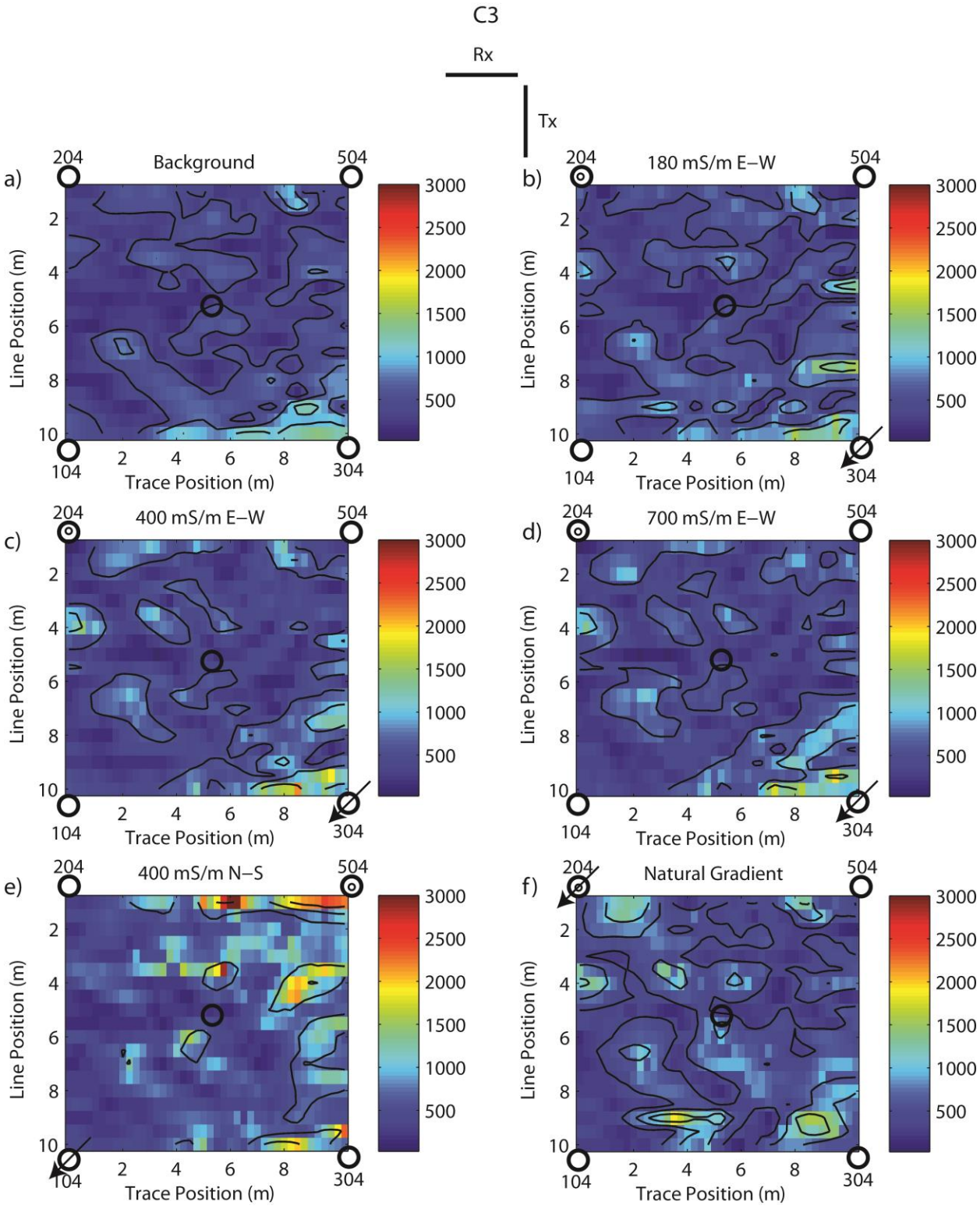

Figure 4.23: 50 MHz C3 scaled-calibrated amplitude maps of fracture. Color signifies amplitude units, contour interval is 500 units. a) Background, b) 180 mS/m E-W, c) 400 mS/m E-W, d) 700 mS/m E-W, e) 400 mS/m N-S, f) Natural Gradient.

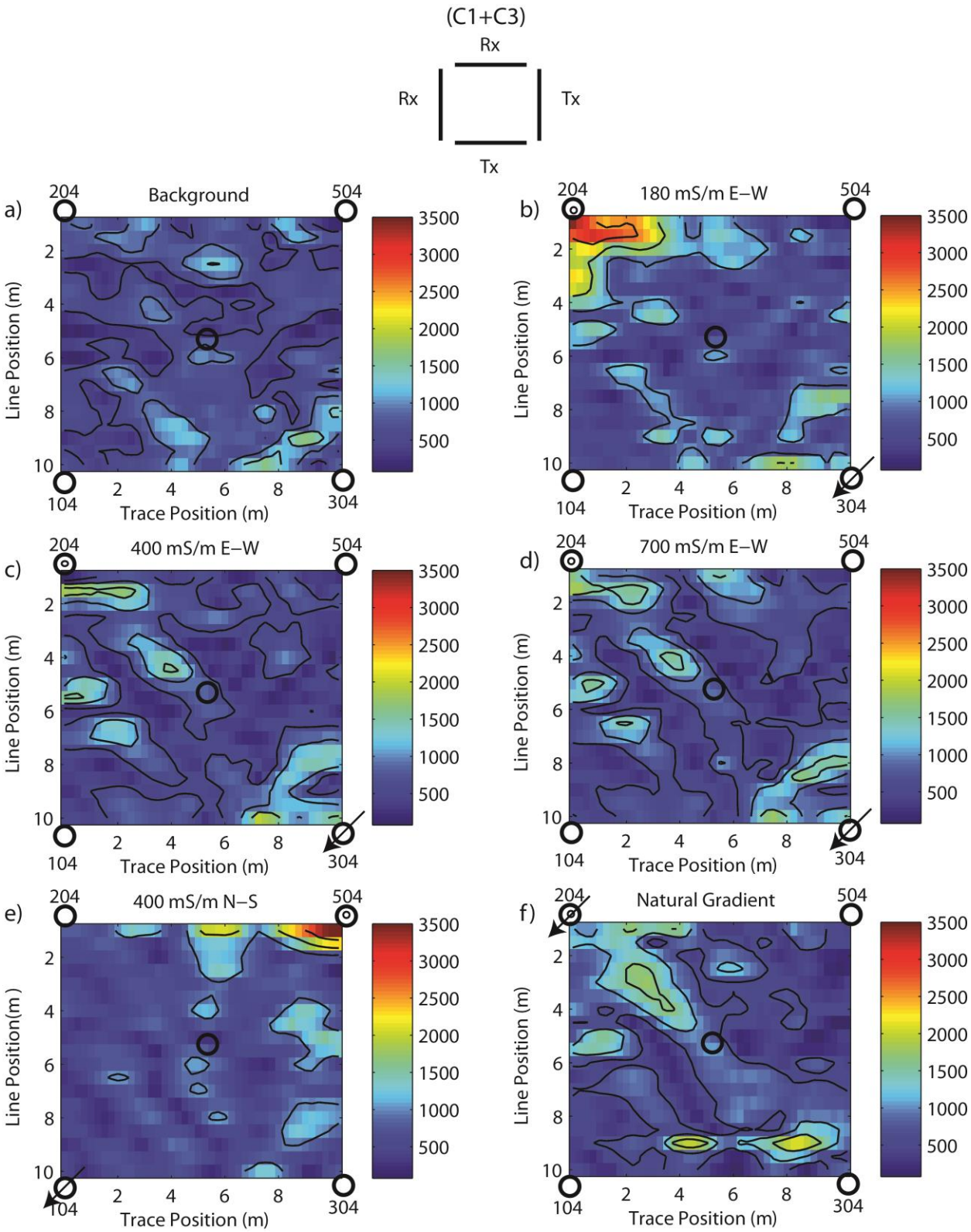

Figure 4.24: 50 MHz **(**C1+C3) raw amplitude maps of fracture. Color signifies amplitude units, contour interval is 500 units. a) Background, b) 180 mS/m E-W, c) 400 mS/m E-W, d) 700 mS/m E-W, e) 400 mS/m N-S, f) Natural Gradient.

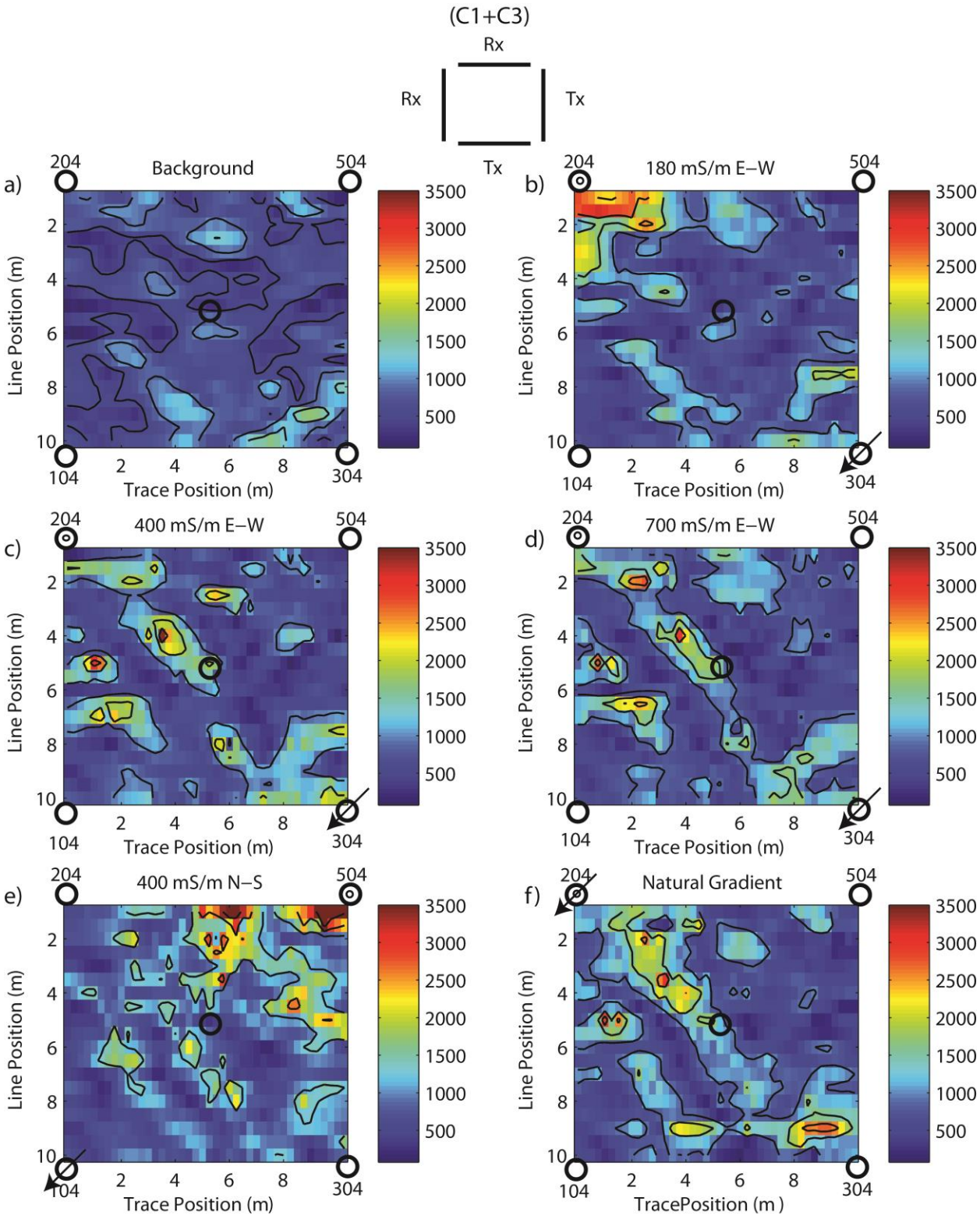

Figure 4.25: 50 MHz **(**C1+C3) scaled-calibrated amplitude maps of fracture. Color signifies amplitude units, contour interval is 500 units. a) Background, b) 180 mS/m E-W, c) 400 mS/m E-W, d) 700 mS/m E-W, e) 400 mS/m N-S, f) Natural Gradient.

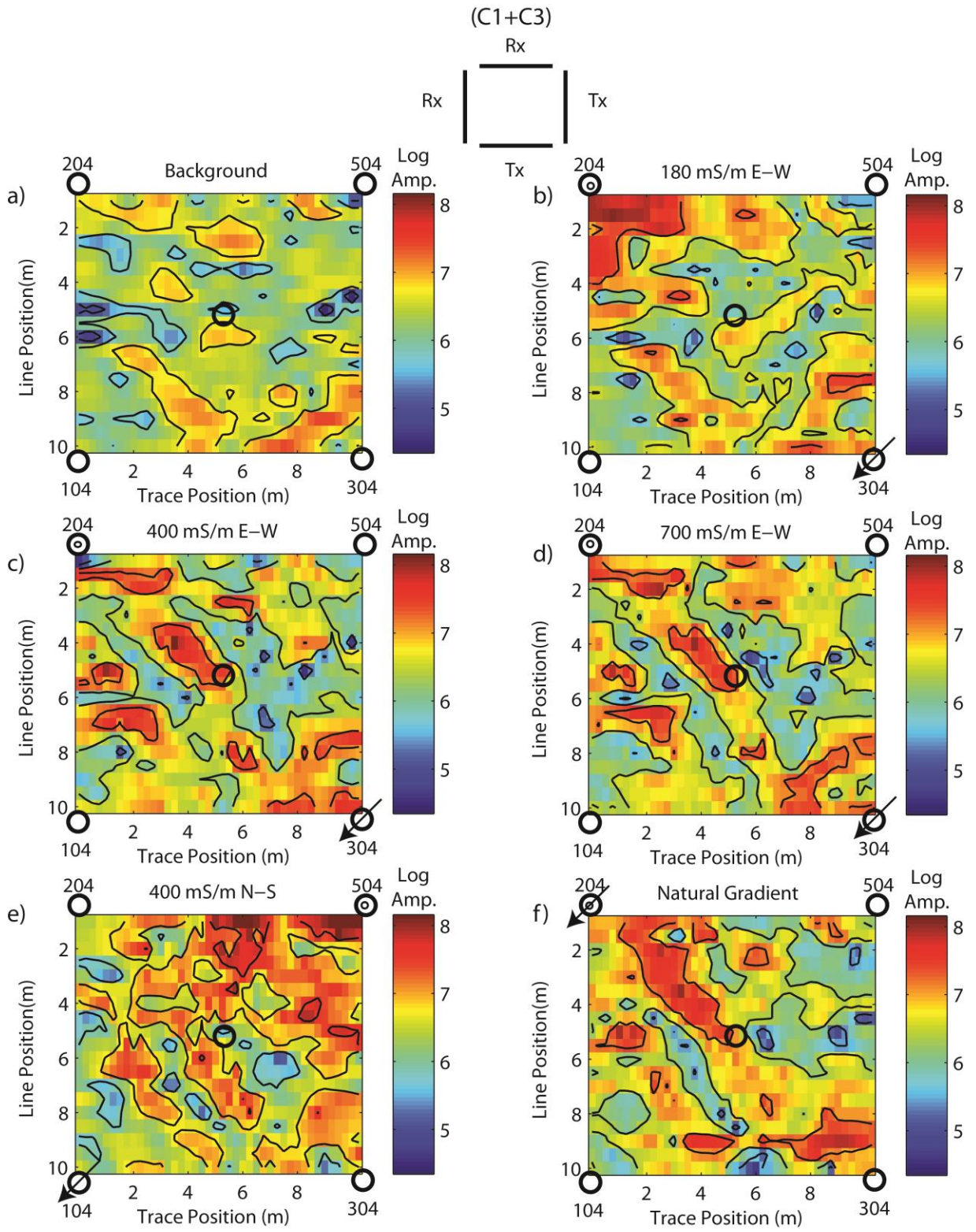

Figure 4.26: 50 MHz **(**C1+C3) scaled-calibrated amplitude maps of fracture. Color signifies natural logarithmic amplitude units, contour interval is 1 unit. a) Background, b) 180 mS/m E-W, c) 400 mS/m E-W, d) 700 mS/m E-W, e) 400 mS/m N-S, f) Natural Gradient.

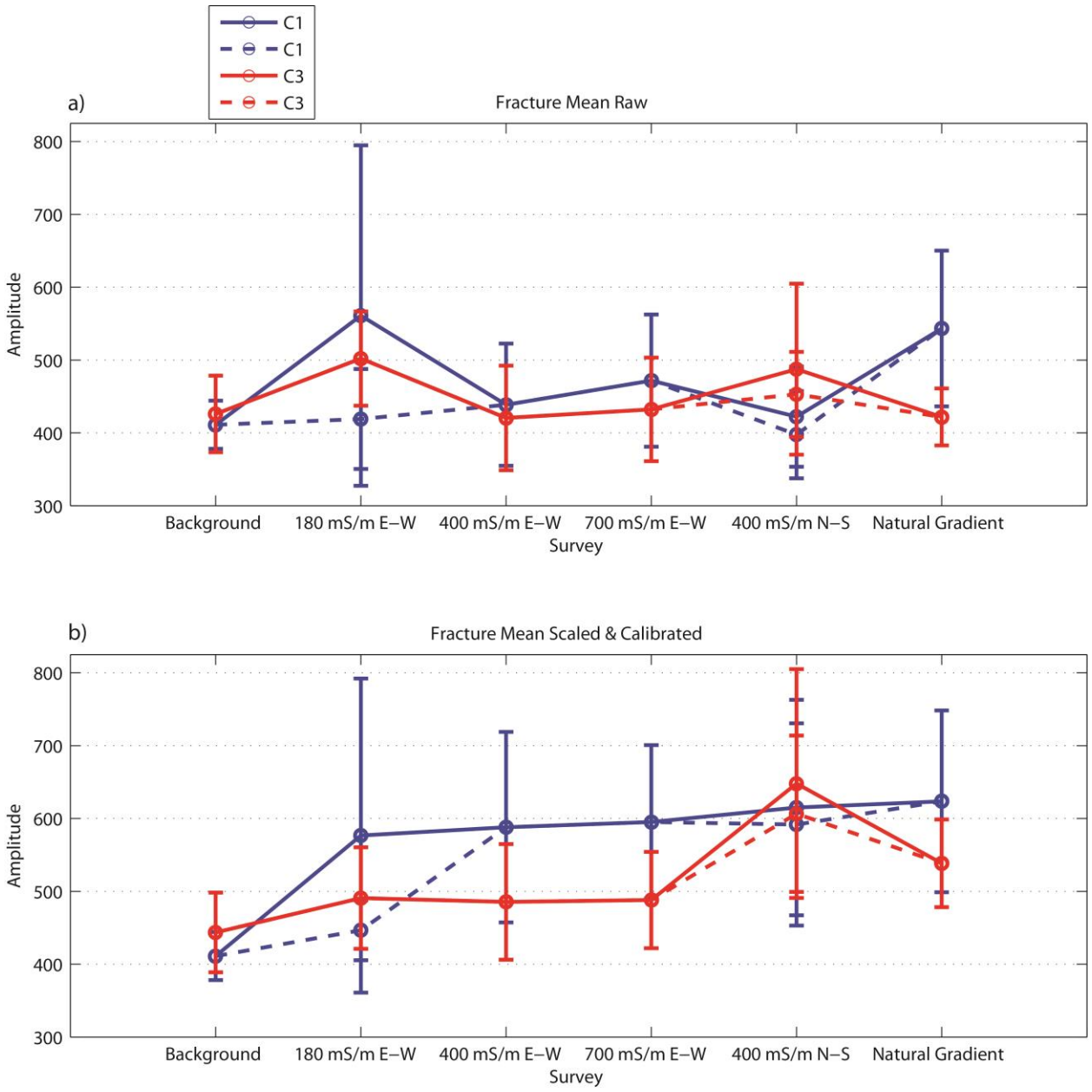

Figure 4.27: Average amplitude of RMS interval across 50 MHz fracture plotted for each survey and individual polarizations C1 and C3. Dashed lines have removed high amplitude values in the 180 mS/m E-W and 400 mS/m N-S surveys. a) Raw, b) Scaled-calibrated.

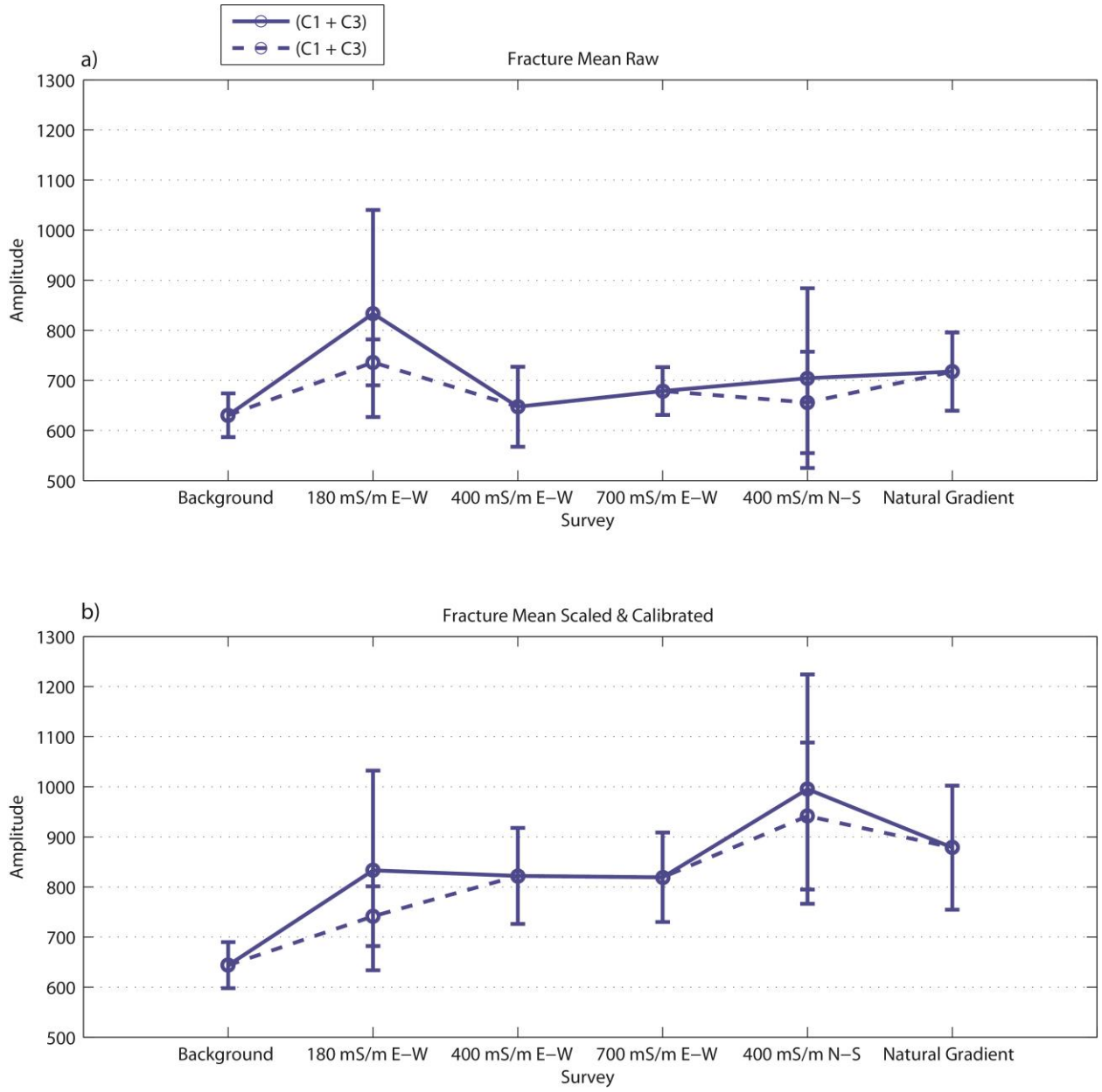

Figure 4.28: Average amplitude of RMS interval across 50 MHz fracture plotted for sums (C1+C3) for each survey. Dashed lines have removed high amplitude values in the 180 mS/m E-W and 400 mS/m N-S surveys. a) Raw, b) Scaled-calibrated.

4.2.3 100 MHz GPR Surveys

100 MHz cross-polarized raw and scaled-calibrated amplitude maps of fracture are shown in Figures 4.29-4.34. 100 MHz amplitude maps are significantly weaker, approximately one order of magnitude less, than 50 MHz amplitude maps. C1 and C3 raw and scaled-calibrated maps show no amplitude trends between wells, and tracer test amplitudes are close to the Background survey in strength (Figures 4.29-4.32). Both C1 and C3 400 mS/m N-S surveys show higher amplitudes than other surveys (Figure 4.29e-4.32e). The (C1+C3) amplitude maps do not show amplitude trends, but the 400 mS/m N-S map displays higher amplitudes than other surveys (Figure 3.33-3.35). The lack of amplitude trends between wells suggests that 100 MHz cross-polarized signals are not able to detect the channel.

Plots of the average amplitude for each survey were generated to analyze the effect of increasing saline tracer. Average amplitudes of the RMS interval, plotted with one STD for each survey and polarizations, are shown in Figures 4.36-4.37. The C1 and C3 average amplitude plots shows C3 stronger for all surveys (Figure 4.36). The (C1 +C3) sums show slight increase in amplitude with increased electrical conductivity (Figure 4.37). The 400 mS/m N-S survey average amplitude is significantly stronger than other surveys (Figures 4.36-4.37). The 100 MHz data is less sensitive to increasing electrical conductivity than the 50 MHz (Tsoflias and Becker, 2008). This observation is in agreement with numerical models presented in chapter 3 (Figure 3.9).

4.2.4 100 MHz GPR Surveys Summary

1. 100 MHz amplitude maps are weaker than 50 MHz and show no consistent amplitude trends.
2. The 400 ms/m N-S dipole exhibits overall greater amplitudes than other surveys.

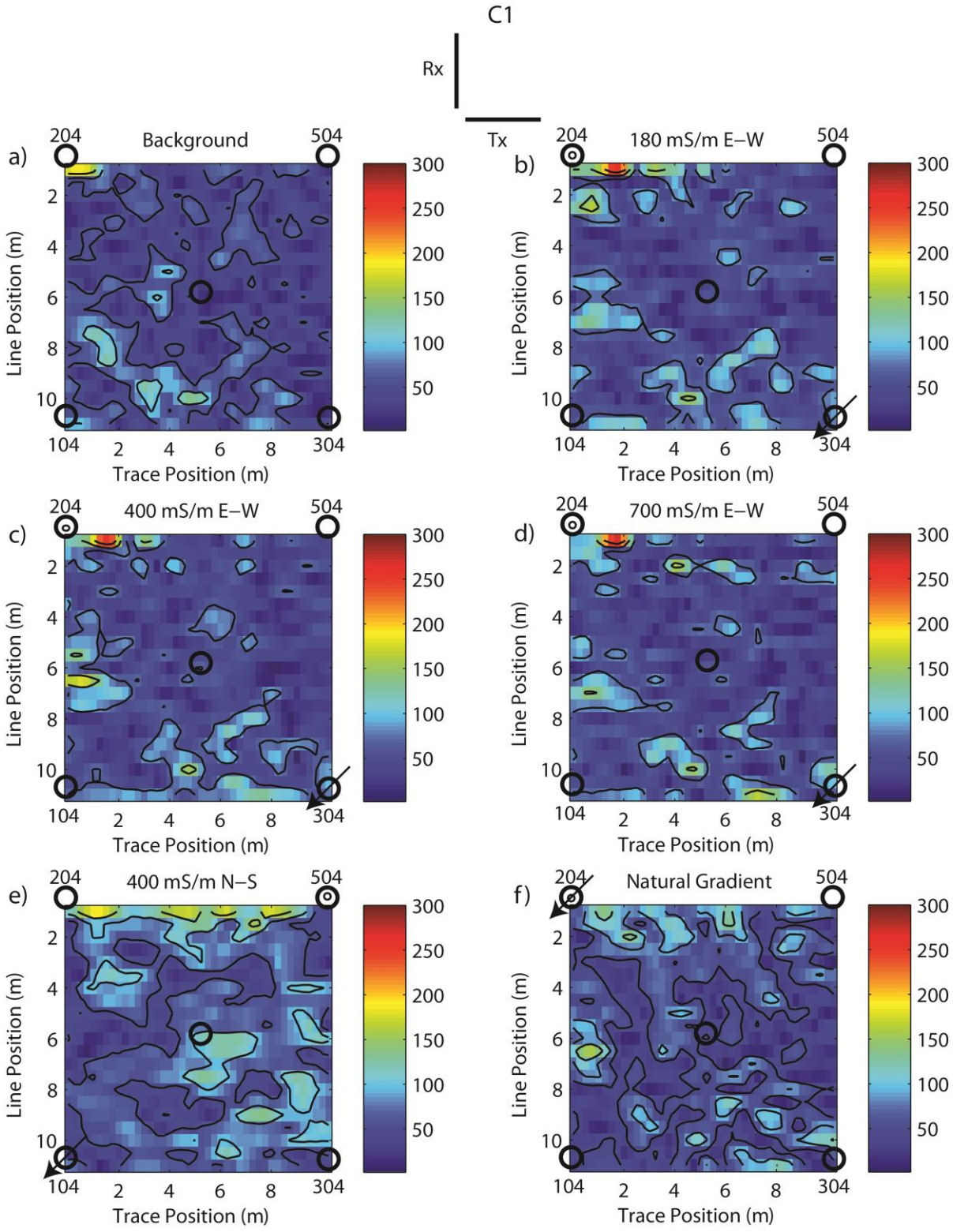

Figure 4.29: 100 MHz C1 raw amplitude maps of fracture. Color signifies amplitude units, contour interval is 50 units. a) Background, b) 180 mS/m E-W, c) 400 mS/m E-W, d) 700 mS/m E-W, e) 400 mS/m N-S, f) Natural Gradient.

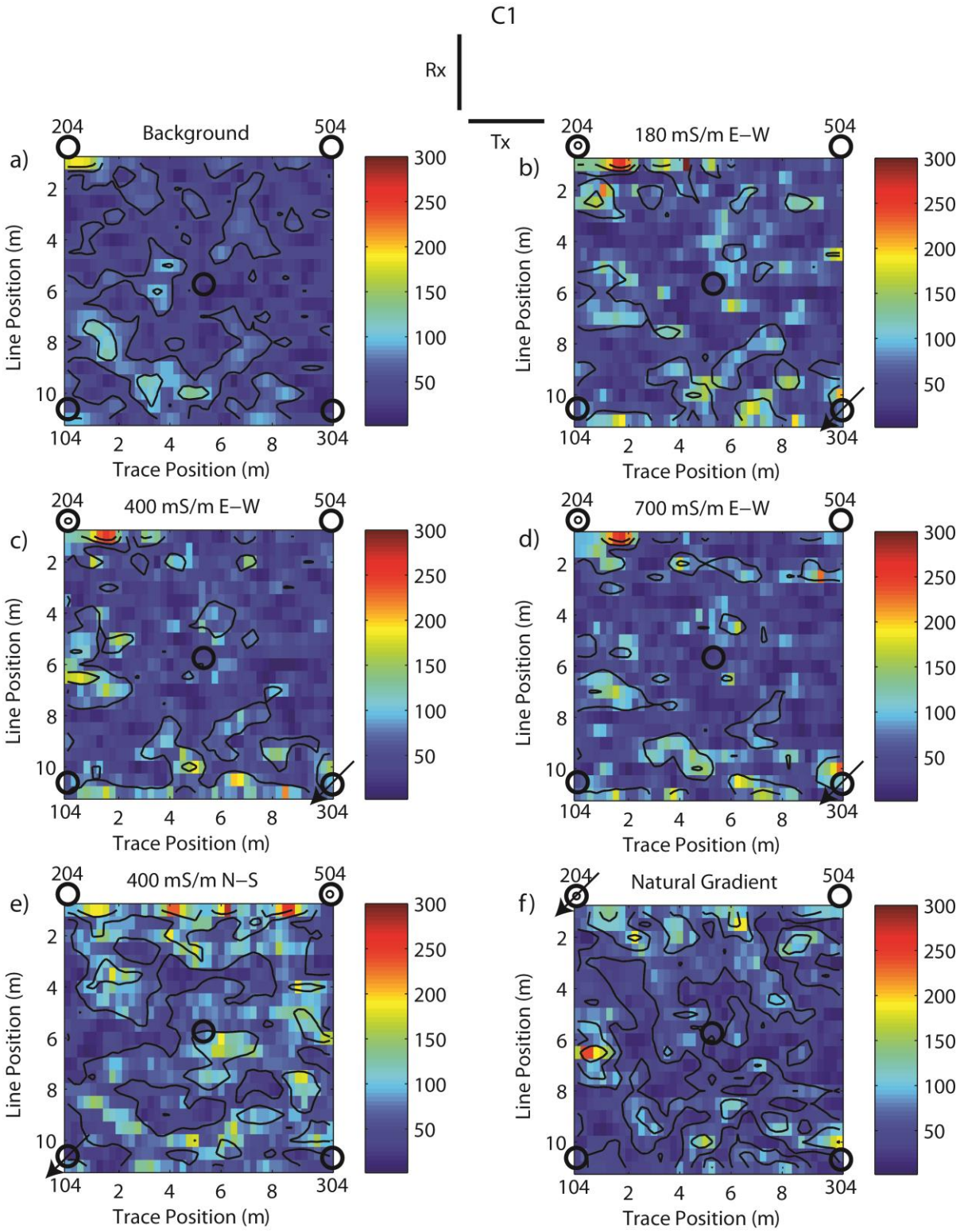

Figure 4.30: 100 MHz C1 scaled-calibrated amplitude maps of fracture. Color signifies amplitude units, contour interval is 50 units. a) Background, b) 180 mS/m E-W, c) 400 mS/m E-W, d) 700 mS/m E-W, e) 400 mS/m N-S, f) Natural Gradient.

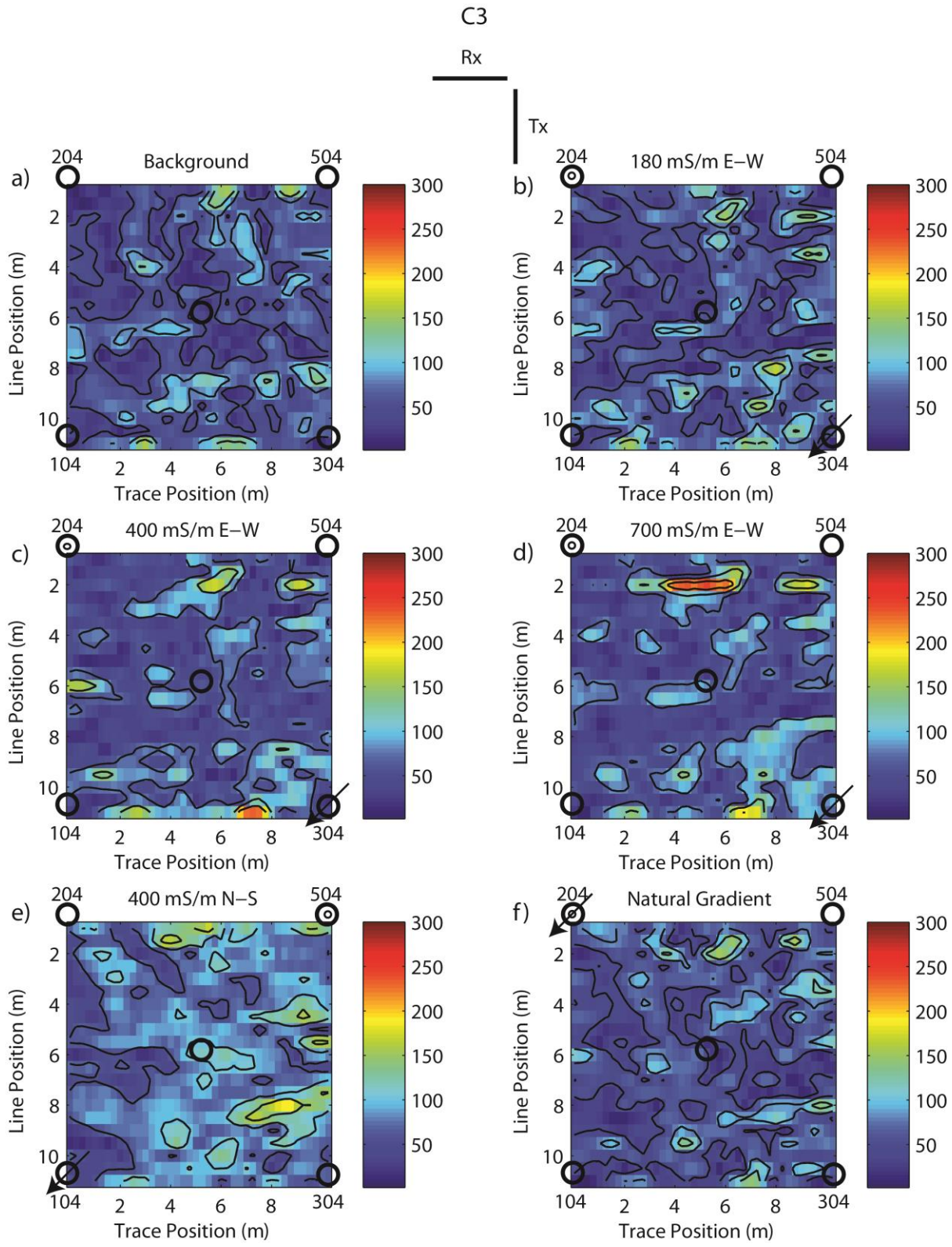

Figure 4.31: 100 MHz C3 raw amplitude maps of fracture. Color signifies amplitude units, contour interval is 50 units. a) Background, b) 180 mS/m E-W, c) 400 mS/m E-W, d) 700 mS/m E-W, e) 400 mS/m N-S, f) Natural Gradient.

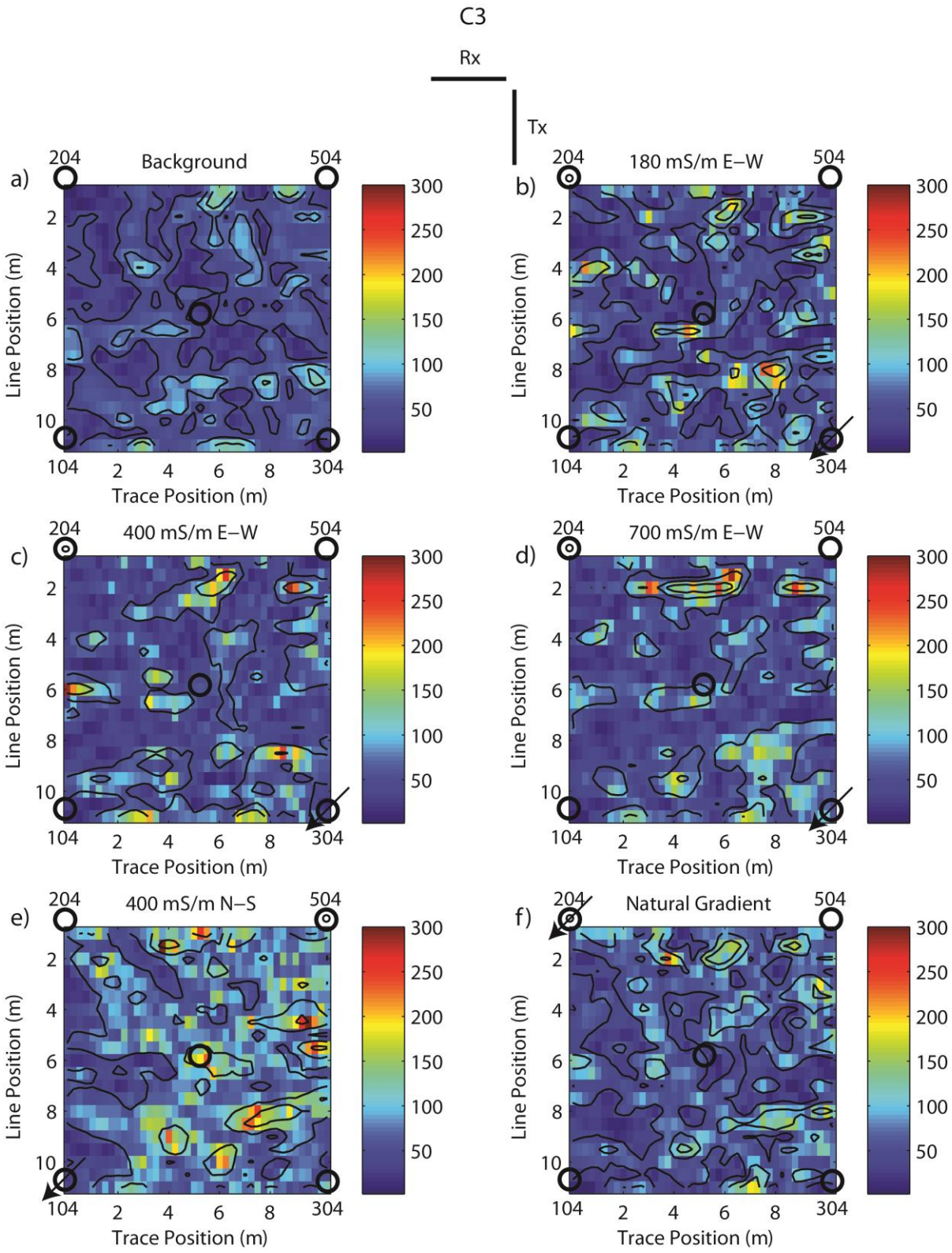

Figure 4.32: 100 MHz C3 scaled-calibrated amplitude maps of fracture. Color signifies amplitude units, contour interval is 50 units. a) Background, b) 180 mS/m E-W, c) 400 mS/m E-W, d) 700 mS/m E-W, e) 400 mS/m N-S, f) Natural Gradient.

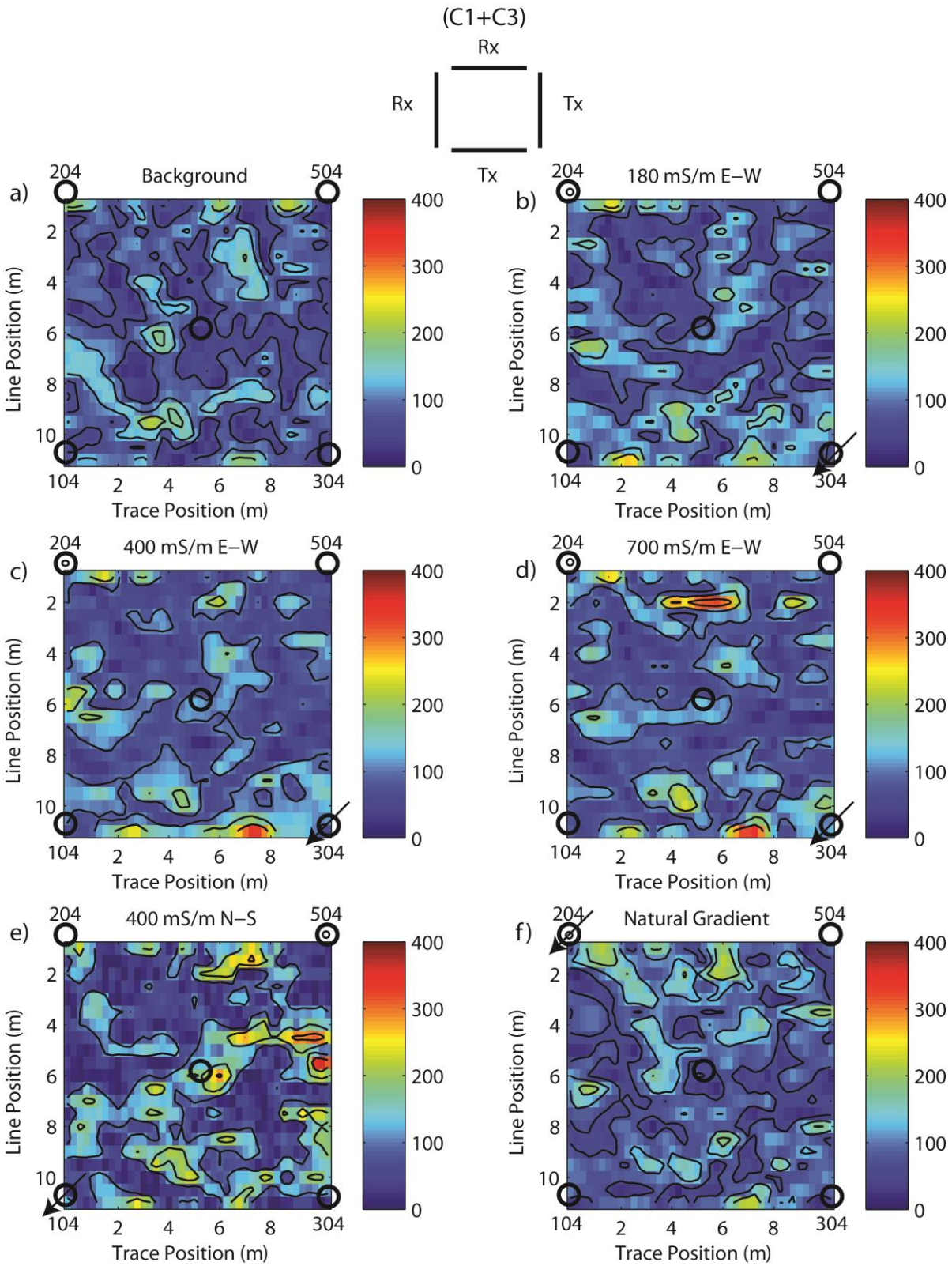

Figure 4.33: 100 MHz (C1+C3) raw amplitude maps of fracture. Color signifies amplitude units, contour interval is 50 units. a) Background, b) 180 mS/m E-W, c) 400 mS/m E-W, d) 700 mS/m E-W, e) 400 mS/m N-S, f) Natural Gradient.

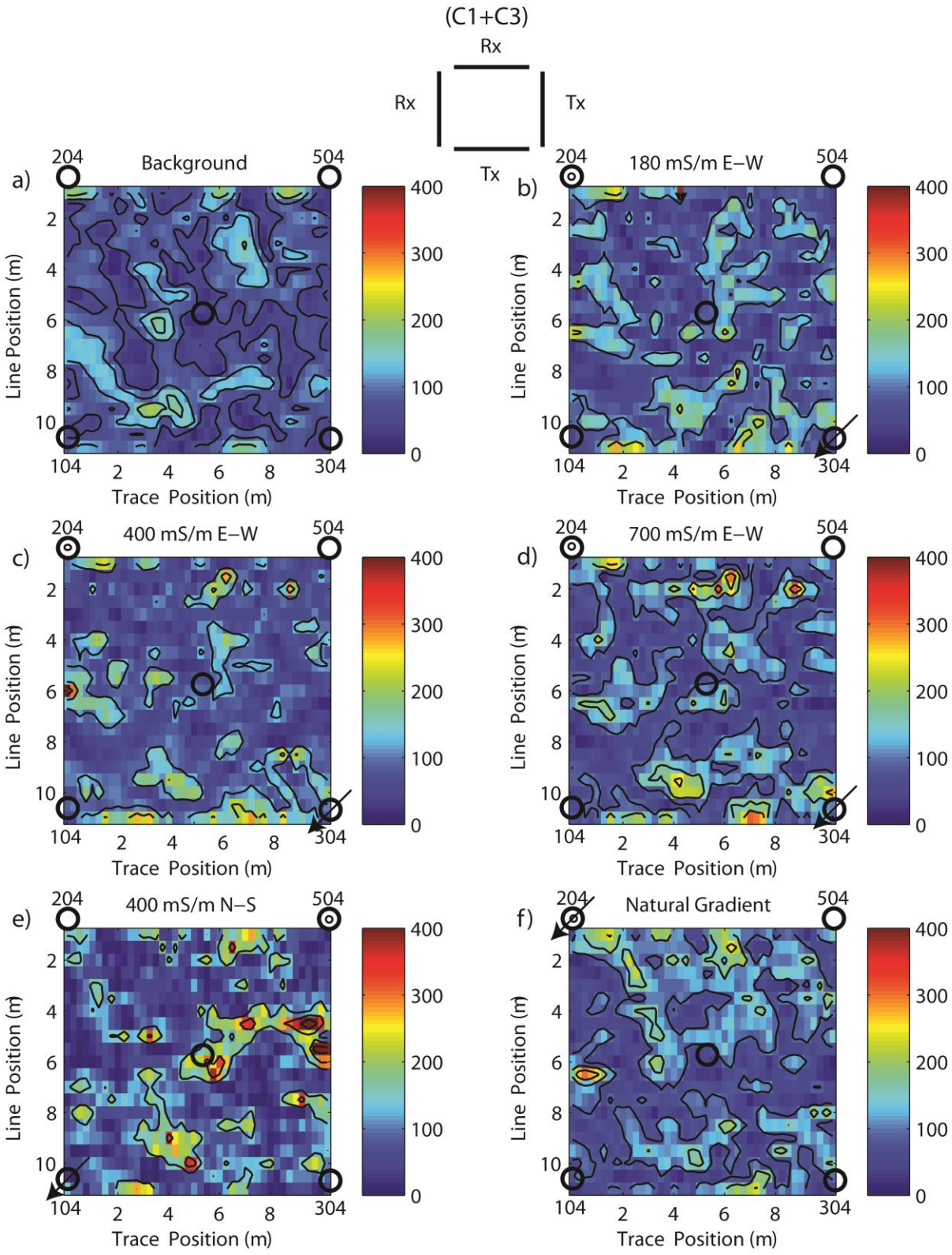

Figure 4.34: 100 MHz **(**C1+C3) scaled-calibrated amplitude maps of fracture. Color signifies amplitude units, contour interval is 50 units. a) Background, b) 180 mS/m E-W, c) 400 mS/m E-W, d) 700 mS/m E-W, e) 400 mS/m N-S, f) Natural Gradient.

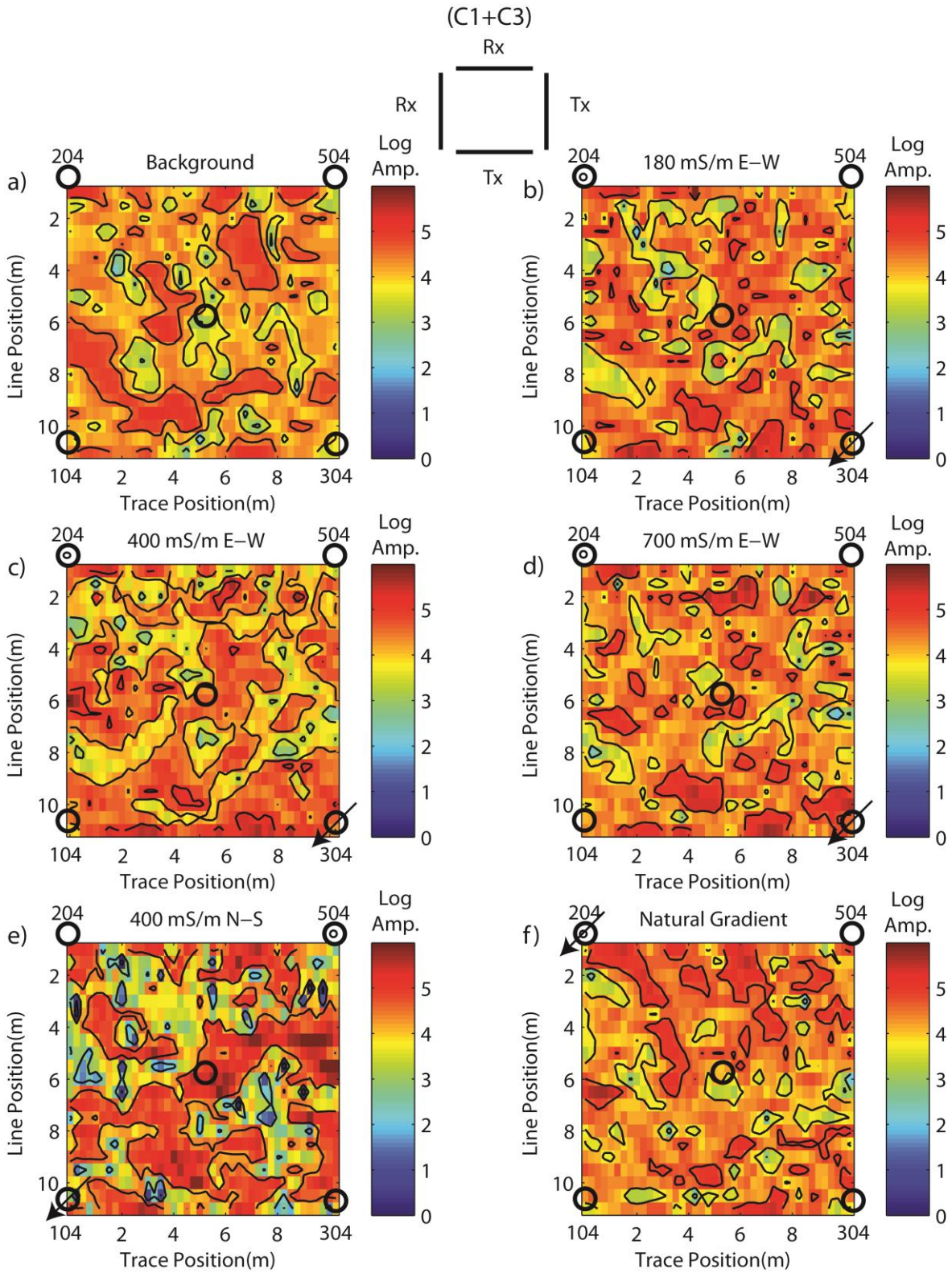

Figure 4.35: 100 MHz **(**C1+C3) scaled-calibrated amplitude maps of fracture. Color signifies natural logarithmic amplitude units, contour interval is 1 unit. a) Background, b) 180 mS/m E-W, c) 400 mS/m E-W, d) 700 mS/m E-W, e) 400 mS/m N-S, f) Natural Gradient.

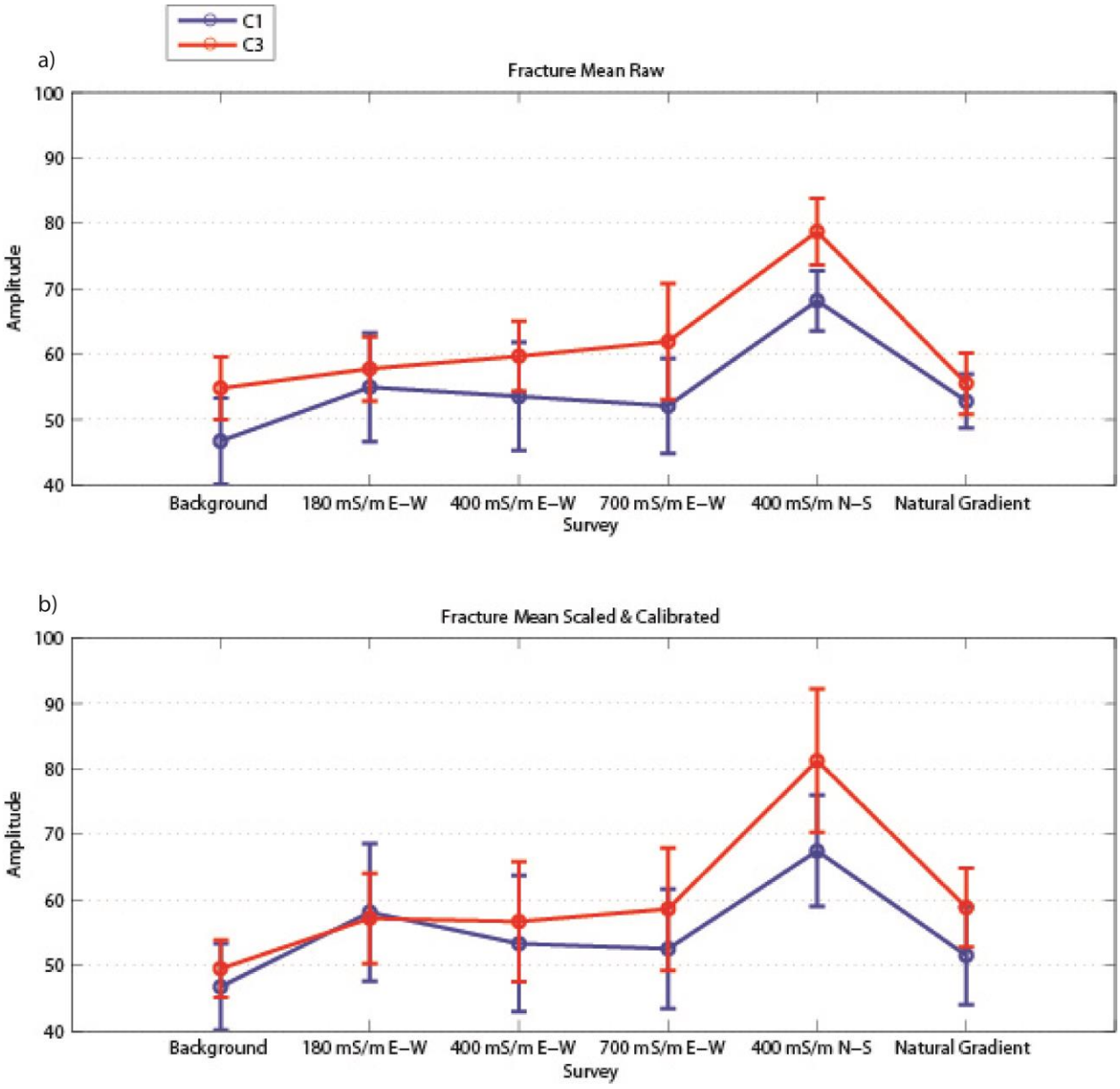

Figure 4.36: Average amplitude of RMS interval across 100 MHz fracture plotted for each survey and individual polarizations C1 and C3. a) Raw, b) Scaled-calibrated.

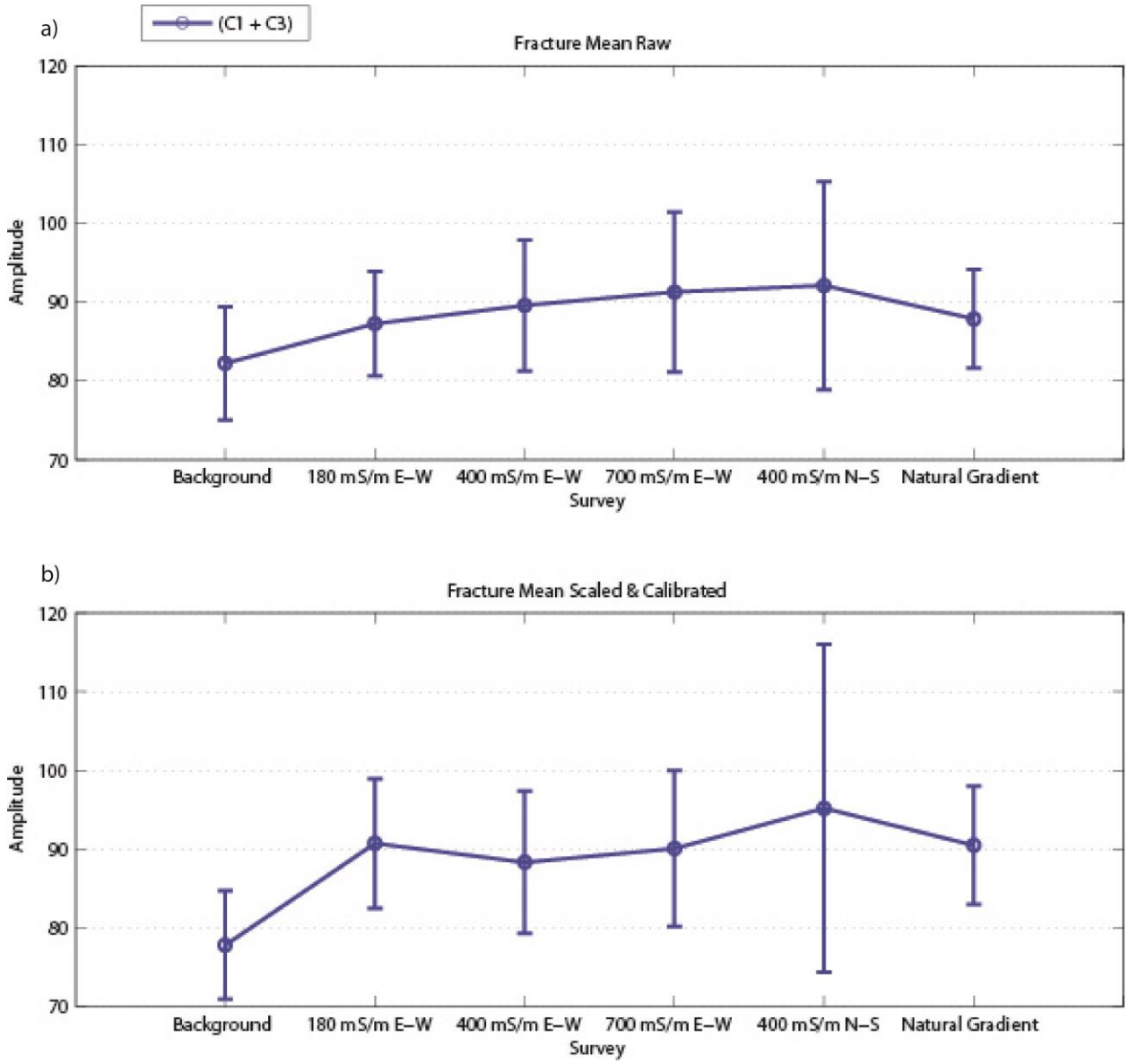

Figure 4.37: Average amplitude of RMS interval across 100 MHz fracture plotted for sums (C1+C3) for each survey. a) Raw, b) Scaled-calibrated.

4.2.5 50 MHz Small-Dipole GPR Surveys

50 MHz Small-Dipole, cross-polarized raw and scaled-calibrated amplitude maps of the fracture are shown in Figures 4.38-4.44. The C1 raw data shows large amplitudes near pumping wells 204 and 504 (Figure 4.38). The C1 scaled-calibrated data shows a coherent amplitude trend from wells 204 to 404 and well 304 to 404 suggesting good connectivity but a weaker trend between 104 to 404 and 504 to 404 (Figure 4.39) suggesting poor conductivity. The C3 raw data and scaled-calibrated data show large amplitudes near pumping wells 104 and 304 (Figure 4.40-4.41).

Figures 4.42-4.44 show summed (C1+C3) amplitude maps. The raw (C1+C3) amplitude maps also show large amplitude near pumping wells but no amplitude trends between wells (Figure 4.42). Scaled-calibrated (C1+C3) data show an amplitude trend between well 204 to 404 and 304 to 404 suggesting good connectivity along 204,404, and 304 E-W (Figure 4.43cf). The natural logarithmic scale (Figure 4.43cf) also show an amplitude trend from 204 to 404 and 304 to 404. A weaker amplitude trend is seen from well 104 to 304 and 504 to 404 suggesting poor connectivity (Figures 4.43-4.44de)

Average amplitude plots are generated for North and South Dipoles to analyze the effect of the saline tracer. The average amplitude of the RMS interval plotted with one STD for each survey and polarization are shown in Figures 4.45-4.46. The North-Dipoles average amplitude plot shows C1 is stronger than C3 for all surveys in both raw and scaled-calibrated data (Figure 4.45). The South Dipole average amplitude plot shows C1 stronger for Small-Dipole 104-404 and C3 stronger in Small-Dipole 304-404 (Figure 4.46). The sums (C1+C3) average amplitude plot shows Small-Dipole 104-404 and 504-404 have the highest amplitudes and the largest STD (Figure 4.46). High amplitude values near pumping wells may be caused by interference from

metallic pump. Therefore, averages were also calculated without these high amplitudes and are shown by dashed lines in figure 4.46.

4.2.6 50 MHz Small-Dipole GPR Surveys Summary

1. Weak evidence of a flow channel reflection in individual polarizations becomes more apparent after calibration and scaling.
2. Summed responses (C1+C3) show evidence that wells 204 and 304 are well connected and wells 104 and 504 are poorly connected hydrologically. This is in agreement with the results from the 50 MHz full grids.
3. Increasing water electrical conductivity increases the reflected amplitude of fracture.
4. Amplitude trends are in agreement with the full sized 50 MHz grids presented in section 4.2.1.

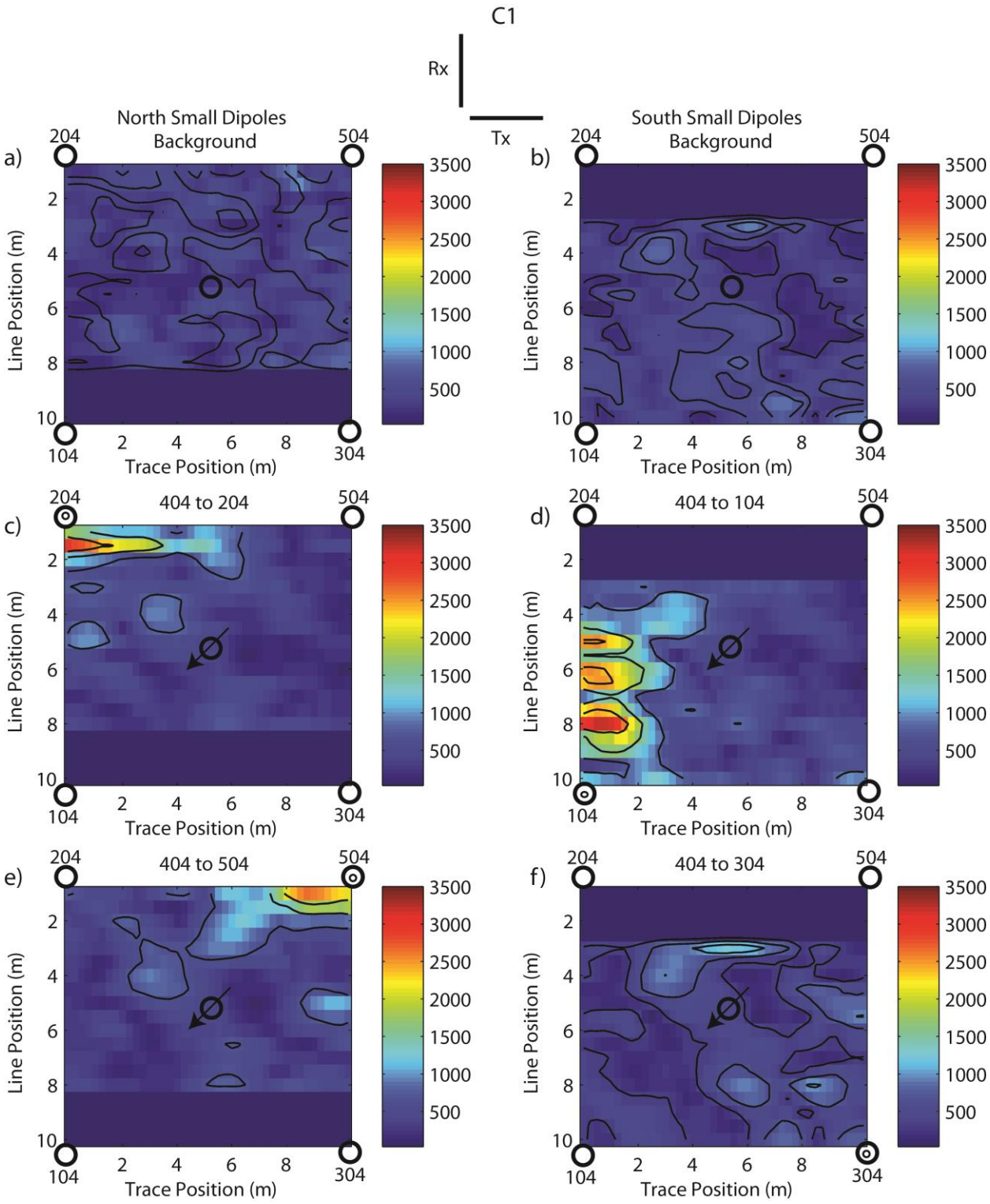

Figure 4.38: 50 MHz small-dipoles C1 raw amplitude maps of fracture. Color signifies amplitude units, contour interval is 500 units. (Left) North Dipoles (Right) South Dipoles a) North Background, b) South Background, c) 404-204, d) 404-104, e) 404-504, f) 404-304.

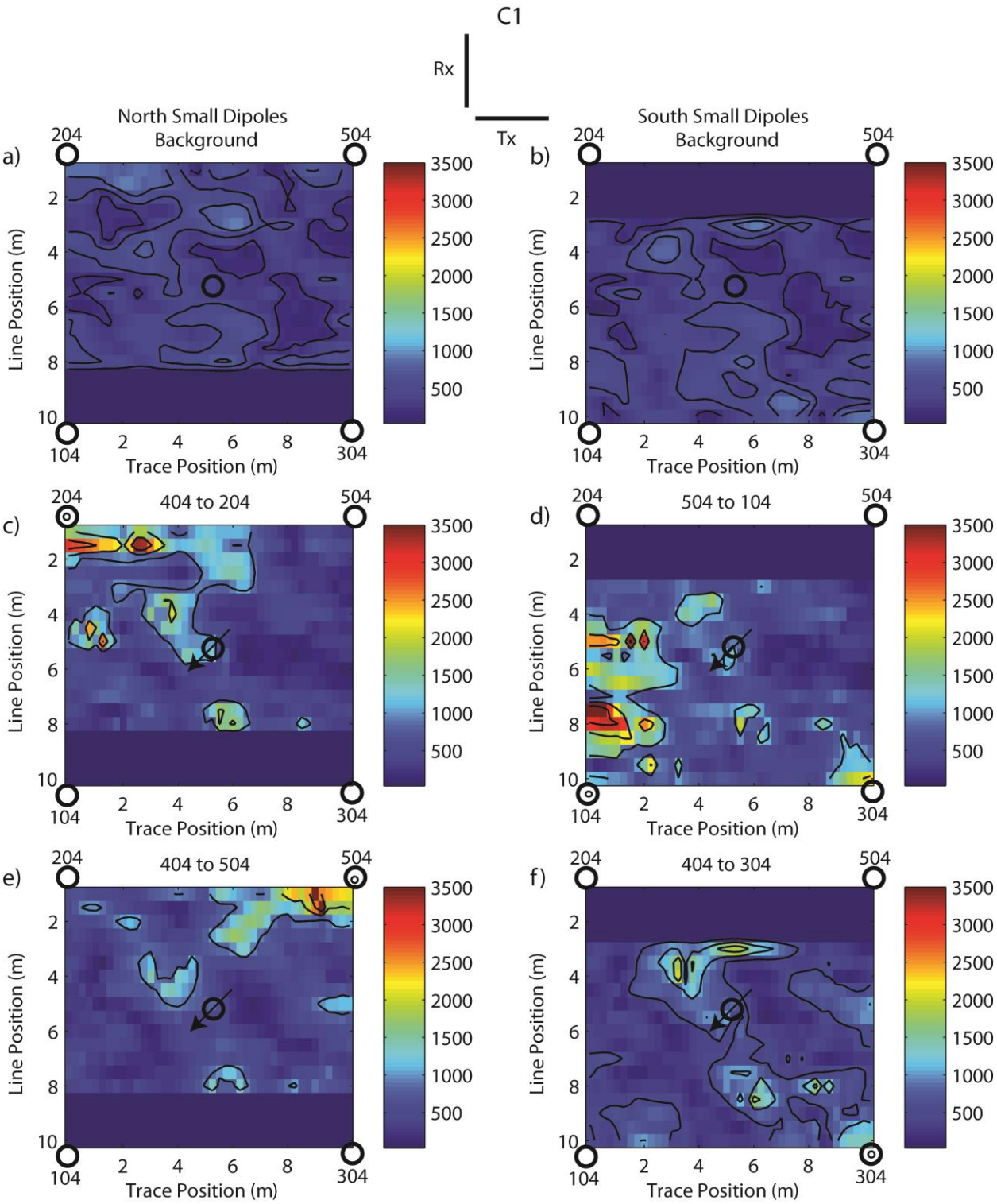

Figure 4.39: 50 MHz small-dipoles C1 scaled-calibrated amplitude maps of fracture. Color signifies amplitude units, contour interval is 500 units. (Left) North Dipoles (Right) South Dipoles a) North Background, b) South Background, c) 404-204, d) 404-104, e) 404-504, f) 404-304.

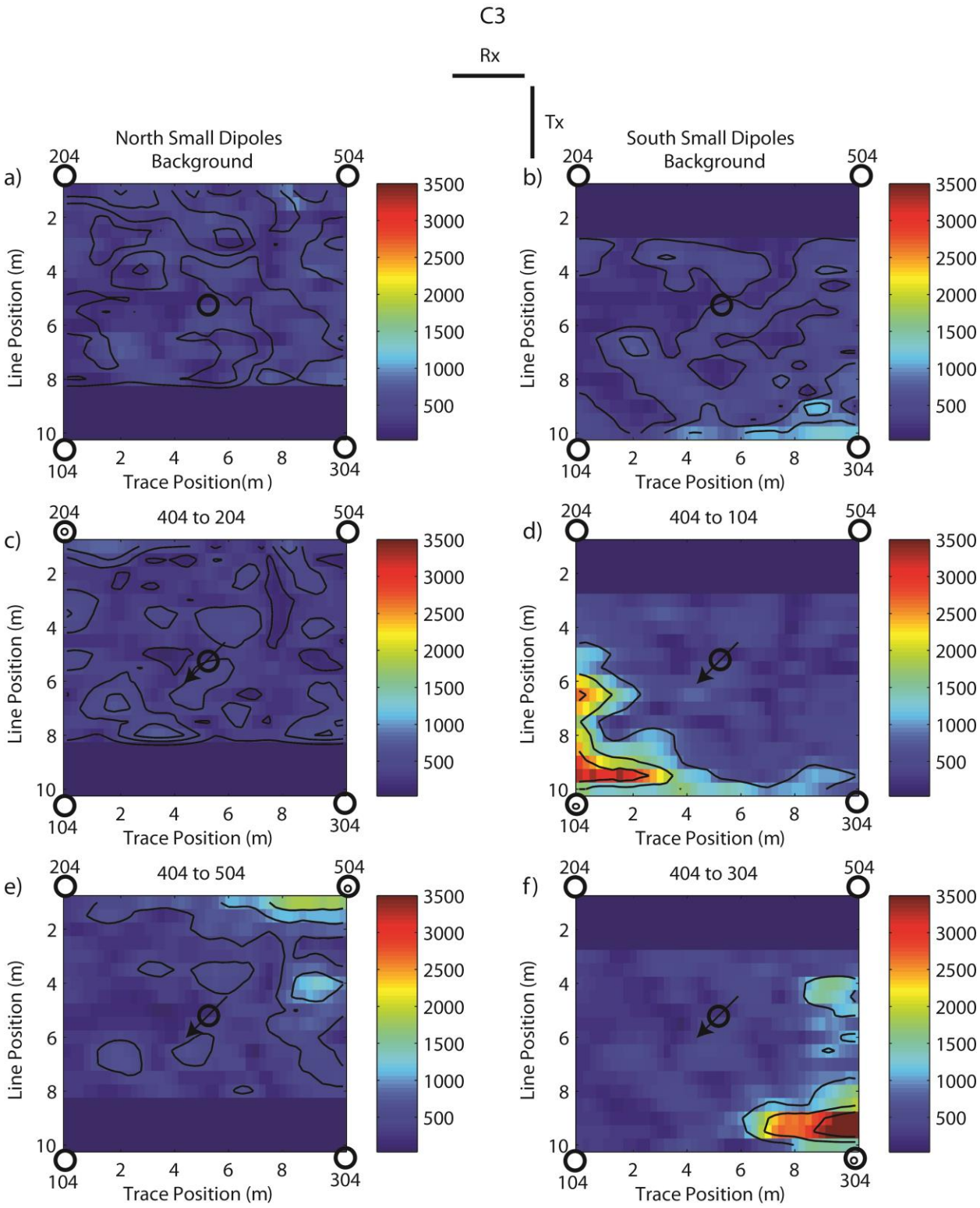

Figure 4.40: 50 MHz small-dipoles C3 raw amplitude maps of fracture. Color signifies amplitude units, contour interval is 500 units. (Left) North Dipoles (Right) South Dipoles a) North Background, b) South Background, c) 404-204, d) 404-104, e) 404-504, f) 404-304.

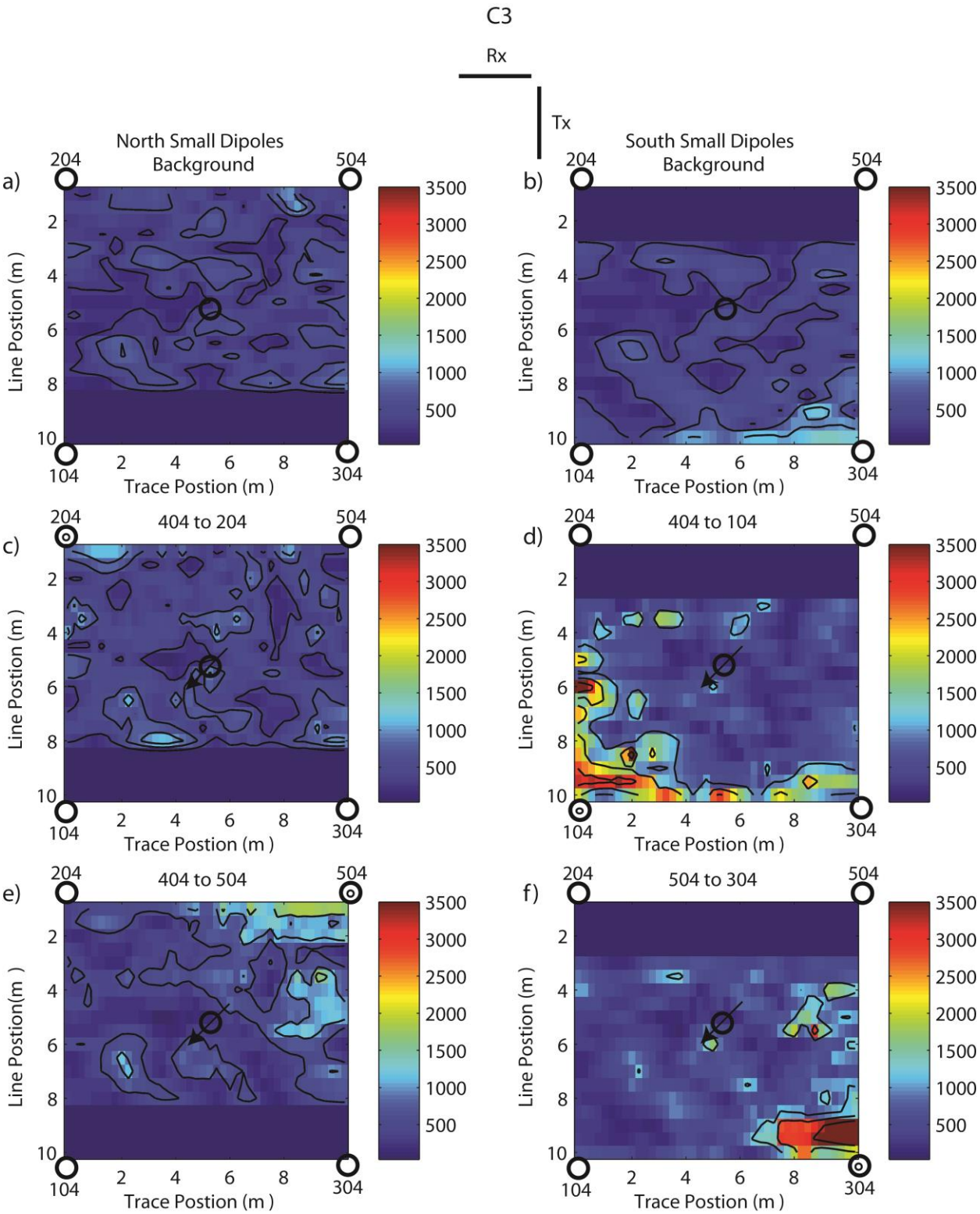

Figure 4.41: 50 MHz small-dipoles C3 scaled-calibrated amplitude maps of fracture. Color signifies amplitude units, contour interval is 500 units. (Left) North Dipoles (Right) South Dipoles a) North Background, b) South Background, c) 404-204, d) 404-104, e) 404-504, f) 404-304.

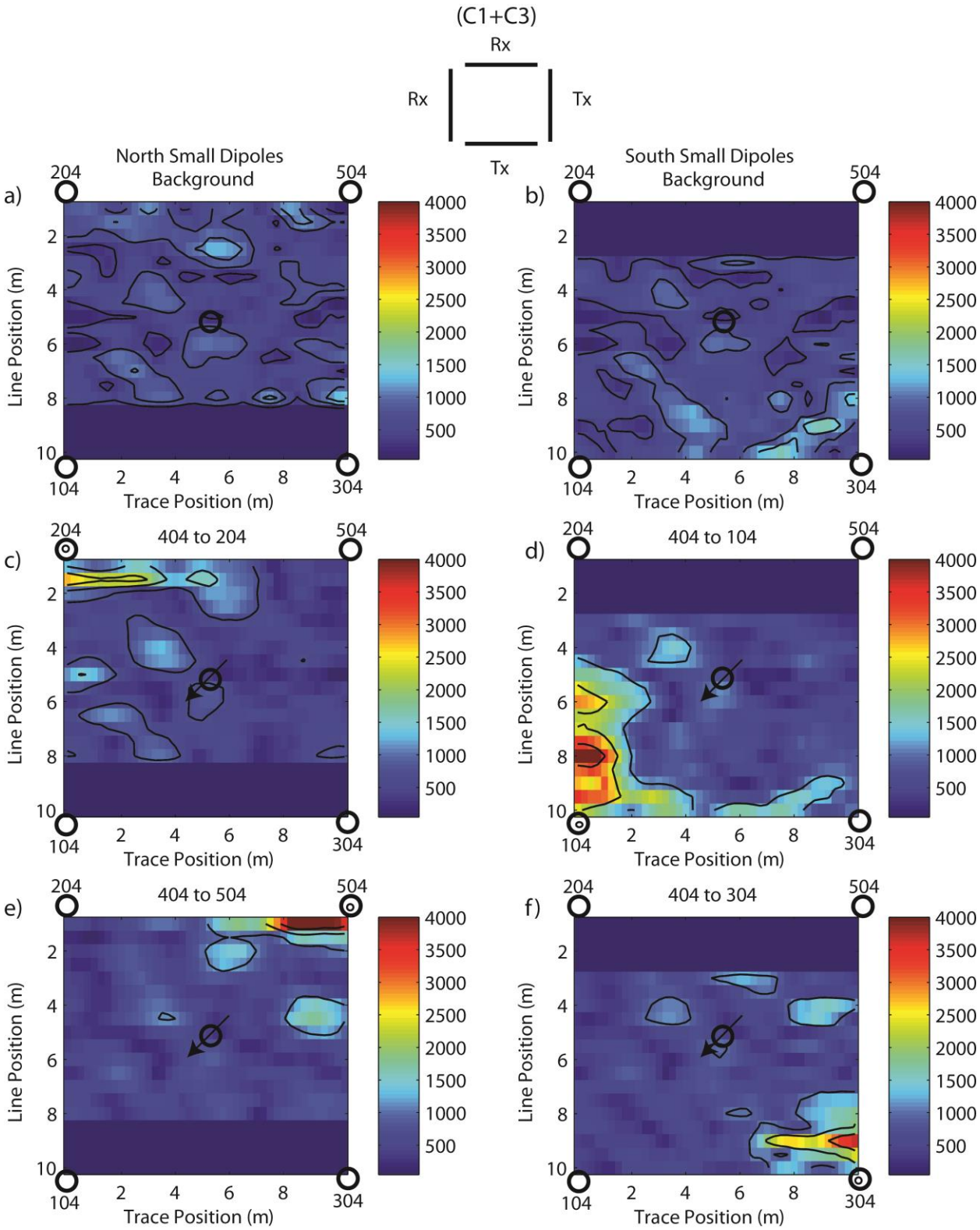

Figure 4.42: 50 MHz small-dipoles (C1+C3) raw amplitude maps of fracture. Color signifies amplitude units, contour interval is 500 units. (Left) North Dipoles (Right) South Dipoles a) North Background, b) South Background, c) 404-204, d) 404-104, e) 404-504, f) 404-304.

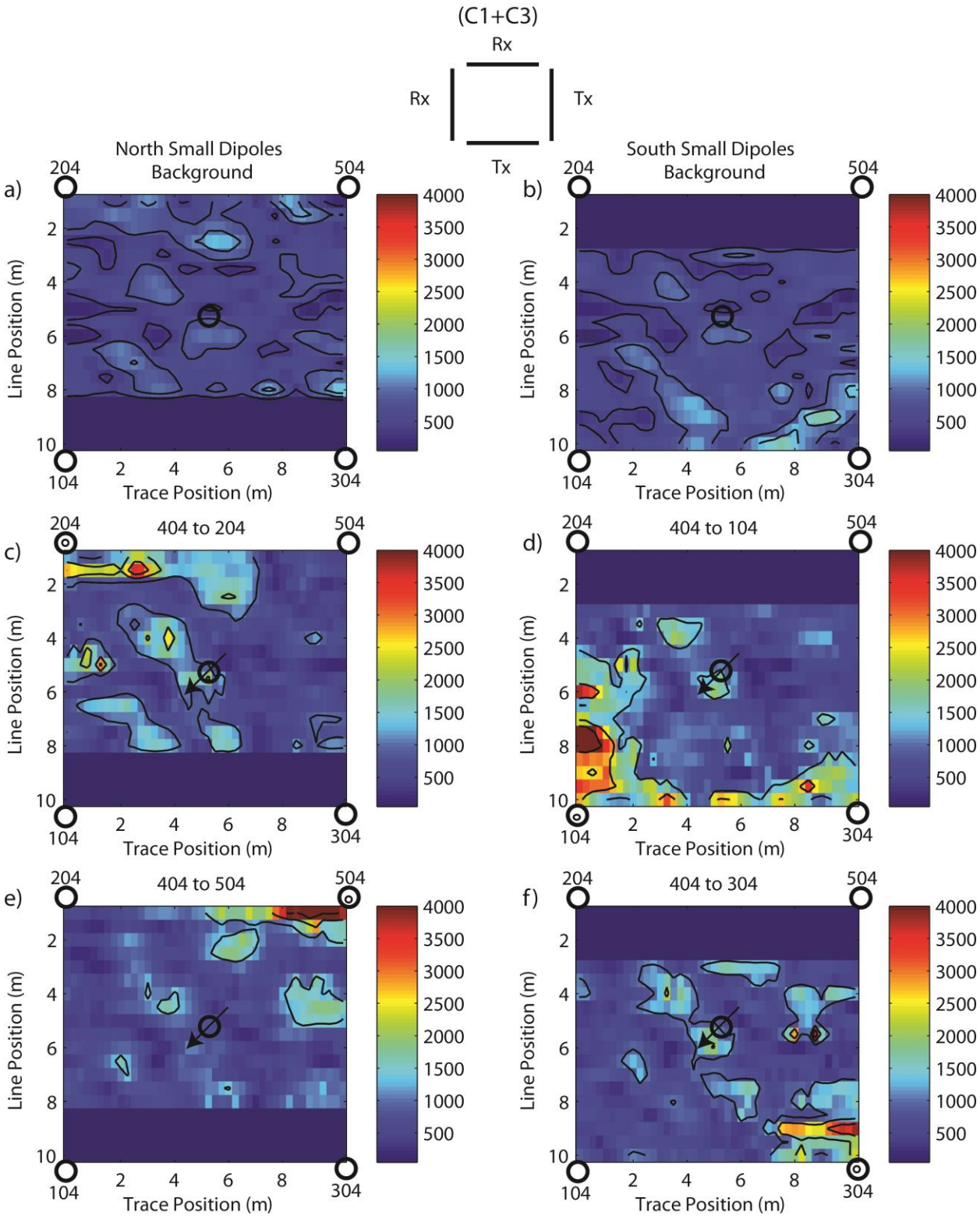

Figure 4.43: 50 MHz small-dipoles (C1+C3) scaled-calibrated amplitude maps of fracture. Color signifies amplitude units, contour interval is 500 units. (Left) North Dipoles (Right) South Dipoles a) North Background, b) South Background, c) 404-204, d) 404-104, e) 404-504, f) 404-304.

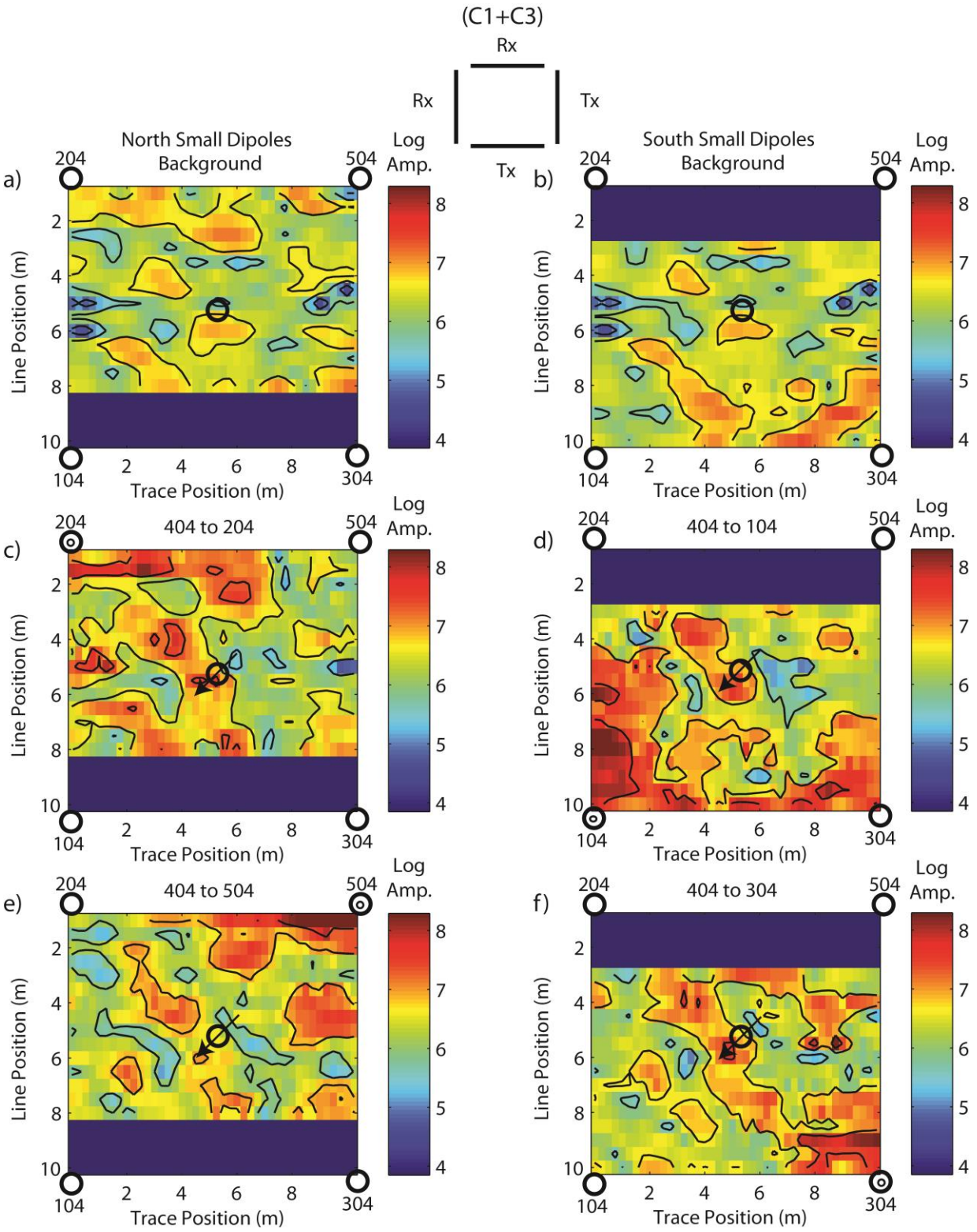

Figure 4.44: 50 small-dipoles MHz **(**C1+C3) scaled-calibrated amplitude maps of fracture. Color signifies natural logarithmic amplitude units, contour interval is 1 unit. a) Background, b) 180 mS/m E-W, c) 400 mS/m E-W, d) 700 mS/m E-W, e) 400 mS/m N-S, f) Natural Gradient.

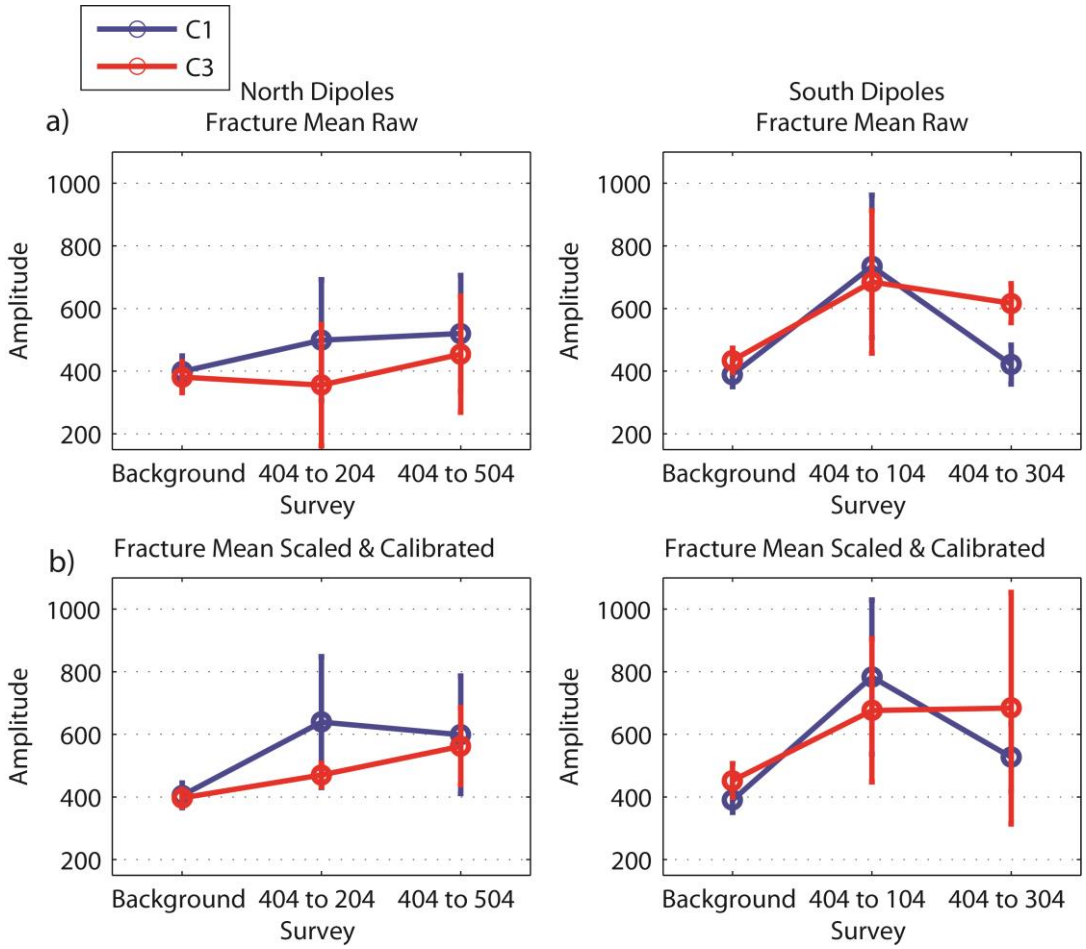

Figure 4.45: Average amplitude of RMS interval for North and South 50 MHz Small-Dipoles plotted for each survey and individual polarizations C1 and C3. (Left) North Dipoles (Right) South Dipoles. a) Raw, b) Scaled-calibrated.

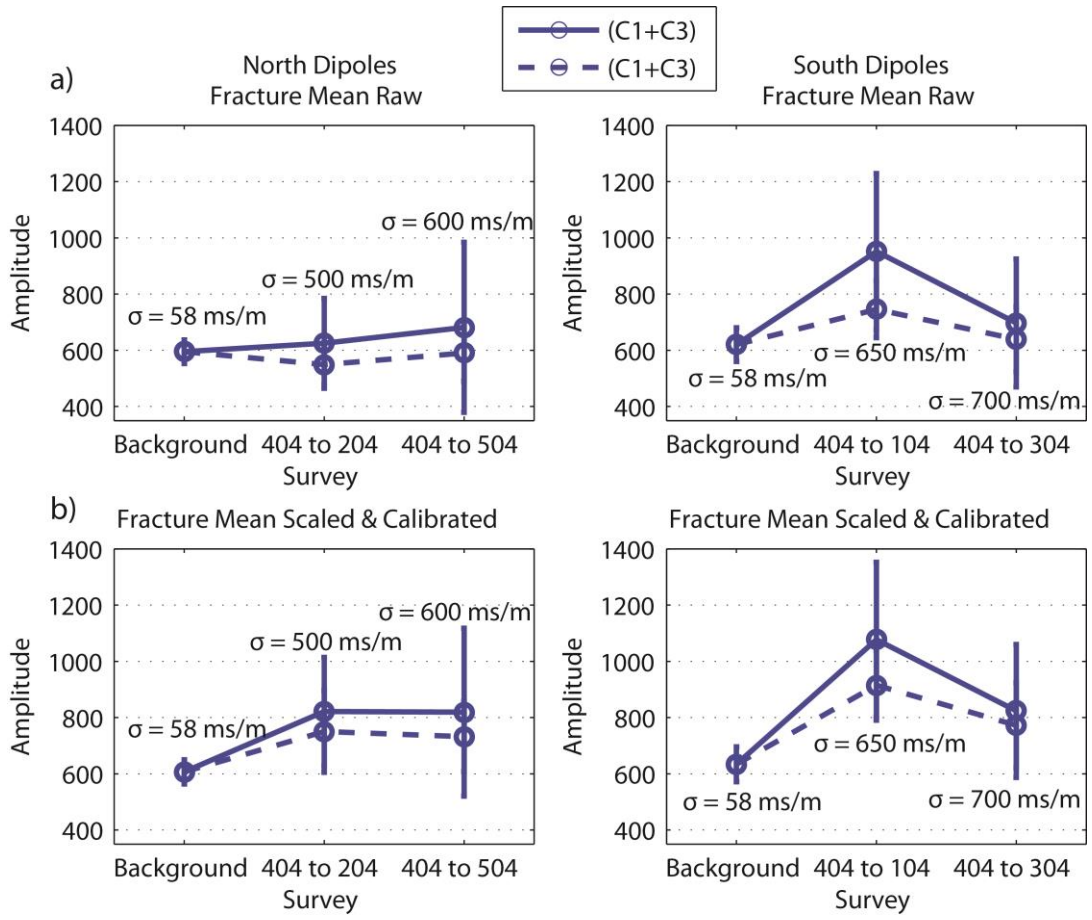

Figure 4.46: Average amplitude of RMS interval for 50 MHz Small-Dipoles plotted for sums (C1+C3) for each survey. (Left) North Dipoles (Right) South Dipoles. a) Raw, b) Scaled-calibrated.

4.2 Altona Tracer Test GPR Discussion

The objective of the Altona field work was to use orthogonal GPR cross-polarized components to image fracture flow channels between wells. To identify flow paths between wells various amounts of saline tracer were injected and dipole flow fields created between different boreholes. The change in water electrical conductivity caused by the saline tracer highlighted flow channels.

50 MHz data showed a difference in amplitude strength between C1 and C3, with C1 stronger than C3. The scaled-calibrated amplitude maps show amplitude trends better than raw data because they compensate for instrument differences and temporal instrument response change. The large amplitude anomaly seen near pumping wells may be caused by the presence of the metallic pump in the borehole. Summing the individual polarizations improved the image of fracture channeling by reducing the polarization effects generated by dipole antennas. 50 MHz sums (C1+C3) identified good connection between wells 204-304 with a flow channel approximately 1.0-1.5 m wide with amplitude trend increasing in strength with increasing electrical conductivity (Figures 4.25-4.26bcdf). No direct flow path was visible in 400 mS/m N-S between wells 104-504 (Figures 4.24-4.26e) but they exhibit the largest overall amplitudes. These observations are corroborated by past hydraulic tests performed at the Altona Flat Rock site (Becker and Guiltinan, 2010). In addition Hawkins and Becker (2012) preformed heat tracer experiments and concluded that wells 204 and 304 are better connected than wells 104 and 504. The average RMS values show increasing amplitude with increasing electrical conductivity (Figure 4.28), which is also in agreement with numerical modeling (Figure 3.15) and past published work (Tsoflias and Becker, 2008). After removing anomalous high amplitudes from

the 180 mS/m E-W and the 400 mS/m N-S data sets the trend of increased amplitude due to increased water electrical conductivity was more apparent.

The 100 MHz data were not able to identify flow paths between the wells in individual polarizations (Figures 4.29-32) or after summing individual polarizations (Figures 4.33-35). The 100 MHz data wavelength (1.0 m) is half the size of the 50 MHz wavelength (2.0 m). The shorter wavelength may not detect the channels that the 50 MHz identified because the channels are too wide and appear as a part of a horizontal plane to 100 MHz signals. Cross-polarized signals do not depolarize from horizontal planar targets (Figure 3.10). Additionally, numerical models in the previous chapter demonstrate that 100 MHz data does not increase in amplitude as much as 50 MHz with increasing water electrical conductivity (Figure 3.15). The 100 MHz amplitude maps show Background survey only marginally weaker than other surveys suggesting that the 100 MHz cross-polarized data does not detecting changes in fracture reflection amplitude caused by saline tracer.

50 MHz Small-Dipoles surveys show similar results to the 50 MHz full surveys. Large amplitude anomalies are seen near pumping wells that could be contributed to metallic pump (Figures 4.38-4.41). The raw individual polarizations show no amplitude trends but after calibration, scaling, and summing trends are visible. The (C1+C3) data show good connection between wells 204 to 404 and 304 to 404 and poor connection between wells 104 to 404 and 504 to 404 (Figures 4.43-4.44). The average RMS values show increasing amplitude due to increasing electrical conductivity (Figure 4.46).

The E-W dipole tracer tests and the natural gradient tests show good connectivity and direct flow paths along the fracture plane. The tracer appears to move rapidly through narrow channels. The N-S dipole tracer tests show radar amplitudes spread over a larger area. This

suggests that the tracer is being forced through a greater surface area of the fracture resulting in the higher overall amplitudes observed in both the 50 and 100 MHz surveys (Figures 4.28, 4.37, and 4.46). These observations suggest that contaminants would rapidly move through the site in an E-W direction, but would by-pass a significant portion of the fracture surface. Contaminants moving N-S would move slowly and cover a larger portion of the fracture surface. If remediation was the objective, an N-S dipole may be preferable because it would result in sweeping a larger area of the fracture.

The field data provided evidence that useful information can be extracted from the cross-polarized components. By summing two orthogonal cross-polarized components an accurate image of fracture channel was produced.

Chapter 5: Conclusions and Future Work

A horizontal fracture containing a channel was simulated with FDTD numerical modeling to assess the effect of fracture aperture, water electrical conductivity, and polarization on the reflected energy from the fracture. In addition multipolarization GPR surveys where completed in conjunction with saline tracer tests at the Altona Flat Rock site to identify flow channels between wells. The objective of this study was to evaluate polarization response with the numerical models and identify a method to image the fracture at the filed site with the cross-polarized components.

Numerical modeling verified that the cross-polarized data held useful information but only when the channel is oriented oblique to the survey line. When the channel is oriented oblique to the survey line, summation of the cross-polarized and co-polarized components result in an accurate representation of the total scattered energy of the channel. When the channel is oriented parallel or orthogonal to the survey line there is no cross-polarized component and the summation of the co-polarized components represents the total scattered energy. Additionally, models demonstrated that after subtraction of the horizontal fracture the co-polarized components were similar to the cross-polarized components.

A method was developed that used the zero crossing time picks above and below the fracture in the co-polarized components to track changes in the cross-polarized components. The zero crossing time picks where transferred to corresponding cross-polarized components and the RMS of the interval was calculated. The resulting amplitude maps show good connectivity between wells 204 and 304 with an approximately 1.0 – 1.5 m wide flow channel visible in E-W tracer tests. Wells 104 and 504 are not well connected with no visible flow path between the two

wells. These results agree with past published work associated with the Altona Flat Rock site (Becker and Guiltinan, 2005; and Hawkins and Becker 2012).

This study represents the first known investigation of the polarization properties of GPR in order to image channelized flow in a horizontal fracture. Additional, work that incorporates both the co-polarized and the cross-polarized components into one data set that fully captures scattered energy from fracture is needed. Separate or joint inversion of co-polarized and cross-polarized components holds promise for quantifying fracture aperture and saline tracer concentration.

References

Balanis, C. A., 1989, Advanced engineering electromagnetics, John Wiley & Sons.

Becker, M. W., and Guiltinan, E., 2010, Cross-hole periodic hydraulic testing of inter-well connectivity, *in* Proceedings Thirty-Fifth Workshop on Geothermal Reservoir Engineering.

Birken, R., and Versteeg, R., 2000, Use of four-dimensional ground penetrating radar and advanced visualization methods to determine subsurface fluid migration: Journal of Applied Geophysics, v. 43, no. 2, p. 215-226.

Chen, C. C., Higgins, M. B., O'Neill, K., and Detsch, R., 2001, Ultrawide-bandwidth fully-polarimetric ground penetrating radar classification of subsurface unexploded ordnance: Geoscience and Remote Sensing, IEEE Transactions on, v. 39, no. 6, p. 1221-1230.

Davis, J., and Annan, A., 1989, Ground penetrating radar for high resolution mapping of soil and rock stratigraphy: Geophysical prospecting, v. 37, no. 5, p. 531-551.

Day-Lewis, F. D., Lane, J. W., Harris, J. M., and Gorelick, S. M., 2003, Time-lapse imaging of saline-tracer transport in fractured rock using difference-attenuation radar tomography: Water Resour. Res., v. 39, no. 10.

Dorn, C., Linde, N., Le Borgne, T., Bour, O., and Baron, L., 2011, Single-hole GPR reflection imaging of solute transport in a granitic aquifer: Geophysical Research Letters, v. 38, no. 8.

Dorn, C., Linde, N., Le Borgne, T., Bour, O., and Klepikova, M., 2012, Inferring transport characteristics in a fractured rock aquifer by combining single-hole ground-penetrating radar reflection monitoring and tracer test data: Water Resources Research, v. 48, no. 11.

Giannopoulos, A., 2005, Modelling ground penetrating radar by GprMax: Construction and Building Materials, v. 19, no. 10, p. 755-762.

Giannopouls, A., 2005, User's Manual Version 2.0 GPRMAX.

Grasmueck, M., 1996, 3-D ground-penetrating radar applied to fracture imaging in gneiss: Geophysics, v. 61, p. 1050.

Grasmueck, M., Weger, R., and Horstmeyer, H., 2004, Three-dimensional ground-penetrating radar imaging of sedimentary structures, fractures, and archaeological features at submeter resolution.(Author Abstract): Geology, v. 32, no. 11, p. 933.

Grasmueck, M., 2005, Full-resolution 3D GPR imaging: Geophysics, v. 70, p. K12.

Hawkins, A. J., and Becker, M. W., 2012, Measurement of the Spatial Distribution of Heat Exchange in a Geothermal Analog Bedrock Site Using Fiber Optic Distributed Temperature Sensing, *in* Proceedings Thirty-Seventh Workshop on Geothermal Reservoir Engineering, Stanford, California, Janurary 2012.

Irving, D. J., and Knight, J. R., 2006, Numerical simulation of antenna transmission and reception for crosshole ground-penetrating radar: Geophysics, v. 71, p. K37.

Jeannin, M., Garambois, S., Grégoire, C., and Jongmans, D., 2006, Multiconfiguration GPR measurements for geometric fracture characterization in limestone cliffs (Alps): Geophysics, v. 71, p. B85.

Kana, A. A., West, L. J., and Clark, R. A., 2013, Fracture aperture and fill characterization in a limestone quarry using GPR thin-layer AVA analysis: Near Surface Geophysics, v. 11, no. 3, p. 293-305.

Kim, C., Daniels, J. J., Guy, E. D., Radzevicius, S. J., and Holt, J., 2000, Residual Hydrocarbons in a Water-Saturated Medium: A Detection Strategy Using Ground Penetrating Radar: Environmental Geosciences, v. 7, no. 4, p. 169-176.

Kruk, J. v. d., Wapenaar, C. P. A., Fokkema, J. T., and Berg, P. M. v. d., 2003, Three-dimensional imaging of multicomponent ground-penetrating radar data: Geophysics, v. 68, p. 1241.

Lane, J. W., Buursink, M. L., Haeni, F. P., and Versteeg, R. J., 2000, Evaluation of Ground-Penetrating Radar to Detect Free-Phase Hydrocarbons in Fractured Rocks—Results of Numerical Modeling and Physical Experiments: Ground Water, v. 38, no. 6, p. 929-938.

Lehmann, F., Boerner, D. E., Holliger, K., and Green, A. G., 2000, Multicomponent georadar data: Some important implications for data acquisition and processing: Geophysics, v. 65, p. 1542.

Lutz, P., Garambois, S., and Perroud, H., 2003, Influence of antenna configurations for GPR survey: information from polarization and amplitude versus offset measurements: Geological Society, London, Special Publications, v. 211, no. 1, p. 299-313.

Luzitano, R. D., and Ulrych, T. J., 1996, The value of two-component GPR data: Identifying the polarization contribution in amplitude anomalies, *in* Proceedings Proceedings of the Symposium on the Application of Geophysics to Environmental and Engineering Problems1, p. 1179-1187.

Radzevicius, S. J., and Daniels, J. J., 2000, Ground penetrating radar polarization and scattering from cylinders: Journal of Applied Geophysics, v. 45, no. 2, p. 111-125.

Rayburn, J. A., K Knuepfer, P. L., and Franzi, D. A., 2005, A series of large, Late Wisconsinan meltwater floods through the Champlain and Hudson Valleys, New York State, USA: Quaternary Science Reviews, v. 24, no. 22, p. 2410-2419.

Roberts, R. L., and Daniels, J. J., 1996, Analysis of GPR Polarization Phenomena: Journal of Environmental and Engineering Geophysics, v. 1, p. 139.

Sambuelli, L., and Calzoni, C., 2010, Estimation of thin fracture aperture in a marble block by GPR sounding: Issues, v. 52, no. 4, p. 2011.

Sassen, D. S., and Everett, M. E., 2009, 3D polarimetric GPR coherency attributes and full-waveform inversion of transmission data for characterizing fractured rock: Geophysics, v. 74, p. J23.

Sato, M., and Miwa, T., 2000, Polarimetric borehole radar system for fracture measurement: Subsurface Sensing Technologies and Applications, v. 1, no. 1, p. 161-175.

Seol, S. J., Kim, J. h., Song, Y., and Chung, S. h., 2001, Finding the strike direction of fractures using GPR: Geophysical Prospecting, v. 49, no. 3, p. 300-308.

Talley, J., Baker, G. S., Becker, M. W., and Beyrle, N., 2005, Four dimensional mapping of tracer channelization in subhorizontal bedrock fractures using surface ground penetrating radar: Geophys. Res. Lett., v. 32, no. 4.

Taner, M. T., Koehler, F., and Sheriff, R., 1979, Complex seismic trace analysis: Geophysics, v. 44, no. 6, p. 1041-1063.

Teixeira, F., Chew, W. C., Straka, M., Oristaglio, M., and Wang, T., 1998, Finite-difference time-domain simulation of ground penetrating radar on dispersive, inhomogeneous, and conductive soils: Geoscience and Remote Sensing, IEEE Transactions on, v. 36, no. 6, p. 1928-1937.

Theune, U., Rokosh, D., Sacchi, M. D., and Schmitt, D. R., 2006, Mapping fractures with GPR: A case study from Turtle Mountain: Geophysics, v. 71, p. B139.

Tsang, C. F., and Neretnieks, I., 1998, Flow channeling in heterogeneous fractured rocks, Rev. Geophys., Volume 36, p. 275-298.

Tsoflias G. P. (2008), GPR Imaging of Dual-Porosity Rocks: Insights to Fluid Flow, The Leading Edge, November 2008 Special Issue on Near-Surface Geophysics, Vol. 27, No. 11, p. 1436-1445.

Tsoflias G. P., Baker M., and Becker, M.W., 2012, Field GPR Monitoring of Flow Channeling in Fractured Rock, Abstract NS51B-1834, Fall AGU Meeting, San Francisco, Calif., December 3-7, 2012.

Tsoflias G. P., Becker, M.W., Baker, M., and Perll, C., 2012, Advancing Field Methods for GPR Monitoring of Flow Channeling in Fractured Rock, SEG-AGU Hydrogeophysics Joint Workshop, Boise, Idaho, 8-11 July, 2012.

Tsoflias, G. P., and Becker, M. W., 2008, Ground-penetrating-radar response to fracture-fluid salinity: Why lower frequencies are favorable for resolving salinity changes: Geophysics, v. 73, p. J25.

Tsoflias, G. P., Halihan, T., and Sharp, J. M., 2001, Monitoring pumping test response in a fractured aquifer using ground-penetrating radar: Water Resour. Res., v. 37, no. 5, p. 1221-1229.

Tsoflias, G. P., and Hoch, A., 2006, Investigating multi-polarization GPR wave transmission through thin layers: Implications for vertical fracture characterization: Geophys. Res. Lett., v. 33, no. 20.

Tsoflias, G. P., Van Gestel, J. P., Stoffa, P. L., Blankenship, D. D., and Sen, M., 2004, Vertical fracture detection by exploiting the polarization properties of ground-penetrating radar signals: Geophysics, v. 69, no. 3, p. 803-810.

Villela, A., and Romo, J. M., 2013, Invariant properties and rotation transformations of the GPR scattering matrix: Journal of Applied Geophysics, v. 90, p. 71-81.

Yee, K., 1966, Numerical solution of initial boundary value problems involving Maxwell's equations in isotropic media: Antennas and Propagation, IEEE Transactions on, v. 14, no. 3, p. 302-307.